

3-28-2014 12:00 AM

Multiparametric Imaging and MR Image Texture Analysis in Brain Tumors

Harish A. Sharma, *The University of Western Ontario*

Supervisor: Dr. Robert Bartha, *The University of Western Ontario*

A thesis submitted in partial fulfillment of the requirements for the Doctor of Philosophy degree
in Medical Biophysics

© Harish A. Sharma 2014

Follow this and additional works at: <https://ir.lib.uwo.ca/etd>



Part of the [Medical Biophysics Commons](#), and the [Oncology Commons](#)

Recommended Citation

Sharma, Harish A., "Multiparametric Imaging and MR Image Texture Analysis in Brain Tumors" (2014).
Electronic Thesis and Dissertation Repository. 1967.
<https://ir.lib.uwo.ca/etd/1967>

This Dissertation/Thesis is brought to you for free and open access by Scholarship@Western. It has been accepted for inclusion in Electronic Thesis and Dissertation Repository by an authorized administrator of Scholarship@Western. For more information, please contact wlsadmin@uwo.ca.

**MULTIPARAMETRIC IMAGING AND MR IMAGE TEXTURE ANALYSIS IN
BRAIN TUMORS**

(Thesis format: Integrated Article)

by

Harish Sharma

Graduate Program in Medical Biophysics

A thesis submitted in partial fulfillment
of the requirements for the degree of
Doctor of Philosophy

The School of Graduate and Postdoctoral Studies
The University of Western Ontario
London, Ontario, Canada

© Harish Sharma 2014

Abstract

This thesis addresses some of the challenges that clinicians face in the course of treatment of brain tumors. Glioblastoma multiforme (GBM, grade IV) is the most malignant form of primary brain tumor and recurrence following treatment is common. Non-invasive imaging is an important component of brain tumor treatment planning and monitoring. Unfortunately, tumor recurrence and radiation injury (RI) in patients with GBM have similar appearances on follow-up conventional magnetic resonance imaging (MRI), making it difficult to choose the most appropriate treatment plan. Brain metastases which are secondary brain tumors are common in patients with systemic cancer. Differentiating between GBM and metastatic tumor is also difficult with conventional MRI, but is essential for guiding surgical and radiotherapy treatment. Therefore, the overall goal of this thesis is to develop imaging methods that improve brain tumor detection.

The first objective was to develop a method to discriminate between GBM tumor recurrences and RI using a multiparametric characterization of the tissue incorporating conventional MRI signal intensities (T2-weighted (T2w) and fluid attenuated inversion recovery (FLAIR)) and diffusion tensor imaging parameters (fractional anisotropy (FA) and radial diffusivity (RD)). In the RI region there were significant correlations between FA and RD as well as between T2w and FLAIR signal intensities. No such correlations were observed in the tumor region. These correlations may aid in differentiating between tumor recurrence and RI.

The second objective was to differentiate between GBM and metastasis (MET); the two most common types of brain tumors. Both exhibit similar radiologic appearance on

routine MR imaging but require different treatment strategies. The goal of this study was to investigate whether texture based image analysis of routine MR images (contrast-enhanced T1-weighted images) would provide quantitative information that could be used to differentiate between GBM and MET. Our results demonstrate that first-order texture feature of standard deviation and second-order texture features of entropy, inertia, homogeneity, and energy show significant differences between the two groups. Receiver operating characteristic (ROC) curve analysis showed that combining first- and second-order features increased the predictive accuracy in differentiating between GBM and MET.

Finally, helical tomotherapy (HT) is a type of radiation delivery technique that allows for a radiosurgery-type simultaneous infield boost (SIB) of multiple brain metastases, synchronously with whole brain radiation therapy (WBRT). However, some patients' tumors may not respond to HT type WBRT+SIB. The goal of our study was to investigate whether quantitative measurements of tumor size and appearance on magnetic resonance imaging (MRI) scans acquired prior to HT type WBRT+SIB treatment could be used to differentiate responder and non-responder patient groups. Our results demonstrated that smaller size lesions may respond better to this type of radiation therapy. Measures of appearance provided limited added value over measures of size for response prediction. Quantitative measurements of rim enhancement and core necrosis performed separately did not provide additional predictive value.

In summary, our correlation based method for differentiating tumor from RI, differentiating GBM and MET using quantitative texture features, and correctly selecting

patients who will respond to HT type radiation treatment may be used to better plan patient treatment.

Keywords

Glioblastoma, multiparametric imaging, CT perfusion, diffusion tensor imaging, MRI, metastasis, helical tomotherapy, whole brain radiotherapy. Stereotactic radiosurgery, texture analysis, RECIST, entropy, homogeneity, correlation, inertia, energy.

Co-Authorship Statement

The following thesis contains materials presented at conferences as well as material that has been submitted for publications. The contributions of co-authors are summarized below.

Chapter 2 contains material that has been submitted for publication to Journal of Medical Imaging and Radiation Oncology. The co-authors are Harish Sharma, Barbara Fisher, Ting-Yim Lee, Donald Lee, Yves Bureau, and Robert Bartha. H. Sharma optimized the pulse sequences for MRI data acquisition, collected and analyzed the data and prepared the manuscript. B. Fisher helped recruit patients with glioblastoma for MRI scans and provided guidance with data analysis. D. Lee provided guidance with data analysis. T.Y. Lee provided perfusion CT data and software for computing the perfusion parameter maps. Y. Bureau provided guidance with statistical analysis of the data. R. Bartha provided guidance with data analysis and manuscript revisions. All authors were involved in review and editing of the manuscript.

Chapter 3 contains material that has been submitted for publication to American Journal of Neuroradiology. The co-authors are Harish Sharma, Aaron Ward, Yves Bureau, George Rodrigues, Glenn Bauman and Barbara Fisher. H. Sharma and B. Fisher wrote the ethics to obtain MRI data of glioblastoma patients. H. Sharma developed the software for data analysis and prepared the manuscript. MRI data for metastasis patients was provided by A. Ward, G. Rodrigues and G. Bauman. A. Ward provided guidance with development of the software and data analysis. Y. Bureau provided guidance with

statistical analysis of the data. All authors were involved in review and editing of the manuscript.

Chapter 4 contains material that will be submitted to *Acta Oncologica*. The co-authors are Harish Sharma, Glenn Bauman, George Rodrigues, Robert Bartha and Aaron Ward. The MRI data for metastasis patients was provided by A. Ward, G. Rodrigues and G. Bauman. H. Sharma developed the software for data analysis and prepared the manuscript. A. Ward provided guidance with development of the software and data analysis. All authors were involved in review and editing of the manuscript.

Epigraph

“The scientist is not a person who gives the right answers, he's one who asks the right questions.”

— Claude Lévi-Strauss

Acknowledgments

The work within this thesis was accomplished with the assistance of several people.

I would like to express my appreciation to Dr. Robert Bartha for his ongoing support and advice. Special thanks to Dr. Aaron Ward for his supervision and dedication to these projects, and for being an invaluable source of knowledge and support.

Thank you to Drs. George Rodrigues and Glenn Bauman for their guidance with the metastasis project. My sincerest appreciation to Dr. Yves Bureau for the countless hours we spent discussing statistics, and to Dr. Barbara Fisher for her enthusiasm on these projects, glioblastoma patient recruitment, and for always being available to answer my clinical questions.

Special thanks to Timothy Yeung for all our perfusion CT discussions and Kim Krueger for maintaining the MRI scanner and assisting with patient scanning and data transfer.

I would like to thank the Department of Medical Biophysics for providing a WGRS Scholarship for the duration of my PhD program.

And finally, thank you to my wife for her unwavering support and love.

Table of Contents

Abstract.....	ii
Co-Authorship Statement.....	v
Epigraph.....	vii
Acknowledgments.....	viii
Table of Contents	ix
List of Tables	xii
List of Figures	xiii
List of Abbreviations and Symbols.....	xvi
1 Introduction	1
1.1 Brain Tumor.....	1
1.1.1 Primary Brain Tumor: Glioblastoma Multiforme.....	2
1.1.2 Secondary Brain Tumor: Metastasis	5
1.2 Treatment Assessment	10
1.2.1 Response Evaluation Criteria in Solid Tumors.....	11
1.3 Multiparametric Imaging	12
1.3.1 Perfusion CT	13
1.3.2 MRI: T1w, T2w and FLAIR Imaging.....	16
1.3.3 Diffusion Tensor Imaging.....	26
1.4 Texture Analysis	31
1.4.1 First-Order Textures.....	32
1.4.2 Second-Order Textures	34
1.4.3 Texture Analysis of Medical Images	38
1.5 Thesis Objectives	40

1.5.1	Objective 1: Multiparametric imaging in patients with glioblastoma	40
1.5.2	Objective 2: Texture analysis in differentiating between glioblastoma and metastasis	40
1.5.3	Objective 3: Texture analysis in patient selection for radiation therapy ..	41
1.6	References.....	42
2	Analysis of morphological MRI parameters and diffusion tensor parameters for perfusion CT derived high permeability areas in glioblastoma: identifying tumor recurrence from radiation induced necrosis	57
2.1	Introduction.....	57
2.2	Methods.....	59
2.2.1	CT Perfusion Imaging.....	61
2.2.2	Data Analysis	61
2.3	Results.....	63
2.4	Discussion	67
2.5	References.....	70
3	Differentiating between glioblastoma and metastasis using first- and second-order MR image texture.....	75
3.1	Introduction.....	75
3.2	Methods.....	77
3.2.1	Data Analysis	78
3.2.2	Statistical Analysis.....	80
3.3	Results.....	82
3.3.1	ROC curve analysis:	86
3.4	Discussion	91
3.5	Conclusions.....	94
3.6	References.....	95

4	MRI-based prediction of response to whole-brain helical tomotherapy with simultaneous intralesional boost for metastatic brain cancer using quantitative size and appearance features	99
4.1	Introduction.....	99
4.2	Materials and methods	101
4.2.1	Materials	101
4.2.2	Methods.....	105
4.3	Results.....	107
4.4	Discussion	115
4.5	References.....	120
5	Conclusion and Future Work	123
5.1	Multiparametric Imaging in Patients with Glioblastoma.....	123
5.2	Texture Analysis in Differentiating between Glioblastoma and Metastasis.....	124
5.3	Texture Analysis in Patient Selection for Radiation Therapy	126
5.4	References.....	127
	Appendix: Ethics Approval Notices	131
	Curriculum Vitae	135

List of Tables

Table 1.1 Techniques used for differentiating tumor recurrence from radiation injury	4
Table 1.2 Four categories of RECIST.....	12
Table 1.3 Summary of the diffusion tensor parameters.....	30
Table 2.1 Patient demographics and clinical information.	60
Table 2.2 Parameters measured in the high permeability and RI regions.	65
Table 3.1 GLCM-based second-order texture features.....	80
Table 3.2 Mean and SD of each of the first-order texture feature.	82
Table 3.3 Mean and SD of each of the second-order texture feature.	83
Table 3.4 ROC curve analysis for each of the first- and second-order texture features ...	87
Table 4.1 Primary site of metastasis for non-responders and responders.....	103
Table 4.2 Feature values measured for each group in the whole tumor	109
Table 4.3 Feature values measured for each group in the tumor core.	110
Table 4.4 Feature values measured for each group in the tumor rim	111
Table 4.5 Optimal thresholds of features having the four largest AUCs.....	114

List of Figures

Figure 1.1 Post-contrast T1-weighted image of patient with glioblastoma	3
Figure 1.2 Post-contrast T1-weighted image of patient with metastasis	6
Figure 1.3 Radiation dose planning image for WBRT	7
Figure 1.4 Radiation dose planning image for SRS.....	8
Figure 1.5 Radiation dose planning image for HT	10
Figure 1.6 A general arterial time attenuation curve.	15
Figure 1.7 Blood flow scaled IRF according to the Johnson and Wilson model.....	15
Figure 1.8 T1 relaxation curve.....	18
Figure 1.9 T2 decay curve.	19
Figure 1.10 Spin echo sequence.....	21
Figure 1.11 Gradient echo sequence.....	23
Figure 1.12 Inversion recovery sequence.	24
Figure 1.13 Sine waves and protons with same phase and different phase.	27
Figure 1.14 DTI sequence.....	28
Figure 1.15 Diffusion tensor with eigen values λ_1 , λ_2 , λ_3	29

Figure 1.16 Gray-level histogram.	32
Figure 1.17a Sample image.....	35
Figure 2.1a-f FLAIR, T2w images, PS and CBV maps, and the ROIs used for analysis.	64
Figure 2.2a-f Scatterplots summarizing the correlation analysis.	66
Figure 3.1 Post-contrast T1w image of GBM and MET lesion.....	78
Figure 3.2 Plots of the first-order texture features for GBM and MET	84
Figure 3.3 Plots of the second-order texture features for GBM and MET	85
Figure 3.8a,b GBM and MET tumors showing similar appearance on routine MR image but differences in the second-order texture measures.	92
Figure 4.1 Isodose curves for an HT plan, illustrating a whole brain radiation plan with integrated high-dose boost to a metastatic lesion.	102
Figure 4.2 Sample images of brain metastases at the pre-treatment and follow-up imaging time points, with manual contours overlaid in red.....	103
Figure 4.3 Representative axial cross sections from inferior (left) to superior (right) of two tumors, one in each row	104
Figure 4.4 Boxplots for 3D volume and Diameter for the whole tumor, the core, and rim regions, comparing responders (R) and non-responders (NR).	112

Figure 4.5 Boxplots for Homogeneity and Inertia for the whole tumor, the core, and rim regions, comparing responders (R) and non-responders (NR).	112
Figure 4.6 Boxplots for Correlation and energy for the whole tumor, the core, and rim regions, comparing responders (R) and non-responders (NR).	113
Figure 4.7 ROC curves for the four features that had the largest AUCs	114

List of Abbreviations and Symbols

b_{ij}	b matrix elements
d	distance vector
D_{ij}	diffusion tensor elements
e	eigenvectors
f	frequency
k	kurtosis
n	number
s	standard deviation
t	time
x	gray level
α	flip angle
γ	gyromagnetic ratio
λ	eigenvalues
θ	angle
3D	three-dimensional
4D	four-dimensional
AUC	area under the curve
AxD	axial diffusivity
B_0	static magnetic field strength
CBF	cerebral blood flow
CBV	cerebral blood volume
CI	confidence interval
CL	linear tensor
CP	planar tensor
CR	complete response
CS	spherical tensor
CSF	cerebrospinal fluid
CT	computed tomography
DT	diffusion tensor
DTI	diffusion tensor imaging
FA	fractional anisotropy
FID	free induction decay
FLAIR	fluid attenuated inversion recovery
G	probability
GBM	glioblastoma multiforme
GE	General Electric
GLCM	gray level co-occurrence matrix
GRE	gradient echo
Gy	Gray
HT	helical tomotherapy
HU	hounsfield units
IQR	interquartile range

IRF	impulse residue function
LRM	logistic regression model
Lt	left
M	magnetization
M_0	net magnetization
MD	mean diffusivity
M_{xy}	transverse component of magnetization
M_z	longitudinal component of magnetization
MET	metastasis
MR	magnetic resonance
MRI	magnetic resonance imaging
MRS	magnetic resonance spectroscopy
MTT	mean transit time
NR	non-responders
PCT	perfusion CT
PD	progressive disease
PET	positron emission tomography
PR	partial response
PS	permeability
R	responders
RD	radial diffusivity
RECIST	response evaluation criteria in solid tumors
RF	radio frequency
RI	radiation injury
ROC	receiver operating characteristic
ROI	region of interest
Rt	right
STD	stable disease
SD	standard deviation
SE	standard error
SI	signal intensity
SIB	simultaneous in-field boost
SK	skewness
SPECT	single-photon emission computed tomography
SRS	stereotactic radiosurgery
T	Tesla
T1	longitudinal relaxation time
T1w	T1-weighted
T2	transverse relaxation time
T2w	T2-weighted
TAC	time–attenuation curve
TE	echo time
TI	inversion time
TR	repetition time
VMAT	volumetric modulated arc therapy

WBRT
WHO

whole brain radiotherapy
World Health Organization

1 Introduction

Accurate discrimination of tumor from radiation injured tissues and differentiation of tumor types and grades using noninvasive imaging is essential for guiding surgical and radiotherapy treatments. This thesis describes the use of multiparametric imaging and image processing techniques to characterize brain tumors. The long-term goal of these methods is to help select appropriate treatment and assess treatment response in patients with brain tumor.

This chapter introduces the imaging and image processing techniques upon which the following chapters are based. Chapter 2 describes the application of multiparametric imaging in an attempt to improve the detection of brain tumor recurrence following treatment. Chapter 3 describes the use of texture based analysis in differentiating enhancing lesions as primary or secondary tumor types. Chapter 4 outlines the use of texture based image analysis for patient selection in radiation therapy.

1.1 Brain Tumor

A tumor is any uncontrolled growth of abnormal cells. Tumors that are located within the brain are called brain tumors and can be classified into two categories: primary and secondary brain tumors.

Primary brain tumors can arise from the cells, the meninges (membranes around the brain), or neurons in the brain. Gliomas and meningiomas are the most common primary

brain tumors. Gliomas are thought to be derived from glial cells such as astrocytes, oligodendrocytes, and ependymal cells. Gliomas are classified into four grades by the World Health Organization (WHO) on the basis of their histologic features and malignancies¹. Glioblastomas are considered grade IV; the most aggressive and malignant type of brain tumor.

Secondary brain tumors are referred to as metastases. They do not initiate in the brain, but rather metastases occurs when cancer cells break away from a primary tumor site elsewhere in the body and travel to the brain through the blood system.

1.1.1 Primary Brain Tumor: Glioblastoma Multiforme

Glioblastoma multiforme (GBM) is the most lethal and aggressive form of primary brain tumor. It is a grade IV type of brain tumor. Median survival for patients with glioblastoma is 12-15 months². GBM is derived from the malignant transformation of glial cells³. Despite recent advances in radiation, chemotherapy, surgical techniques, and newer investigational drugs, GBM has a poor prognosis. Medical imaging plays an important role in the diagnosis of GBM. Typically post-contrast magnetic resonance (MR) imaging is used for diagnosis followed by biopsy for pathological validation. GBM often appear as ring-enhancing lesions on post-contrast MR images (Figure 1.1)^{3, 4}. Treatment options for patients with GBM are determined by tumor size, location, and the associated symptoms. The current standard of care for patients with GBM is surgical resection of the tumor followed by radiation therapy and concomitant and adjuvant temozolomide chemotherapy. This approach has been shown to standardize treatment and prolong survival for patients⁵. Radiation therapy damages the genetic material (DNA)

within tumor cells and limits their ability to successfully reproduce^{6, 7}. Tumor cells are less able to repair DNA than healthy cells. With each subsequent radiation dose, the cumulative effect of unrepaired DNA strand breaks initiates apoptosis (cell death) in these tumor cells^{6, 7}.

Radiation injury (RI) is an undesirable but unavoidable side effect of radiation treatment. Radiation injury is characterized by extensive necrosis due to small artery injury and direct damage to oligodendroglia⁸. The incidence of radiation injury depends on the total radiation dose and the rate of delivery⁹. Concomitant chemotherapy enhances radiation injury. RI appears as enhancing lesions on MR imaging. Since GBM is a high grade tumor, recurrences are common even after treatment, and these recurrences appear as hyperintense regions on post-contrast MR images.

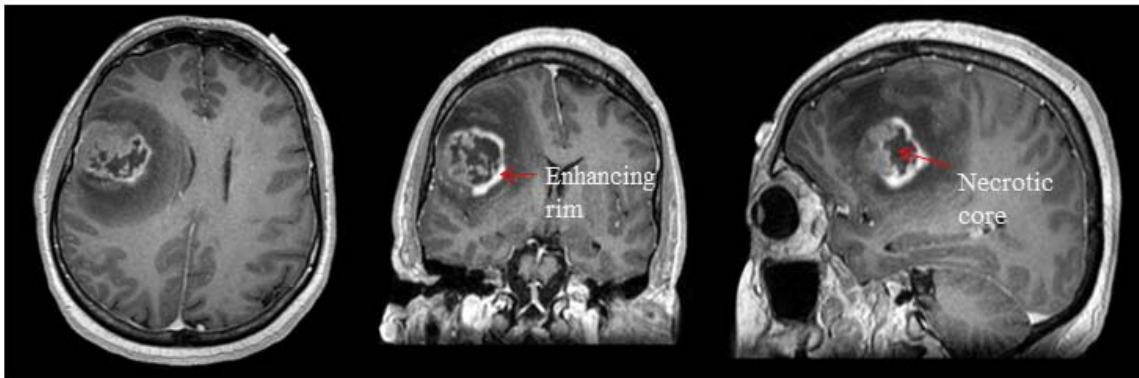


Figure 1.1 Post-contrast T1-weighted image of patient with glioblastoma. The tumor appears to have a necrotic core and enhancing rim.

The presence of enhancing lesions after chemo-radiation therapy may represent either tumor recurrence or radiation induced injury or both^{10, 11}. Differentiating between tumor recurrence and RI regions can be difficult with conventional MR imaging¹², however it

is very important to differentiate these two entities since the treatment options and prognoses for each are considerably different.

There have been numerous attempts to differentiate tumor recurrences from RI using conventional morphologic imaging as well as various functional imaging techniques such as CT perfusion, MR perfusion, diffusion weighted imaging, MR spectroscopy, single-photon emission computed tomography and positron emission tomography¹²⁻²⁹. Table 1.1 provides a partial list of studies that have used various techniques to differentiate tumor recurrence from RI.

Table 1.1 Techniques used for differentiating tumor recurrence from radiation injury¹²⁻²⁹

Technique	Reference	Parameter
Diffusion	Hein et al.	Apparent diffusion coefficient ratios
	Kashirmura et al.	Fractional anisotropy
	Asai et al.	Apparent diffusion coefficient
	Sundgren et al.	Fractional anisotropy
	Xu et al.	Fractional anisotropy
	Zeng et al.	Apparent diffusion coefficient
Perfusion	Barajas et al.	Cerebral blood volume
	Jain et al.	Cerebral blood flow
	Jain et al.	Cerebral blood volume
	Bobek-Billewicz	Cerebral blood volume
	Fisher-stevens et al.	Permeability
MRS	Rabinov et al.	Choline / Creatine
	Zeng et al.	Choline / Creatine
	Zeng et al.	Choline / N-Acetyl aspartate
	Rock et al.	Choline / Creatine
	Rock et al.	Choline / N-Acetyl aspartate
PET	Langleben et al.	Fluorodeoxy glucose uptake
	Tsuyuguchi et al.	¹¹ C-Methionine uptake
SPECT	Schwartz et al.	201Thallium uptake
	Samnick et al.	123 Iodine uptake

All of the above techniques have shown some promise but none of them have been able to convincingly differentiate radiation injury from tumor recurrence. FDG-PET and dynamic contrast enhanced CT have shown better sensitivity and accuracy compared to other techniques. However, with the limited availability of PET scanners and the risks associated with radiation exposure from CT, the search for an accessible and reliable technique continues with biopsy of the affected tissue still considered the gold standard.

1.1.2 Secondary Brain Tumor: Metastasis

Brain metastasis is common among patients with systemic cancer. They are a significant public health issue, with 20–40% of patients with solid tumors subsequently developing symptomatic brain metastases³⁰. Approximately 150,000 brain metastases are diagnosed annually in the United States. Brain metastasis (MET) is thought to occur when the primary tumor acquires the ability to migrate away from the primary site and travels to the brain. The most common origins of brain metastasis are from breast cancer, melanoma and lung cancer. Metastasis often causes severe neurological symptoms that significantly impair quality of life. With recent improvements in diagnostic imaging and increasing patient survival due to improved systemic cancer control, the incidence of intracranial metastatic disease is projected to rise³¹. Imaging is the most important diagnostic modality for brain metastasis. Metastasis appears as an enhancing rim with necrotic core on a post-contrast MRI (Figure 1.2). The management of brain metastasis initially involves treating the symptoms using corticosteroids, anticonvulsants to reduce peritumoral edema and prevent recurrent seizures and surgical resection for debulking

followed by therapeutic approaches of whole brain radiotherapy (WBRT), stereotactic radiosurgery (SRS), and/or chemotherapy.

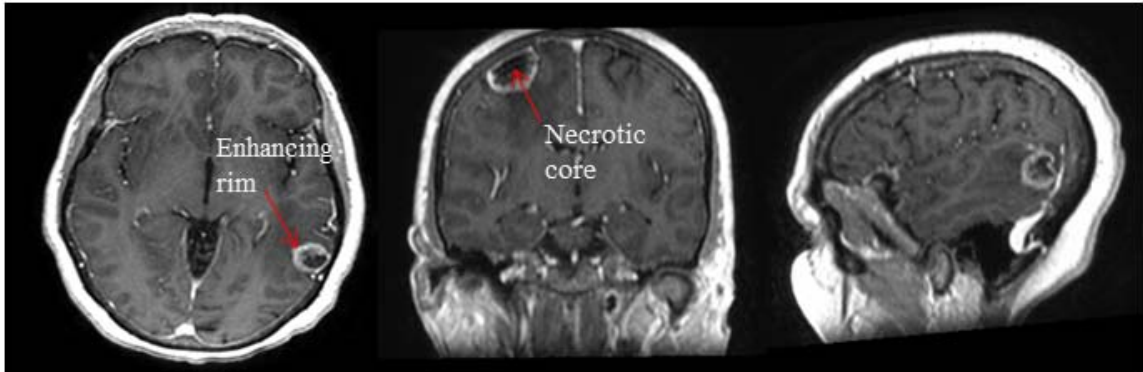


Figure 1.2 Post-contrast T1-weighted image of patient with metastasis. The tumor has a necrotic core and enhancing rim.

Whole brain radiotherapy (WBRT) is the most commonly used treatment for patients with brain metastasis. It involves delivering a uniform dose of radiation from a linear accelerator to the entire brain while the patient head is immobilized to minimize movement during treatment³². A perforated thermoplastic mask that is shaped to conform to the individual patient's facial features is used to immobilize the patient's head during treatment. Whole brain radiation therapy (WBRT) delivers an even dose of radiation to the entire brain. Figure 1.3 shows WBRT radiation dose planning image. It can be used to treat small undetectable tumors, large tumors that may be developing in different areas of the brain and tumors that are deep in the brain which are inaccessible to surgery. Since radiation is delivered to the entire brain WBRT has side effects that include nausea, vomiting, headache, fever, fatigue and possible worsening of neurologic symptoms.

There is also a risk of memory loss or dementia. WBRT typically improves symptoms, but longer-term survivors may develop neurocognitive deficits^{33, 34}.

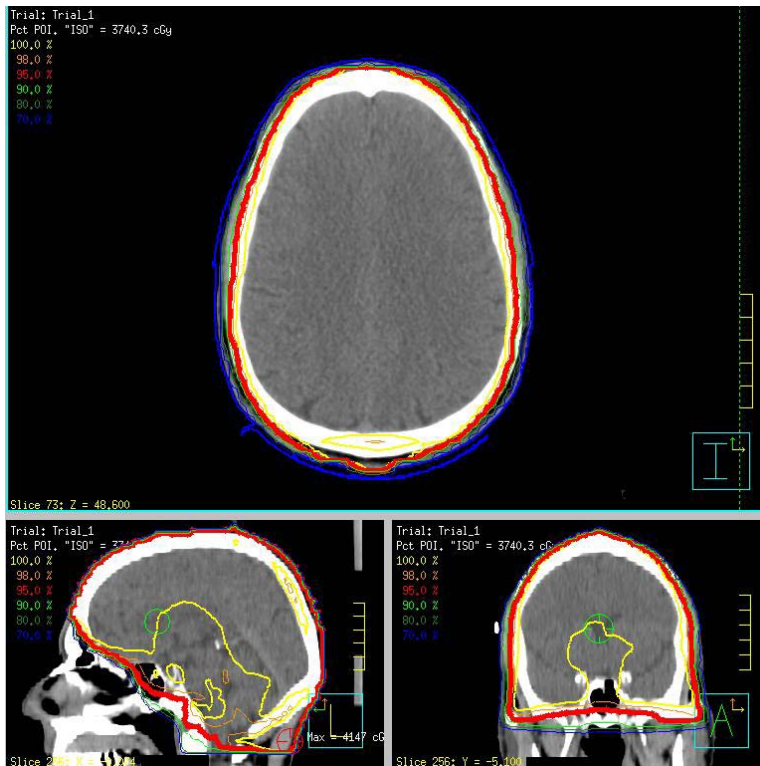


Figure 1.3 Radiation dose planning image for WBRT (yellow=100% of the dose, orange =98%, red=95%, green = 80%, blue =70%). A traditional WBRT delivers 30-60 Gy in 10-15 fractions.

Stereotactic radiosurgery (SRS) is a more targeted form of radiation therapy in which a higher dose of radiation is delivered to the tumor in a single treatment session. Figure 1.4 shows a typical SRS radiation dose planning image. The radiation beam is concentrated on a small region of the parietal lobe. Typically multiple radiation beams are delivered to

the tumor from many different angles using special computer planning. A stereotactic head frame is used to keep the patient's head completely still during the procedure. Because this form of radiation targets the tumor more precisely, it is less likely to hurt healthy tissue. Generally, SRS may be used to treat patients with up to three lesions, although this may vary depending on the size and location of the tumors. For multiple lesions (>3), WBRT is usually the best option. WBRT or SRS is also an option for people who are not candidates for surgery.

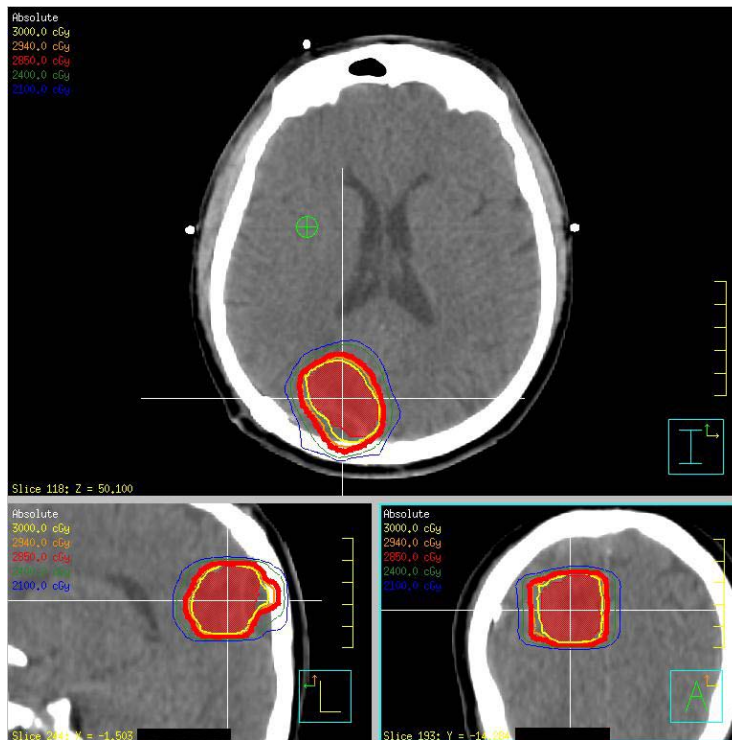


Figure 1.4 Radiation dose planning image for SRS (yellow=100% of the dose, orange =98%, red=95%, green = 80%, blue =70%). A traditional SRS would deliver 15-20 Gy in a single fraction.

SRS combined with WBRT has been shown to yield superior local control, as compared with WBRT alone³⁵. Since SRS involves high dose of radiation to a small region, it has a higher frequency of side effects related to brain tissue necrosis and edema, which can put pressure on surrounding healthy brain tissue. SRS also requires separate stereotactic localization and treatment procedures that add to the cost and patient inconvenience. In addition, the sequential delivery of WBRT and SRS does not allow for the integration of radiation delivery across both components, limiting the ability to fully optimize the radiation dose.

Helical tomotherapy (HT) is a radiotherapy delivery technique that allow for radiosurgery-type simultaneous infield boost (SIB) treatments to be given synchronously with the standard WBRT dose. In HT, the treatment beam rotates about the gantry while the patient table is moved through the gantry, thereby creating a helical or spiral type of beam, hence the name helical tomotherapy. This form of delivery technique can be used to efficiently boost multiple brain metastases without the need for separate stereotactic procedures^{36, 37}. The ability to incorporate this boost contribution with larger field volumes as part of the treatment planning optimization process is advantageous over sequential WBRT and SRS. It has also been shown that HT type WBRT+SIB dose distribution and lesion conformity is comparable to SRS alone³⁸. This type of radiation delivery is beneficial for patients with multiple lesions and lesions that are in close proximity to sensitive organs. It is also useful for patients who cannot be immobilized due to claustrophobia, obesity or physical impairment³⁹.

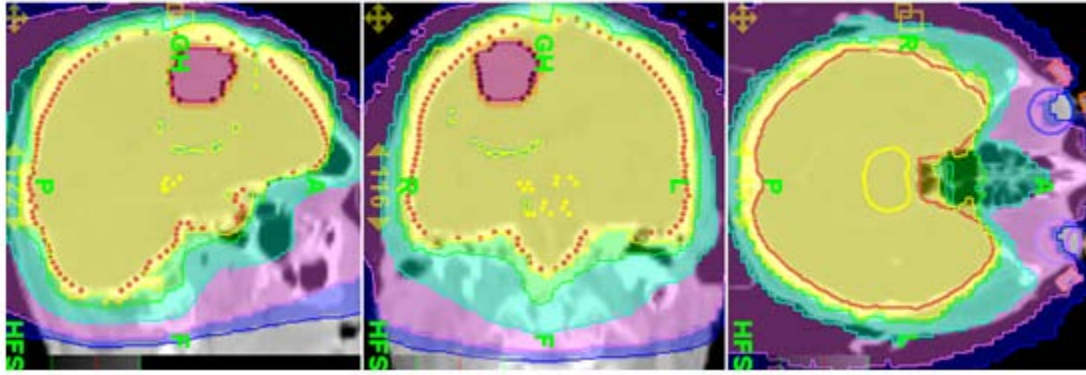


Figure 1.5 Radiation dose planning image for HT, illustrating a whole brain radiation plan with integrated high-dose boost (purple) to a metastatic lesion. The patient underwent HT with 30 Gy WBRT and 60 Gy SIB in 10 fractions.

HT type WBRT+SIB has potential advantages compared to surgery and SRS but it is not appropriate for every patient. Some patients' tumors may not respond to simultaneous WBRT+SIB, and are more appropriately treated with radiosurgery or conventional surgery.

1.2 Treatment Assessment

Treatment assessment is critical for measuring tumor response to therapy. The development of contrast-enhanced CT and MR imaging has allowed radiologists to assess therapeutic response more accurately and reproducibly in patients with brain tumors. Imaging for treatment assessment is routinely performed at three months interval post chemo-radiation therapy. Advanced CT and MRI techniques are currently being used in research settings as response assessment tools for brain tumor patients and are based on detecting cellular changes, and detecting changes in metabolic and hemodynamic

activity⁴⁰. In clinical settings, changes in lesion size are widely used to assess tumor response to therapy.

1.2.1 Response Evaluation Criteria in Solid Tumors

The assessment of treatment response in brain tumors is based on clinical and imaging parameters. A number of techniques have been proposed to assess treatment response. The Macdonald criteria are widely used in assessing treatment response⁴¹ of glial tumors. These criteria involve computing the cross-sectional area of the tumor by measuring the longest single diameter and the longest perpendicular diameter. A 50% decrease in the area is considered a partial response while an 25% increase in the area is considered progression. As an update to the Macdonald criteria, the revised assessment in neuro-oncology criteria⁴² is used for assessing disease progression and treatment response in GBM.

The most common way to assess treatment response in metastasis is the anatomical based method known as response evaluation criteria in solid tumors (RECIST). RECIST were originally published in 2000 and then updated in 2009 for use as a treatment assessment tool in clinical oncology^{43, 44}. RECIST are a set of guidelines that were developed to allow for a simplified and standardized assessment of solid tumors. They classify therapeutic responses in brain tumors based on a one-dimensional tumor measurement: the longest diameter across a contrast-enhancing lesion in the axial plane. In cases where multiple lesions are present, the sum of the longest diameters of up to two measurable lesions is obtained.

Table 1.2 Four categories of RECIST.

Response	Criteria:	Description
RECIST 1.1		
Complete (CR)	Response	Disappearance of all target lesions.
Partial Response (PR)		At least a 30% decrease in the sum of diameters of the target lesions, taking as reference the baseline sum diameters.
Progressive (PD)	Disease	At least a 20% increase in the sum of diameters of target lesions, taking as reference the baseline sum diameters. The appearance of one or more new lesions is also considered progression.
Stable Disease (STD)		Neither sufficient shrinkage to qualify as PR nor sufficient progression to qualify as PD.

The major advantage of the RECIST system is its simplicity. A single diameter measurement is done in the axial plane on the post-contrast images, which can be performed easily and rapidly. The technique performs comparably to more complex two-dimensional and volumetric methods of treatment assessment in brain tumor studies^{45, 46}.

1.3 Multiparametric Imaging

Imaging modalities such as computed tomography (CT) and magnetic resonance imaging (MRI) are commonly used for diagnosis and treatment assessment. CT is often the first line imaging modality performed in patients with brain tumors because it is relatively inexpensive, minimally invasive, and widely available in clinical settings. CT is also used

for surgical planning and radiation treatment planning but MRI is preferred due to its superior soft tissue contrast. For brain tumors, imaging is routinely performed before the initial treatment, immediately after the treatment and at 3-6 month interval thereafter (for high grade brain tumor patients imaging is performed at 2-3 months intervals).

RECIST measures tumor response to treatment based on assessment of anatomical MR images. RECIST requires a well-defined anatomical lesion and relies on the serial measurements of reduction in tumor size during treatment as the basis for response assessment. Treatment selection and response assessment can also be based on functional evaluation of CT and MR images.

1.3.1 Perfusion CT

Brain tumors are associated with angiogenesis and neovascularization (forming new blood vessels) that results in increased blood volume and permeability related to the immature vessels⁴⁷⁻⁵¹. Previous studies have indicated increased microvascular permeability with the increase in biologic aggressiveness of tumors, while a reduction in permeability in response to therapy correlates with decreased tumor growth^{49, 50}. Since perfusion CT (PCT) provides an in vivo marker of angiogenesis, it is widely used as both a diagnostic tool and as a treatment assessment tool in brain tumor imaging^{52, 53}.

Perfusion CT typically requires the acquisition of a baseline image without contrast enhancement followed by a series of images acquired as a function of time following an intravenous bolus injection of a conventional iodinated CT contrast material. The resulting temporal changes in contrast enhancement of the tissue are displayed as time–

attenuation curves (TAC). These TACs are used to quantify a range of parameters that reflect the functional status of the vascular system. This approach is used to produce parametric maps that represent cerebral blood volume (CBV), blood flow (CBF), permeability (PS), mean transit time (MTT), and the size of extravascular space. Many of these parameters have been correlated with tumor grade, aggressiveness, and prognosis^{54, 55}.

Tissue perfusion, blood volume, mean transit time, and other vascular physiological parameters can be derived from dynamic CT data^{53, 56}. The first phase of enhancement (Figure 1.6) can be used to evaluate blood flow, and blood volume which are generally increased in malignant tissues. The second phase is used to evaluate vascular permeability (since tumor blood vessels are abnormally permeable to the contrast agent used)^{56, 57}. Deconvolution method is the most widely used analysis method for determination of perfusion parameters. The deconvolution operation uses a reference “arterial” input function that is selected most often within the anterior cerebral artery. The impulse residue function (IRF) is then calculated by deconvolution of the arterial and tissue time–attenuation curves for the tissue of interest. The IRF (Figure 1.7) is usually constrained in its shape to comprise a plateau followed by a single exponential decay⁵³. The height of the flow scaled IRF will provide the cerebral blood flow and the area under the curve will determine the cerebral blood volume. Width of the IRF equals the mean transit time (MTT). This approach can also be used to include a measurement of capillary permeability by use of a distributed parameter model⁵³.

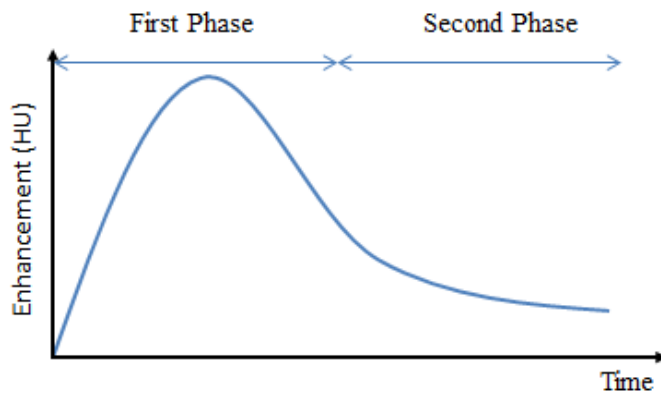


Figure 1.6 A general arterial time attenuation curve showing the first and second phase enhancement. (HU = hounsfield units).

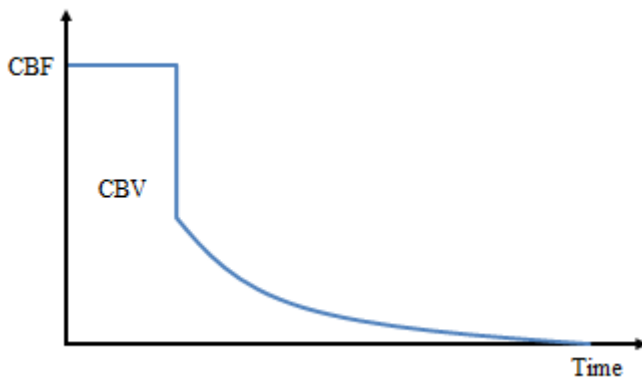


Figure 1.7 Blood flow scaled IRF according to the Johnson and Wilson model. The height of the IRF is the cerebral blood flow and the area under the curve will determine the cerebral blood volume. Width of the IRF equals the mean transit time.

PCT provides quantitatively accurate assessment of brain perfusion. PCT measurements have been shown to be reproducible and have been validated against a range of reference methods including xenon CT and positron emission tomography (PET)⁵⁸⁻⁶⁴. PCT has been used to estimate tumor grade and predict response to radiation therapy in cerebral tumors⁶⁵⁻⁶⁷. The results of perfusion studies^{49, 50} have shown that CBV and PS, a measure of microvascular permeability, are predictive of pathologic grade and correlates with tumor activity. Studies utilizing perfusion techniques have used cerebral blood volume (CBV) values⁶⁸⁻⁷⁰ and recovered percentage of signal intensity and peak height⁷¹ (i.e. shape of dynamic perfusion data) to differentiate between metastasis and GBM.

1.3.2 MRI: T1w, T2w and FLAIR Imaging^{72, 73, 74}

MR imaging is an important diagnostic and treatment assessment imaging modality that has become essential to routine clinical brain tumor imaging due to its superior soft tissue contrast. In clinical MR imaging, the hydrogen nucleus (proton) is primarily used because it is abundantly present in the human body (70-90%) and has high detection sensitivity due to its high gyromagnetic ratio. Since hydrogen atoms have an odd number of protons, this nucleus possesses a property known as spin angular momentum. The phenomenon of magnetic resonance arises in atoms with odd numbers of protons. In absence of a static magnetic field, the protons are oriented randomly and the net macroscopic magnetic moment is zero. When these protons are subjected to a static magnetic field (B_0), the magnetic moment vectors have a tendency to align in the direction of the static field producing a net magnetization (M_0). They also exhibit precessional behavior at a well-defined frequency due to the interaction between the static magnetic field and the

magnetic moment of the nucleus. The frequency of precession is proportional to the strength of the static magnetic field and is expressed by the Larmor Equation (equation 1.1).

$$f = \frac{\gamma}{2\pi} B_0 \quad [1.1]$$

f = Larmor frequency in Hertz

B_0 = static magnetic field strength in Tesla (T)

γ = gyromagnetic ratio (for protons, $\gamma = 42.57$ MHz/T)

In order to induce signal in the tissue of interest, a component of the net magnetization must be tilted away from its equilibrium axis (z-axis) into the transverse (x-y) plane, which is achieved by applying a rotating magnetic field in the transverse plane at the Larmor frequency using a radio frequency (RF) coil. This process is called excitation, and the applied magnetic field is called an RF pulse. The amplitude and duration of this RF pulse produces a predictable torque on the magnetization vector causing it to rotate away from its equilibrium position by precessing about the axis defined by the RF pulse. This angle of rotation away from the z-axis is also known as flip angle. The transverse component of the magnetization is then detected by the same RF coil. The resulting time-varying signal is called the free induction decay (FID) and represents the basic MR signal. The most common excitation RF pulse is a 90° pulse that rotates the magnetization by 90° into the x-y plane resulting in no z-component. Eventually the net magnetization vector will return to its equilibrium state along the z-axis: this process is called relaxation. Relaxation has both longitudinal and transverse components that occur simultaneously but independent of each other. Longitudinal relaxation refers to recovery

of the longitudinal magnetization along the z-axis, and is characterized by the T1 time constant (Figure 1.8). This is the mechanism by which protons give up their energy to the surrounding lattice in order to return to their equilibrium energy distribution. This process of relaxation is also known as spin-lattice relaxation.

The longitudinal component of magnetization can be written as:

$$M_z(t) = M_0 (1 - e^{-\frac{t}{T_1}}) \quad [1.2]$$

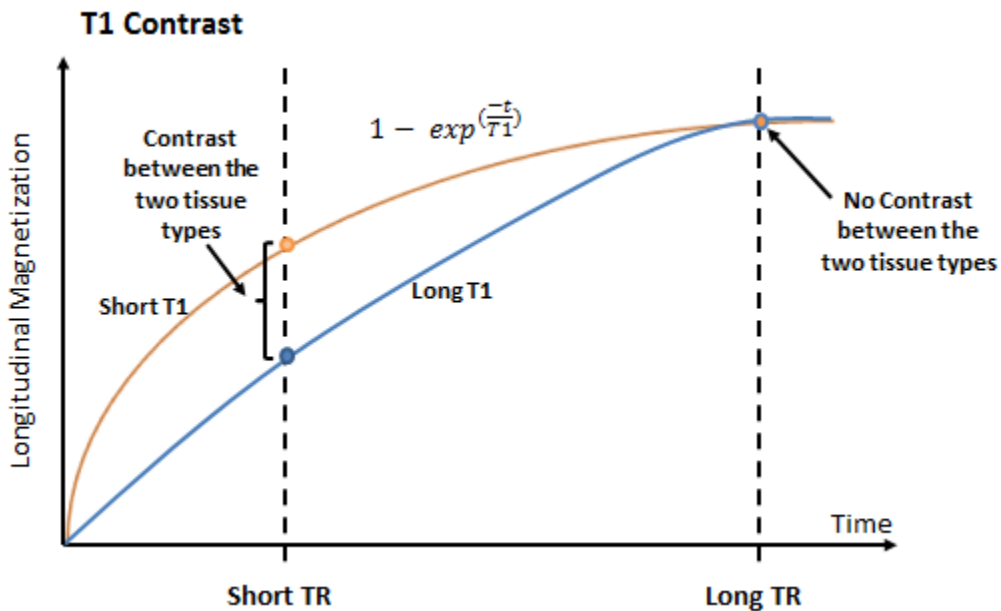


Figure 1.8 T1 relaxation curve showing recovery from $M_z = 0$ following a 90° pulse.

Figure 1.8 shows the T1 relaxation curve. There is no longitudinal magnetization following the 90° RF pulse. Longitudinal magnetization is generated as protons release

their energy to the lattice. This regeneration of the longitudinal magnetization follows an exponential growth process characterized by the T1 time constant.

Transverse relaxation describes the loss of phase coherence of the magnetization in the transverse plane and is characterized by the T2 time constant (Figure 1.9). One mechanism that leads to the decay of transverse magnetization is when protons exchange energy amongst themselves (spin-spin interactions) resulting random phase following energy transfer. This process is also known as spin-spin relaxation.

The transverse component of magnetization can be written as:

$$M_{xy}(t) = M_0 (e^{\frac{-t}{T_2}}) \quad [1.3]$$

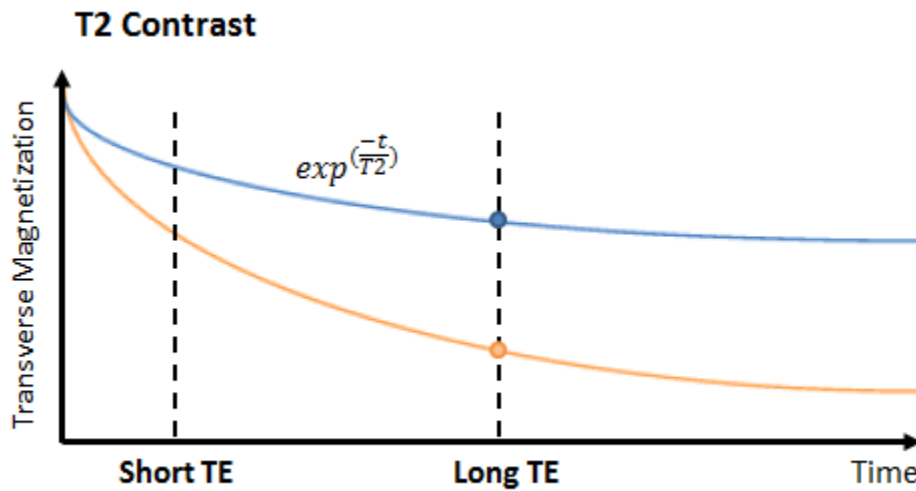


Figure 1.9 T2 signal decay in the transverse plane following excitation. The Blue line represents a long T2 decay while the orange line represents a short T2 decay.

Figure 1.9 shows the T2 decay curve. Following a 90° RF pulse, the magnetic moments of protons have a transverse orientation and rotate together (in-phase) around the magnetic field axis. After a short period of time due to spin-spin interactions, the directions of the protons begin to spread (dephase) causing the transverse magnetization to decay.

During relaxation of the longitudinal magnetization, individual tissues have different levels of magnetization due to their inherently unique T1 values. Similarly, during decay of the transverse magnetization, individual tissues have different levels of magnetization due to their unique T2 values. These T1 and T2 relaxation time constants are intrinsic features of the underlying tissue and vary according to tissue type.

MR images are made up of thousands of tiny squares known as pixels (picture element) or voxels (volume elements). The signal intensity in the pixel or voxel represents the MR signal arising from a volume of tissue that is excited. The greater the MR signal from that tissue, the higher will be the signal intensity of that voxel. Various tissues have different signal intensities on MR image. The differences of the signal intensity are described as image contrast and it allows us to see the boundaries between the tissues. T1 and T2 values of the tissue are important factors that determine the image contrast. MR imaging allows us to produce a wide range of contrasts by changing the acquisition parameters of the MRI pulse sequence.

The MRI pulse sequence represents a precisely timed series of RF and gradient pulses. Gradient pulses create linear variations in the static magnetic field strength and are used to produce a spatially localized signal. Figure 1.10 shows one cycle of a hypothetical MRI pulse sequence. The repetition time (TR) is defined as the time from the center of the first RF pulse to the center of the first RF pulse in the next repetition of the sequence. The time at which the signal is measured is the echo time (TE). TE is defined as the time between the center of the first RF pulse and the center of the echo.

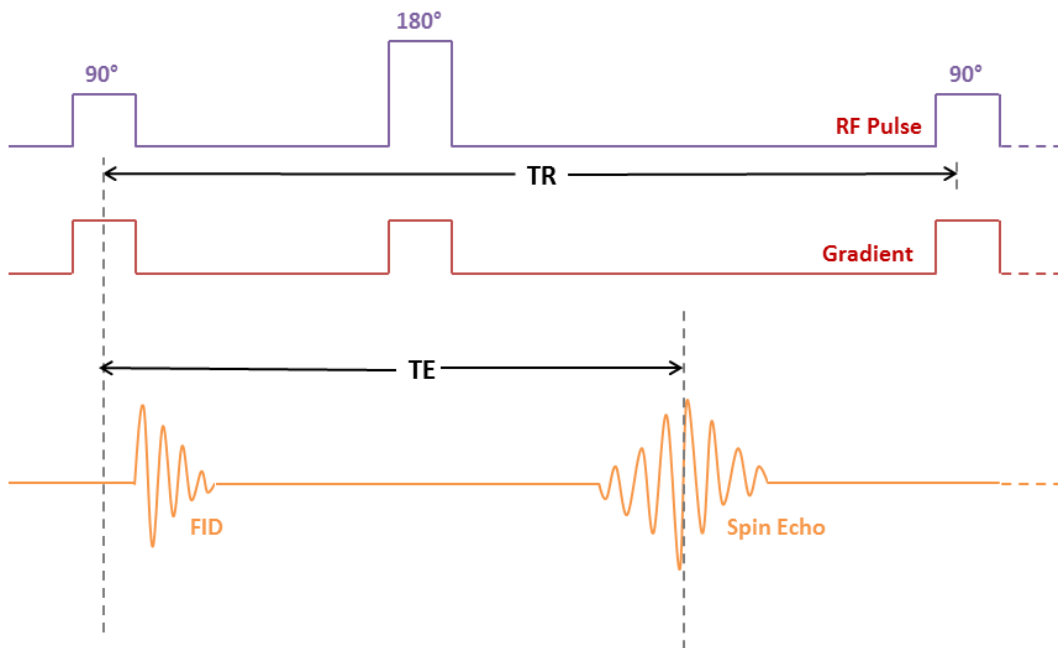


Figure 1.10 A simplified spin echo sequence (phase and frequency encoding gradients not shown here).

By varying the TR and TE, image contrast can be manipulated. Varying the TR modifies the amount of T1 weighting while varying the TE modifies the amount of T2 weighting

in an image. The ability to modify image contrast gives MRI tremendous flexibility. The most common pulse sequences used to create contrast in MR imaging are “spin echo”, “gradient echo”, and “inversion recovery” sequences.

Spin echo: A basic spin echo pulse sequence consists of two RF pulses (Figure 1.10). The first RF pulse is a 90° pulse that excites the protons and produces a FID, and the second RF pulse is an 180° pulse that refocuses the transverse magnetization so that the dephasing effects resulting from B_0 inhomogeneities can be removed. This 180° pulse is exactly halfway between the excitation pulse and the echo. It is also known as a refocusing pulse since it flips the protons around an axis in the transverse plane. The phase that the spins accumulated during the first half of the TE interval is then reversed during the second half of the TE interval and the spin echo is formed.

Gradient echo: A basic gradient echo sequence (GRE) uses a single RF pulse with a flip angle (α) of less than 90° . The echo is generated by gradient reversal (Figure 1.11). GRE are a class of imaging sequences that do not use an 180° RF pulse to refocus the transverse magnetization. The absence of the 180° refocusing pulse allows for faster imaging, but makes it sensitive to the effects of B_0 inhomogeneities.

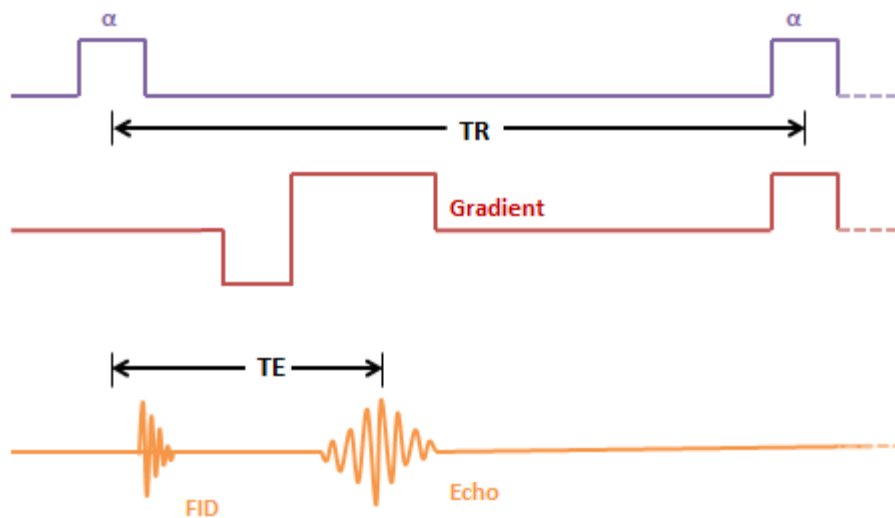


Figure 1.11 Gradient echo sequence.

T1-weighted and T2-weighted images can be produced with either spin echo or gradient echo sequences. T1w images rely on relatively short values of TR to produce T1-weighting and very short TE values to eliminate T2-weighting. T2w images rely on very long values of TR to eliminate T1-weighting and long TE values to produce T2-weighting by creating differences in transverse magnetization between tissue types.

Inversion recovery: Inversion recovery is a variant of a spin echo or gradient echo sequence. The only difference is an additional 180° inversion pulse that is applied before the excitation pulse. Following the inversion pulse and before the excitation pulse there is a delay (known as the inversion time). This inversion time provides a mechanism to use differences in T1 relaxation to generate contrast between tissues of interest. One of the most common variants of the inversion recovery sequence is the fluid attenuated inversion recovery (FLAIR). In a FLAIR sequence, the inversion time is chosen to correspond to the zero-crossing point (Figure 1.12) in the T1 relaxation curve of fluid,

specifically cerebrospinal fluid (CSF). With signal from CSF nulled, lesions in the brain parenchyma appear brighter.

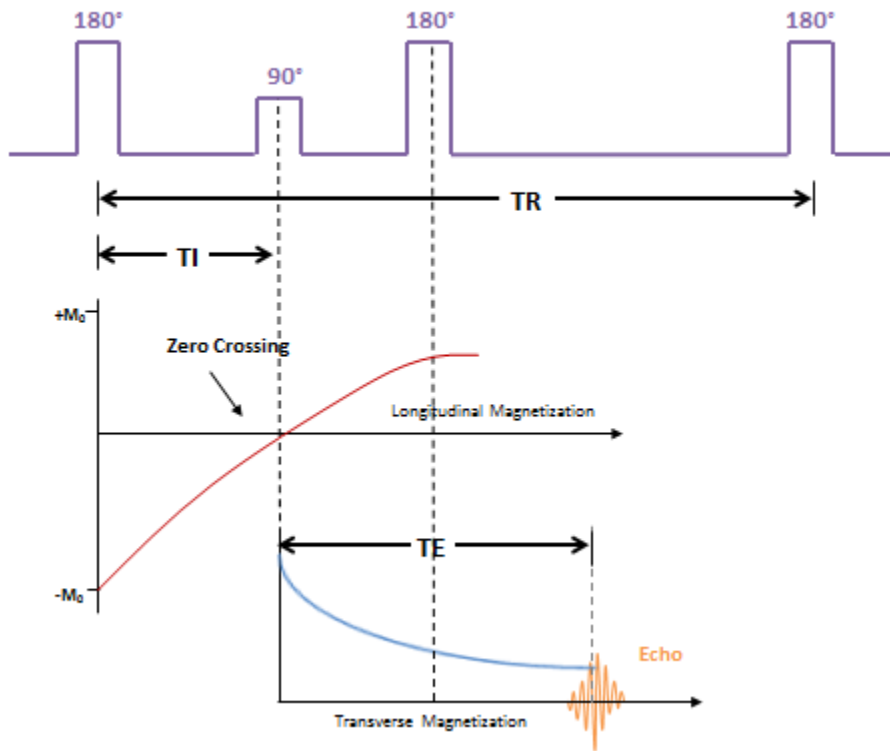


Figure 1.12 Inversion recovery sequence.

In routine brain tumor imaging, morphological MR images are usually acquired as pre- and post-contrast T1w images, T2w images, and FLAIR images. Contrast agents are pharmaceuticals which are used to improve diagnostic information by changing the signal intensity differences. They change the intrinsic tissue properties by changing the local magnetic field and consequently the T1 and T2 relaxation times. Along with CT, MRI is

the first line of diagnostic imaging performed for patients with symptoms suggesting brain tumor. T1w images best depict the anatomy of the brain, and, when used with a contrast agent they also may show brain pathology. However, T2-weighted images provide the best depiction of the tumor, because most tissues that are involved in a pathologic process have higher water content than the normal brain matter, and the fluid causes the affected areas to appear bright on T2w images.

Most brain tumors have prolonged T1 and T2 relaxation times and will appear hypointense relative to normal brain tissue on a T1w image and hyperintense on a T2w image. However, the presence of hemorrhage, necrosis, or calcification can cause a heterogeneous appearance of the tumor. On a post-contrast T1-weighted image, the contrast (gadolinium) accumulates in the extracellular space of the tumor due to local disruption of the blood-brain barrier. As a result, the tumor appears brighter than the normal brain tissue on a post-contrast T1-weighted image due to shortening of the T1 relaxation time constant.

Morphological MRI is helpful in diagnosis of brain tumors, however morphologic MRI alone is insufficient for grading malignant brain tumors, differentiating between tumor types, or differentiating between tumor recurrence and radiation necrosis⁷⁵. Additional imaging techniques have been developed to overcome this problem. Tumors can be further characterized by using advanced MRI techniques such as diffusion tensor imaging, dynamic contrast-enhanced MRI, perfusion MRI and MR spectroscopy⁷⁶⁻⁷⁹.

1.3.3 Diffusion Tensor Imaging

Diffusion Tensor Imaging (DTI) is an advanced MRI technique that provides information about the diffusivity of water molecules in the tissue and that can be used to map fiber tracts in the brain^{80, 81, 82}. DTI is non-invasive. It utilizes existing MRI technology and does not require the administration of a contrast agent. This technique exploits the sensitivity of MRI to random water diffusion in the brain tissue in the presence of diffusion gradient pulses that are incorporated into the MR imaging pulse sequence.

To understand diffusion it is important to understand the concept of 'phase'. Consider three sine waves (Figure 1.13) that are oscillating at the same rate but two of them are shifted along the x-axis. It can be said that the sine waves have the same frequency but different phase. Phase describes the instantaneous position of the sine wave within the cyclic variation. Similarly, phase in MRI refers to an angle and describes the position of the protons relative to each other. Immediately after the first 90° RF pulse, all the protons precess synchronously, they have a phase difference of 0° and are said to be in-phase (phase coherence). Due to T2 relaxation and susceptibility differences within tissue leading to magnetic field inhomogeneities, the phase coherence disappears and the protons are said to be out of phase (dephased). Figure 1.13 (a) shows the protons with same phase and (b) different phase.

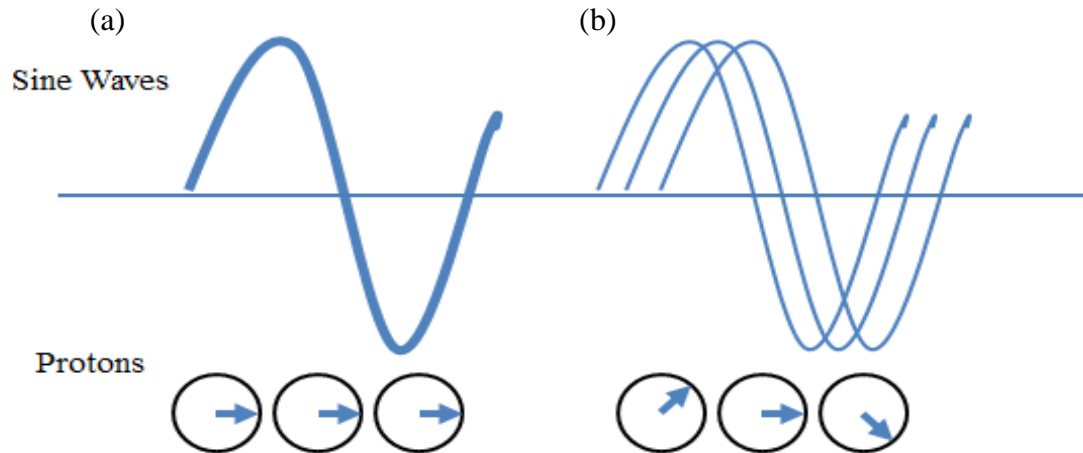


Figure 1.13 Sine waves and protons with (a) same phase and (b) different phase.

In DTI imaging, the 90° RF pulse generates a transverse magnetization that is purposely dephased by the application of a large diffusion gradient. If no diffusion is present, the protons do not move, and a second diffusion gradient is designed to rephase the magnetization completely. However, if diffusion occurs, the protons change their spatial position, and the second gradient does not perfectly rephase the magnetization. Since the gradients are controlled by the MRI pulse sequence, information about the diffusion process can be inferred by measuring the signal with (M) and without (M_0) diffusion gradients. Figure 1.14 below shows a basic spin echo MRI pulse sequence with the addition of diffusion gradients.

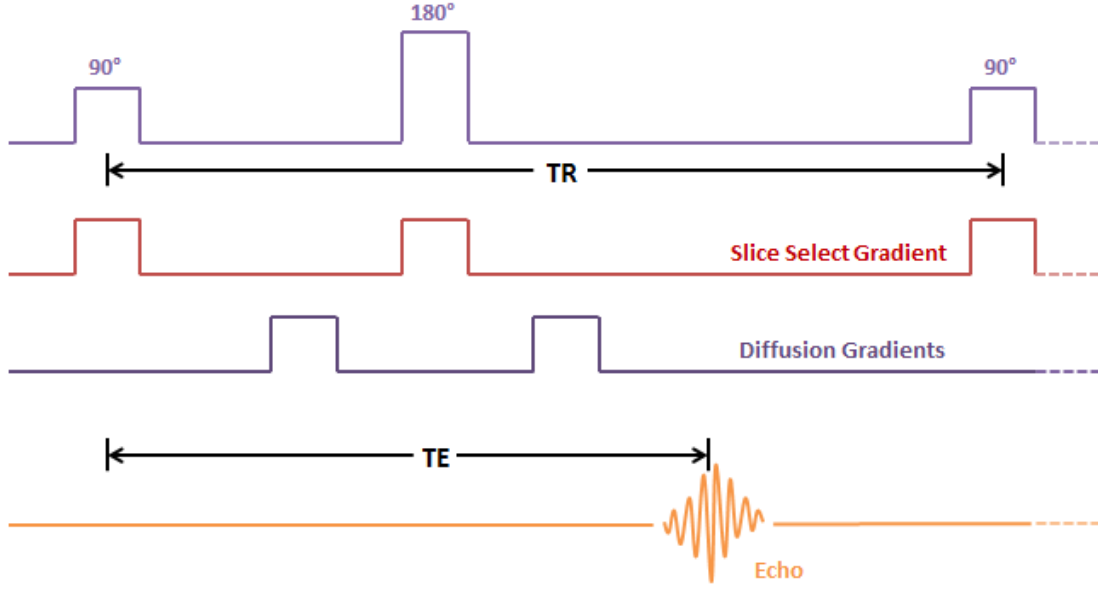


Figure 1.14 DTI sequence: spin echo sequence with the addition of diffusion gradients.

Diffusion in the anisotropic white matter is modeled as a second-order tensor (Figure 1.15). To quantify the second-order tensor, measurements are made in at least six non-collinear directions.

The diffusion tensor is calculated for each pixel according to the following equation^{83, 84}.

$$\frac{M}{M_0} = \exp(-\sum_{i=1}^6 \sum_{j=1}^6 b_{ij} D_{ij}) \quad [1.4]$$

D_{ij} are elements of the diffusion tensor matrix

b_{ij} are elements of the b matrix and is calculated as $b_{ij} = \gamma^2 \partial^2 G_i G_j (\Delta - \frac{\partial}{3})$

where $i, j = x, y, z$

The tensor can be diagonalized to obtain its eigenvalues ($\lambda_1, \lambda_2, \lambda_3$). The corresponding directions of these eigenvalues are the eigenvectors (e_1, e_2, e_3). The eigenvectors represent the tensor's principal coordinate, and the eigenvalues describe the shape and size of the tensor. Figure 1.15 below shows the diffusion tensor with the eigenvalues.

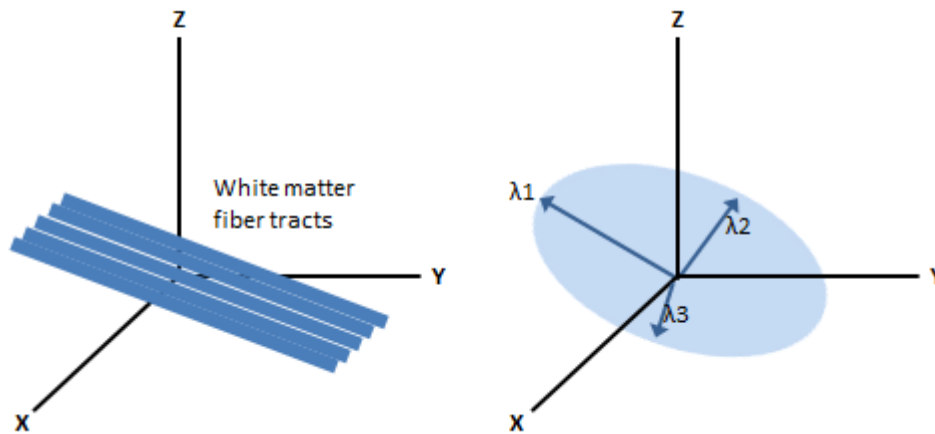


Figure 1.15 Diffusion tensor with eigen values $\lambda_1, \lambda_2, \lambda_3$. The diffusion is highly anisotropic in fibrous tissues such as white matter, and the direction of largest diffusivity is generally assumed to be parallel to the local direction of the white matter.

The eigen value information from the diffusion tensor measurements are used to calculate the following diffusion tensor parameters: mean diffusivity (MD), fractional anisotropy (FA), axial diffusivity (AxD) and radial diffusivity (RD) as shown in the following equations:

Mean Diffusivity (MD): The mean diffusivity is the average of the eigenvalues.

$$MD = \bar{\lambda} = (\lambda_1 + \lambda_2 + \lambda_3)/3 \quad [1.5]$$

Fractional Anisotropy (FA): The fractional anisotropy is the ratio of the anisotropic component of the diffusion tensor to the whole diffusion tensor

$$FA = \sqrt{\frac{3}{2}} \sqrt{\frac{(\lambda_1 - \bar{\lambda})^2 + (\lambda_2 - \bar{\lambda})^2 + (\lambda_3 - \bar{\lambda})^2}{\lambda_1^2 + \lambda_2^2 + \lambda_3^2}} \quad [1.6]$$

Axial Diffusivity (AxD): The axial diffusivity is the principal eigenvalue.

$$AxD = \lambda_1 \quad [1.7]$$

Radial Diffusivity (RD): The radial diffusivity is the average of the radial eigenvalues.

$$RD = \frac{(\lambda_2 + \lambda_3)}{2} \quad [1.8]$$

Table 1.3 Summary of the diffusion tensor parameters.

Diffusion Tensor Parameters	Formula	Description
Mean Diffusivity	$\frac{\lambda_1 + \lambda_2 + \lambda_3}{3}$	Average of the eigen values.
Fractional Anisotropy	$\sqrt{\frac{3}{2}} \sqrt{\frac{(\lambda_1 - \bar{\lambda})^2 + (\lambda_2 - \bar{\lambda})^2 + (\lambda_3 - \bar{\lambda})^2}{\lambda_1^2 + \lambda_2^2 + \lambda_3^2}}$	Ratio of the anisotropic component of the diffusion tensor to the whole diffusion tensor.
Axial Diffusivity	λ_1	Principal eigen value.
Radial Diffusivity	$\frac{(\lambda_2 + \lambda_3)}{2}$	Average of the middle and shorter eigen values.

Diffusion is considered isotropic when the eigenvalues are nearly equal. Conversely, the diffusion tensor is anisotropic when the eigenvalues are significantly different in

magnitude. The magnitudes of eigenvalues are affected by changes in local tissue microstructure that occurs due to normal physiological changes (i.e. aging) and also by different types of tissue injury or neurological diseases^{85, 86, 87}. Therefore, the parameters derived from the diffusion tensor may be a sensitive probe for characterizing both normal and abnormal tissue microstructure.

There has been strong interest in exploring the clinical applications of DTI in the assessment of brain tumors⁸⁸⁻⁹². DTI has been used for tumor grading⁹³ and tumor delineation⁹⁴. Functional diffusion maps have been used for early assessment of tumor response to treatment⁹⁵. DTI has also been used to differentiate between glioblastoma and metastasis⁹⁶. DTI studies have shown differences in DT parameters in GBM compared to MET⁹⁷. In some studies higher DT parameter values of FA, linear tensor (CL) and planar tensor (CP) and lower values of spherical tensor (CS) were observed in GBM and were useful for discriminating between the tumor types⁹⁸⁻¹⁰⁰.

1.4 Texture Analysis

Texture is an important characteristic of images and refers to the appearance of the image. Image texture is a function of the spatial variation of pixel intensities in an image^{101, 102}. Image texture analysis can provide quantitative information in the form of texture features that is not visible to human vision¹⁰³. Texture features are mathematical parameters computed from the distribution of pixels, which characterize the texture type in the image. The most common method of computing the image texture is to use a statistical based method that analyzes the properties of individual pixel intensities and their spatial distribution within the image¹⁰⁴.

Statistical based texture analyses are commonly classified as first-order and second-order textures, based on the number of pixels defining the local features. First-order textures estimate properties of individual pixel values, ignoring the spatial interaction between the neighboring image pixels, whereas second-order textures estimate properties of two or more pixel values occurring at specific locations relative to each other.

1.4.1 First-Order Textures

Textures based on first order statistics are features that can be computed from the gray level histogram. The histogram of an image is the count of the number of pixels in the image that possess a given grey-level value. Figure 1.16 shows an example gray-level histogram. The most common first-order texture features are the mean, standard deviation, skewness and kurtosis.

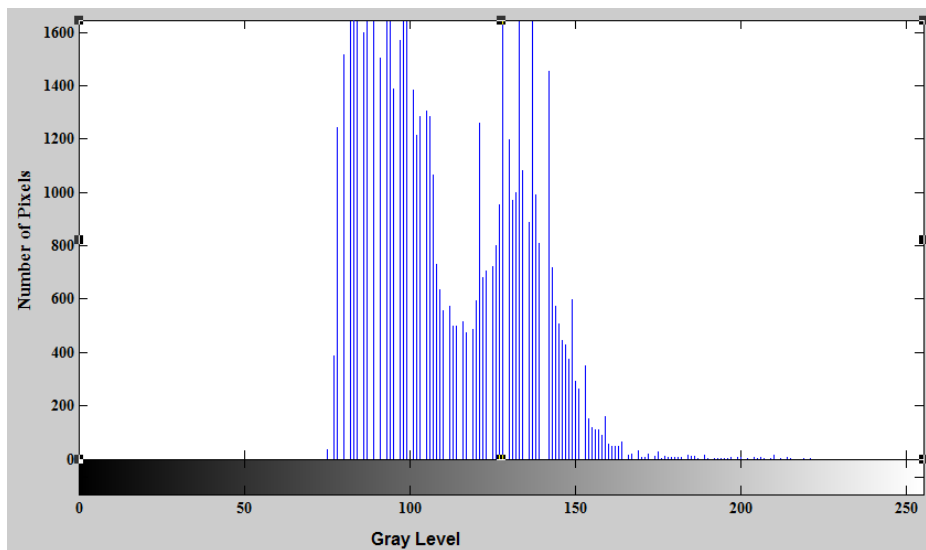


Figure 1.16 Gray-level histogram.

(1) Mean of the histogram is the mean of the gray-levels in an image.

$$\bar{x} = \frac{1}{n} \sum_{i=1}^n x_i \quad [1.9]$$

x = gray levels

n = number of gray-levels

(2) Standard deviation is a measure of how far from the mean the gray values in the image are distributed.

$$s = \sqrt{\frac{1}{n} \sum_{i=1}^n (x_i - \bar{x})^2} \quad [1.10]$$

(3) Skewness of the histogram refers to the asymmetry of the distribution of the gray values¹⁰⁵. A distribution is symmetric if the right side of the distribution is similar to the left side of the distribution. If the distribution is symmetric, then the skewness value is zero. A distribution with an asymmetric tail extending out to the right is referred to as positively skewed, while a distribution with an asymmetric tail extending out to the left is referred to as negatively skewed.

The skewness of a distribution is defined as:

$$sk = \frac{\frac{1}{n} \sum_{i=1}^n (x_i - \bar{x})^3}{\left[\sqrt{\frac{1}{n} \sum_{i=1}^n (x_i - \bar{x})^2} \right]^3} \quad [1.11]$$

(4) Kurtosis is a measure of how flat or peaked the top of a symmetric distribution is when compared to a normal distribution. If the grey level distribution is similar to the

normal distribution, the kurtosis value is 3. Flat-topped distributions are referred to as platykurtic and have a kurtosis value of less than 3, while less flat-topped distributions are referred to as leptokurtic and have a kurtosis value greater than 3.

The kurtosis of a distribution is defined as:

$$k = \frac{\frac{1}{n} \sum_{i=1}^n (x_i - \bar{x})^4}{\left[\sqrt{\frac{1}{n} \sum_{i=1}^n (x_i - \bar{x})^2} \right]^4} \quad [1.12]$$

The limitation of the histogram-based measurements is that they carry no information regarding the relative spatial position of pixels with one another. The spatial relationship of the pixels can be incorporated by taking in to account the distribution of intensities as well as the position of pixels with equal or nearly equal intensity values. This can be achieved by constructing a gray level co-occurrence matrix as explained in the next section.

1.4.2 Second-Order Textures

Textures based on second-order statistics are features that can be computed from the gray level co-occurrence matrix (GLCM). The GLCM is a two-dimensional histogram of gray-levels for a pair of pixels separated by a fixed distance (d) at a fixed angle (θ)^{103, 104}. It is an estimate of the joint probability $G(i, j)$ of the intensity values of two pixels (i and j), at a certain pixel distance apart along a given direction (i.e., the probability that i and j have the same intensity). This joint probability takes the form of a square matrix with row and column dimensions equal to the number of discrete gray levels (intensities) in the image. If an intensity image contained no texture (intensity variations) the resulting GLCM

would be completely diagonal. As the image texture increases (i.e. as the local pixel intensity variations increase), the off-diagonal values in the GLCM become larger. GLCMs are usually computed with neighboring pixels defined in angular directions 0° , 45° , 90° and 135° .

Figure 1.17 shows an example to construct a GLCM. Consider a 4x4 image (Figure 1.17a) with 4 gray-levels from 0 to 3 (Figure 1.17b). A generalized GLCM is shown in Figure 1.17c where (i, j) stands for the number of times gray-level i and j satisfy the condition stated by the offset distance vector d and angle θ .

The resulting four GLCMs for $d = [0 \ 1]$ and $[0 \ -1]$ and $\theta = 0^\circ, 45^\circ, 90^\circ, 135^\circ$ are shown in Figure 1.17d-g.



Figure 1.17a Sample image.

0	0	1	1
0	0	1	1
0	2	2	2
2	2	3	3

Figure 1.17b Gray-levels in the sample image.

(i, j)	0	1	2	3
0	(0,0)	(0, 1)	(0, 2)	(0, 3)
1	(1,0)	(1, 1)	(1, 2)	(1, 3)
2	(2,0)	(2, 1)	(2, 2)	(2, 3)
3	(3,0)	(3, 1)	(3, 2)	(3, 3)

Figure 1.17c: general form of a GLCM

4	2	1	0	4	1	0	0
2	4	0	0	1	2	2	0
1	0	6	1	0	2	4	1
0	0	1	2	0	0	1	0

Figure 1.17d: GLCM for $\theta = 0^\circ$

Figure 1.17e: GLCM for $\theta = 45^\circ$

6	0	2	0	2	1	3	0
0	4	2	0	1	2	1	0
2	2	2	2	3	1	0	2
0	0	2	0	0	0	2	0

Figure 1.17d: GLCM for $\theta = 90^\circ$

Figure 1.17e: GLCM for $\theta = 135^\circ$

GLCMs as seen above are symmetric matrices. Hence either upper or lower triangle is used for calculation of the second-order features. Each element in the GLCM is the

probability of co-occurrence of the pixel gray-levels. The second-order texture features can then be calculated using the formulas shown below.

Each of the five GLCM-based second-order texture features that are used in this thesis are described below:

(1) Entropy is the measure of randomness of the GLCM. It describes the amount of chaos or disorder within the elements of the GLCM. Entropy is higher when the image is non-uniform.

$$Entropy = -\sum_{i,j} G(i,j) \log_2 G(i,j) \quad [1.13]$$

$G(i, j)$ = probability of co- occurrence of the pixel gray-levels

(2) Homogeneity measures the closeness of the distribution of elements in the GLCM to the GLCM diagonal. It is also known as inverse difference moment. It is sensitive to the near diagonal elements of the GLCM. It is higher for a diagonal GLCM.

$$Homogeneity = \sum_{i,j} \frac{1}{1+|i-j|} G(i,j) \quad [1.14]$$

(3) Inertia measures the intensity or gray-level variation between the reference pixel and its neighbor over the whole image. It describes the local variations in the GLCM. It is inversely correlated to homogeneity and will be lower for a diagonal GLCM.

$$Inertia = \sum_{i,j} (i - j)^2 G(i,j) \quad [1.15]$$

(4) Correlation measures how correlated a reference pixel is to its neighbor over the whole image. It describes the joint probability occurrence of the specified pixel pairs. Correlation is 1 or -1 for a perfectly positively or negatively correlated image.

$$Correlation = \sum_{i,j} \frac{(i-\mu)(j-\mu)G(i,j)}{\sigma^2} \quad [1.16]$$

μ and σ are the mean and standard deviation.

(5) Energy describes the uniformity of the image. It measures the sum of squared elements of the GLCM. It is also known as angular second moment feature. Energy is high if the image is homogenous.

$$Energy = \sum_{i,j} G(i,j)^2 \quad [1.17]$$

1.4.3 Texture Analysis of Medical Images

MR images hold a large amount of texture information that may be relevant for clinical diagnosis. Due to its inherent resolution limitation, MR images are not capable of providing microscopic tissue information that can be evaluated visually. However, histological changes present in various diseases may generate textural changes in the MR image that can be quantified through texture analysis.

Image texture analysis has been used in a range of MR studies for classifying tissues in brain tumors. It has also been used to differentiate between different tumor grades¹⁰⁶ and discriminate between benign, malignant, and normal tissue types on MR images¹⁰⁷.

Texture analysis has been used to study the effects of traumatic brain injury on texture features¹⁰⁸. Genetic features have been discovered by texture analysis that could favor prognosis in low grade oligodendroglioma¹⁰⁹. Texture analysis has been used to segment structures in the normal brain^{110, 111} as well as in epilepsy to identify abnormalities in the hippocampus¹¹² by detecting differences in the texture features.

Image texture analysis has been used in a range of CT and MRI studies for classifying non- cerebral tissues. Texture analysis has been used on computed tomography (CT) images to detect microcalcification in breast cancer¹¹³, microcalcification susceptibility effects on breast MRI¹¹⁴, and to analyze breast tumors on contrast-enhanced MRI¹¹⁵. Texture differences were observed in MR images of the spinal cord between normal subjects and patients with relapsing multiple sclerosis before the atrophy was visually detectable¹¹⁶. Texture analysis has also been successfully applied to the classification of pathological tissues in the lungs¹¹⁷ and skeletal muscles¹¹⁸.

1.5 Thesis Objectives

1.5.1 Objective 1: Multiparametric imaging in patients with glioblastoma

Glioblastoma multiforme (GBM) is the most aggressive form of primary brain tumor. The current standard of care for patients with GBM is surgery followed by chemo- and radiation therapy. Since GBM is a grade IV tumor, recurrences are common even after the treatment. Radiation injury (RI), a side effect of radiation therapy and tumor recurrences appears hyperintense on conventional MR images. Differentiating between RI and tumor recurrences is important for treatment planning. Numerous techniques have been utilized trying to find biomarkers for differentiation, however biopsy is still the gold standard. The purpose of our current study was to determine whether a multiparametric characterization of tissue based on correlations of T2w signal intensity, FLAIR signal intensity, and diffusion tensor imaging parameters could differentiate RI from tumor recurrence.

1.5.2 Objective 2: Texture analysis in differentiating between glioblastoma and metastasis

Glioblastoma and metastasis are the two most common types of brain tumor. Both types of tumors exhibit similar radiologic appearance on routine MR images. Differentiating between GBM and MET is very important because they have different biological mechanisms and require different treatment strategies. Previous studies have focused on advanced imaging modalities, such as diffusion tensor imaging, perfusion MRI, MR spectroscopy and perfusion CT, that require longer scan times and expertise in advanced

imaging, which results in increased cost, examination time, and exposure to radiation.

The goal of our current study was to use texture based image analysis on routine MR images to provide quantitative information that can be used to differentiate between GBM and MET.

1.5.3 Objective 3: Texture analysis in patient selection for radiation therapy

Whole brain radiotherapy (WBRT) and stereotactic radiosurgery (SRS) is frequently used to treat metastatic brain tumors. However, SRS has side effects related to necrosis and edema, and requires separate and relatively invasive localization procedures. Helical tomotherapy (HT) allows for a SRS-type simultaneous infield boost (SIB) of multiple brain metastases, synchronously with WBRT and without separate stereotactic procedures. However, some patients' tumors may not respond to HT type WBRT+SIB, and would be more appropriately treated with radiosurgery or conventional surgery despite the additional risks and side effects. The goal of the current study was to investigate whether quantitative measurements of tumor size and appearance (including first- and second-order texture features) on a magnetic resonance imaging (MRI) scan acquired prior to treatment could be used to differentiate responder and non-responder lesions after HT type WBRT+SIB treatment of metastatic disease of the brain.

1.6 References

- [1] Louis DN, Ohgaki H, Wiestler OD, Cavenee WK, Burger PC, Jouvet A, Scheithauer BW, Kleihues P. The 2007 WHO classification of tumours of the central nervous system. *Acta Neuropathologica* 2007;114(2):97-109.
- [2] Yang I, Aghi MK. New advances that enable identification of glioblastoma recurrence. *Nature reviews in clinical oncology* 2009; 6:648-657.
- [3] S.K. Ray. *Glioblastoma: Molecular Mechanisms of Pathogenesis and Current Therapeutic Strategies*. Springer 2010.
- [4] Essig M, Weber MA, Tengg-Kobligk H, et al. Contrast-enhanced magnetic resonance imaging of central nervous system tumors: agents, mechanisms, and applications. *Top Magn Reson Imaging* 2006;17:89–106.
- [5] Stupp R, Mason WP, Van den Bent MJ, Weller M, Fisher B, Taphoorn MJ, Belanger K, Eishenhauer JG, Mirimanoff RO. European organization for research and treatment of cancer brain tumor and radiotherapy groups. *New England Journal of Medicine* 2005; 10, 352 (10): 987-96.
- [6] Baskar R, Lee KA, Y R, Yeoh KW. Cancer and radiation therapy: current advances and future directions. *International Journal of Medical Sciences* 2012; 9(3):193-199.
- [7] Gamulin M, Garaj-Vrhovac V, Kopjar N. Evaluation of DNA damage in radiotherapy-treated cancer patients using the alkaline comet assay. *Collegium Antropologicum*. 2007; 31(3):837-45.
- [8] Wong CS, Van der Kogel AJ. Mechanisms of radiation injury to the central nervous system: mechanisms for neuroprotection. *Molecular Interventions*. 2004; 4(5): 273-284

- [9] Langleban DD, Segall GM. PET in differentiation of recurrent brain tumor from radiation injury. *The Journal of nuclear medicine* 2000; 41(11):1861-7.
- [10] Chamberlain MC, Glantz MJ, Chalmers L, Van Horn A, Sloan AE. Early necrosis following concurrent Temodar and radiotherapy in patients with glioblastoma. *J Neurooncology* 2007;82(1):81–83.
- [11] Gasparetto EL, Pawlak MA, Patel SH,. Post treatment recurrence of malignant brain neoplasm: accuracy of relative cerebral blood volume fraction in discriminating low from high malignant histologic volume fraction. *Radiology* 2009;250(3):887–896.
- [12] Kashimura H, Inoue T, Beppu T, et al. Diffusion tensor imaging for differentiation of recurrent brain tumor and radiation necrosis after radiotherapy—three case reports. *Clinical neurology and neurosurgery* 2007; 109:106-110.
- [13] Kumar AJ, Leeds NE, Fuller GN, et al. Malignant gliomas: MR imaging spectrum of radiation therapy- and chemotherapy-induced necrosis of the brain after treatment. *Radiology* 2000;217:377–384.
- [14] Mullins ME, Barest GD, Schaefer PW, et al. Radiation necrosis versus. glioma recurrence: Conventional MR imaging clues to diagnosis. *Am J Neuroradiol.* 2005;26:1967–72.
- [15] Rogers LR, Scarpace L, Gutierrez J, et al. Magnetic resonance imaging characteristics and histological correlates of cerebral radiation necrosis. *Neurology.* 2006;66(2):335.
- [16] Jain R, Scarpace L, Ellika S. First-pass perfusion computed tomography: initial experience in differentiating recurrent brain tumors from radiation effects and radiation necrosis. *Neurosurgery* 2007;61:778–786.
- [17] Jain R, Narang J, Schultz L. Permeability estimates in histopathology proven treatment induced necrosis using perfusion CT: Can these add to other perfusion

- parameters in differentiating from recurrent/progressive tumors? *AJNR Am J Neuroradiology* 2011;32:658–663.
- [18] Sugahara T, Korogi Y, Tomiguchi S. Post therapeutic intra axial brain tumor: the value of perfusion-sensitive contrast enhanced MR imaging for differentiating tumor recurrence from non-neoplastic contrast-enhancing tissue. *AJNR Am J Neuroradiol.* 2000;21:901–909.
 - [19] Barajas RF, Chang JS, Sneed PK. Distinguishing recurrent intra-axial metastatic tumor from radiation necrosis following gamma knife radiosurgery using dynamic susceptibility-weighted contrast-enhanced perfusion MR imaging. *AJNR Am J Neuroradiol.* 2009;30:367–372.
 - [20] Hein PA, Eskey CJ, Dunn JF. Diffusion weighted imaging in the follow-up of treated high-grade gliomas: Tumor recurrence versus radiation injury. *Am J Neuroradiology* 2004;25:201–209.
 - [21] Rock JP, Scarpace L, Hearshen D. Associations among magnetic resonance spectroscopy, apparent diffusion coefficients, and image guided histopathology with special attention to radiation necrosis. *Neurosurgery* 2004; 54:1111–1117.
 - [22] Graves EE, Nelson SJ, Vigneron DB. Serial proton MR spectroscopic imaging of recurrent malignant gliomas after gamma knife radiosurgery. *American Journal of Neuroradiology* 2001;22:613–624.
 - [23] Rabinov JD, Lee PL, Barker FG. In vivo 3-T MR spectroscopy in the distinction of recurrent glioma versus radiation effects: Initial experience. *Radiology* 2002; 225: 871–879.
 - [24] Chao ST, Suh JH, Raja S. The sensitivity and specificity of FDG PET in distinguishing recurrent brain tumor from radionecrosis in patients treated with stereotactic radiosurgery. *Int J Cancer* 2001;96:191–197.

- [25] Tsuyuguchi N, Sunada I, Iwai Y. Methionine positron emission tomography of recurrent metastatic brain tumor and radiation necrosis after stereotactic radiosurgery: is a differential diagnosis possible? *J Neurosurg.* 2003;98:1056–1064.
- [26] Narang J, Jain R, Arbab AS, Mikkelsen T, Scarpace L, Rosenblum ML, Hearshen D, Babajani-Feremi A. Differentiating treatment-induced necrosis from recurrent/progressive brain tumor using nonmodel-based semiquantitative indices derived from dynamic contrast-enhanced T1-weighted MR perfusion. *Neuro-oncology* 2011, 13(9), 1037-1046.
- [27] Zeng QS, Li CF, Liu H, Zhen JH, Feng DC. Distinction between recurrent glioma and radiation injury using magnetic resonance spectroscopy in combination with diffusion weighted imaging. *Int. J. Radiation Oncology Biol. Phys.* 2007; 68(1): 151–158.
- [28] Schwartz RB, Carvalho PA, Alexander E 3rd, Loeffler JS, Folkerth R, Holman BL. Radiation necrosis vs high-grade recurrent glioma: differentiation by using dual-isotope SPECT with ²⁰¹Tl and ^{99m}Tc-HMPAO. *AJNR Am J Neuroradiol.* 1991 Nov-Dec;12(6):1187-92.
- [29] Samnick S, Bader JB, Hellwig D, Moringlane JR, Alexander C, Romeike BF, Feiden W, Kirsch CM.. Clinical Value of Iodine-123-Alpha-Methyl-L-Tyrosine Single-Photon Emission Tomography in the Differential Diagnosis of Recurrent Brain Tumor in Patients Pretreated for Glioma at Follow-Up. *Journal of Clinical Oncology* 2002; 20(2):396-404.
- [30] Barnholtz-Sloan JS, Sloan AE, Davis FG, Vignea FD, Lai P, Sawaya RE. Incidence proportions of brain metastases in patients diagnosed (1973 to 2001) in the metropolitan Detroit cancer surveillance system. *Journal of Clinical Oncology* 2004; 22(14):2865–72.

- [31] Patel TR, McHugh BJ, Bi WL, Minja FJ, Knisely JP, Chiang VL. A comprehensive review of MR imaging changes following radiosurgery to 500 brain metastases. *AJNR Am J Neuroradiol.* 2011. 32(10):1885-92.
- [32] Eichler AF, Loeffler JS. Multidisciplinary management of brain metastases. *Oncologist* 2007; 12(7):884-98.
- [33] Asai A, Matsutani M, Kohno T, Nakamura O, Tanaka H, Fujimaki T, Funada N, Matsuda T, Nagata K, Takakura K.. Subacute brain atrophy after radiation therapy for malignant brain tumor. *Cancer* 1989; 63(10):1962-74.
- [34] Sneed PK, Lamborn KR, Forstner JM, McDermott MW, Chang S, Park E, Gutin PH, Phillips TL, Wara WM, Larson DA. Radiosurgery for brain metastases: is whole brain radiotherapy necessary? *Int J Radiat Oncol Biol Phys* 1999; 43(3):549-58.
- [35] Rodrigues G, Yartsev S, Yaremko B, Perera F, Dar AR, Hammond A, Lock M, Yu E, Ash R, Caudrelier JM, Khuntia D, Bailey L, Bauman G. Phase I trial of simultaneous in-field boost with helical tomotherapy for patients with one to three brain metastases. *International Journal of Radiation Oncology Biology Physics* 2011; 80(4):1128-33.
- [36] Lagerwaard F, Van der hoorn EA, Verbakel WF, Haasbeek CJ, Slotman BJ, Senan S. Whole brain radiotherapy with simultaneous integrated boost to multiple brain metastases using volumetric modulated arc therapy. *Int J Radiat Oncol Biol Phys* 2009; 75(1):253–9.
- [37] Hall EJ, Brenner DJ. The radiobiology of radiosurgery: rationale for different treatment regimes for AVMs and malignancies. *Int J Radiat Oncol Biol Phys* 1993; 25(2):381–5.
- [38] Levegrun S, Pottgen C, Wittig A, Lubcke W, Jawad JA, Stuschke M., Helical Tomotherapy for Whole-Brain Irradiation With Integrated Boost to Multiple Brain

Metastases: Evaluation of Dose Distribution Characteristics and Comparison With Alternative Techniques. *Int Journal of Radiation oncology biology and Physics* 2013; 86(4): 734-742.

- [39] Sterzing F, Schubert K, Sroka-Perez G, Kalz J, Debus J, Herfarth K. Helical Tomotherapy. *Strahlentherapie und Onkologie* 2008; 184(1):8-14.
- [40] Provenzale JM, Mukundan S, Barboriak DP. Diffusion-weighted and perfusion MR imaging for brain tumor characterization and assessment of treatment response. *Radiology* 2006; 239: 632-649.
- [41] Sorenson GA, Batchelor TT, Wen PY, Zhang WT, Jain RK. Response criteria for glioma. *Nature* 2008; 5(11): 634-644.
- [42] Wen PY, Macdonald DR, Reardon DA, Cloughesy TF, Mikkelsen, Wong ET, Chamberlain MC, Stupp R, Bent MJ, Chang S. Updated response assessment criteria for high-grade gliomas: response assessment in neuro-oncology working group. *Journal of Clinical Oncology* 2010; 28(11):1963-72
- [43] Eisenhauer EA, Therasse P, Bogaerts J, Schwartz LH, Sargent D, Ford R, Dancey J, Arbuck S, Gwyther S, Mooney M, Rubinstein L, Shanker L, Dodd L, Kaplan R, Lacombe D, Verweij J. New response evaluation criteria in solid tumors: revised RECIST guideline (version 1.1). *European Journal of Cancer* 2009; 45(2):228–47.
- [44] Therasse P, Arbuck SG, Eisenhauer EA. New guidelines to evaluate response to treatment in solid tumors: European Organization for Research and Treatment of Cancer, National Cancer Institute of the United States, National Cancer Institute of Canada. *J Natl Cancer Inst* 2000;92:205– 216.
- [45] Sorenson AG, Patel S, Harmath C, et al. Comparison of diameter and perimeter methods for tumor volume calculation. *J Clin Oncol* 2001;19:551–557.
- [46] Galanis E, Buckner JC, Maurer MJ, et al. Validation of neuroradiologic response assessment in gliomas: measurement by RECIST, two dimensional, computer-

assisted tumor area, and computer-assisted tumor volume methods. *Neuro Oncol* 2006;8:156–165.

- [47] Roberts HC, Roberts TP, Lee TY, Dillon WP. Dynamic contrast-enhanced CT of human brain tumors: quantitative assessment of blood volume, blood flow and microvascular permeability—report of two cases. *AJNR Am J Neuroradiol* 2002; 23:828–832.
- [48] Roberts HC, Roberts TP, Lee TY, Dillon WP. Dynamic contrast-enhanced computed tomography (CT) for quantitative assessment of microvascular permeability in human brain tumors. *Acad Radiol* 2002; 9(suppl 2):S364–S367.
- [49] Roberts HC, Roberts TP, Brasch RC, Dillon WP. Quantitative measurement of microvascular permeability in human brain tumors achieved using dynamic contrast-enhanced MR imaging: correlation with histologic grade. *AJNR Am J Neuroradiol* 2000; 21:891–899.
- [50] Roberts HC, Roberts TP, Ley S, Dillon WP, Brasch RC. Quantitative estimation of microvascular permeability in human brain tumors: correlation of dynamic Gd-DTPA-enhanced MR imaging with histopathologic grading. *Acad Radiol* 9(suppl 1):S151–S155, 2002.
- [51] Padhani AR, Neeman M. Challenges for imaging angiogenesis. *Br J Radiology* 2001; 74:886–890.
- [52] Miles KA. Functional computed tomography in oncology. *Eur J Cancer* 2002; 38:2079–84.
- [53] Miles KA, Griffiths MR. Perfusion CT: a worthwhile enhancement? *Br J Radiol.* 2003;76:220–31.
- [54] Jain R, Ellika SK, Scarpace L, et al. Quantitative estimation of permeability surface-area product in astroglial brain tumors using perfusion CT and correlation with histopathologic grade. *AJNR Am J Neuroradiol* 2008;29:694–700.

- [55] Law M, Oh S, Johnson G, et al. Perfusion magnetic resonance imaging predicts patient outcome as an adjunct to histopathology: a second reference standard in the surgical and nonsurgical treatment of low-grade gliomas. *Neurosurgery* 2006;58:1099–10.
- [56] Miles KA, Charnsangavej C, Lee F, Fishman E, Horton K, Lee T-Y. Application of CT in the investigation of angiogenesis in oncology. *Acad Radiol* 2000;7:840–50.
- [57] Miles KA. Tumour angiogenesis and its relation to contrast enhancement on computed tomography: a review. *Eur J Radiol* 1999;30:198–205.
- [58] Wintermark M, Thiran JP, Maeder P, Schnyder P, Meuli R. Simultaneous measurement of regional cerebral blood flow by perfusion CT and stable xenon CT: a validation study. *Am J Neuroradiol* 2001; 22: 905-14.
- [59] Kudo K, Terae S, Katoh C, et al. Quantitative cerebral blood flow measurement with dynamic perfusion CT using the vascular-pixel elimination method: comparison with H₂(15)O positron emission tomography. *Am J Neuroradiol* 2003; 24: 419-26.
- [60] Cenic A, Nabavi DG, Craen RA, Gelb AW, Lee TY. Dynamic CT measurement of cerebral blood flow: a validation study. *Am J Neuroradiol* 1999;20:63–73.
- [61] Cenic A, Nabavi DG, Craen RA, Gelb AW, Lee TY. A CT method to measure hemodynamics in brain tumors: validation and application of cerebral blood flow maps. *Am J Neuroradiol* 2000;21:462–70.
- [62] Hattori H, Miyoshi T, Okada J, Yoshikawa K, Arimizu N, Hattori N. Tumor blood flow measured using dynamic computed tomography. *Invest Radiology* 1994;29:873–6.

- [63] Nabavi DG, Cenic A, Dool J, Smith RM, Espinosa F, Craen RA, et al. Quantitative assessment of cerebral hemodynamics using CT: stability, accuracy, and precision studies in dogs. *J Comput Assist Tomogr* 1999;23:506–15.
- [64] Gillard JH, Antoun NM, Burnet NG, Pickard JD. Reproducibility of quantitative CT perfusion imaging. *Br J Radiol* 2001;74:552–5.
- [65] Hermans R, Lambin P, Van den Bogaert W, Haustermans K, Van der Goten A, Baert AL. Non-invasive tumour perfusion measurement by dynamic CT: preliminary results. *Radiother Oncol* 1997;44:159–62.
- [66] Dugdale PE, Miles KA, Kelley BB, Bunce IH, Leggett DAC. CT measurements of perfusion and permeability within lymphoma masses: relationship to grade, activity and chemotherapeutic response. *J Comput Assist Tomogr* 1999;23:540–7.
- [67] Leggett DA, Miles KA, Kelley BB. Blood-brain barrier and blood volume imaging of cerebral glioma using functional CT: a pictorial review. *Australas Radiol* 1998;42: 335–40.
- [68] Ma JH, Kim HS, Rim NJ, et al. Differentiation among glioblastoma multiforme, solitary metastatic tumor, and lymphoma using whole-tumor histogram analysis of the normalized cerebral blood volume in enhancing and perienhancing lesions. *AJNR Am J Neuroradiol* 2010;31:1699–706.
- [69] Blasel S, Jurcoane A, Franz K, et al. Elevated peritumoural rCBV values as a mean to differentiate metastases from high-grade gliomas. *Acta Neurochir(Wien)* 2010;152:1893–99.
- [70] Law M, Cha S, Knopp EA, Johnson G, Arnett J, Litt AW. High-grade gliomas and solitary metastases: differentiation by using perfusion and proton spectroscopic MR imaging. *Radiology*.2002; 222(3):715-21.
- [71] Cha S, Lupo JM, Chen MH, et al. Differentiation of glioblastoma multiforme and single brain metastasis by peak height and percentage of signal intensity recovery

derived from dynamic susceptibility-weighted contrast-enhanced perfusion MR imaging. *AJNR Am J Neuroradiol*, 2007; 28:1078–84.

- [72] Marinus T. Vlardingerbroek, Jaques A. den Boer, *Magnetic resonance imaging, Theory and practice*, Springer, 3rd edition. 2003.
- [73] Edelman hesselink, zlatkin. *Clinical magnetic resonance imaging vol one*. Second edition. W. B Saunders company, 2nd edition, 1996.
- [74] D.G. Mitchell, M. Cohen, *MRI Principles*, Saunders, Philadelphia, 2nd ed. 2004.
- [75] Sartor K. MR imaging of the brain: tumors. *EurRadiol*. 1999;9:1047–54.
- [76] Sinha S, Bastin ME, Whittle IR, Wardlaw JM. Diffusion tensor MR imaging of high-grade cerebral gliomas. *AJNR Am J Neuroradiol* 2002;23:520–527.
- [77] Tropine A, Vucurevic G, Delani P, et al. Contribution of diffusion tensor imaging to delineation of gliomas and glioblastomas. *J Magn Reson Imaging* 2004; 20:905–912.
- [78] Lee HY, Na DC, Song IC, Lee DH, Seo HS, Kim J, Chang KH. Diffusion-Tensor Imaging for Glioma Grading at 3-T Magnetic Resonance Imaging: Analysis of Fractional Anisotropy and Mean Diffusivity. *J Comput Assist Tomography*. 2008; 32(2), 298-303.
- [79] Opstad KS, Murphy MM, Wilkins PR, et al. Differentiation of metastases from high-grade gliomas using short echo time 1H spectroscopy. *J Magn Reson Imaging* 2004; 20:187–92.
- [80] Basser PJ, Mattiello J, LeBihan D. Estimation of the effective self diffusion tensor from the NMR spin echo. *J Magn Reson B* 1994; 103:247–254.
- [81] Basser PJ, Pajevic S, Pierpaoli C, Duda J, Aldroubi A. In vivo fiber tractography using DT-MRI data. *Magn Reson Med* 2000; 44:625-63.

- [82] Le Bihan D, Mangin JF, Poupon C, et al. Diffusion tensor imaging: concepts and applications. *J Magn Reson Imaging*.2001; 13:534-546.
- [83] Basser PJ, Mattiello J, LeBihan D. Estimation of the effective self-diffusion tensor from the NMR spin echo. *J Magn Reson B*. Mar. 103(3):247-54, 1994.
- [84] Counsell SJ, Shen Y, Boardman JP, Larkman DJ, Kapellou O, Ward P, Allsop JM, Cowan FM, Hajnal JV, Edwards AD, Rutherford MA. Axial and Radial Diffusivity in Preterm Infants Who Have Diffuse White Matter Changes on Magnetic Resonance Imaging at Term-Equivalent Age 2006; 117(2):376-386.
- [85] Alexander AL, Lee JE, Lazar M, Field AS. Diffusion Tensor Imaging of the Brain. *Neurotherapeutics* 2007; 4(3):316-329.
- [86] Davis, S.W., Dennis, N.A., Buchler, N.E.G., Madden, D.J., White, L.E., Cabeza, R. Assessing the effects of aging on long white matter tracts using diffusion tensor imaging (DTI) tractography. *Neuroimage* 2009; 46:530-541.
- [87] Niogi SN, Mukherjee P. Diffusion tensor imaging of mild traumatic brain injury. *J Head Trauma Rehabil* 2010;25(4):241-55.
- [88] Field AS, Alexander AL, Wu YC, Hasan KM, Witwer B, Badie B. Diffusion tensor eigenvector directional color imaging patterns in the evaluation of cerebral white matter tracts altered by tumor. *J Magn Reson Imaging* 2004; 20:555–562.
- [89] Lu S, Ahn D, Johnson G, Law M, Zagzag D, Grossman RI. Diffusion tensor MR imaging of intracranial neoplasia and associated peritumoral edema: introduction of the tumor infiltration index. *Radiology* 2004; 232:221–228.
- [90] Sinha S, Bastin ME, Whittle IR, Wardlaw JM. Diffusion tensor MR imaging of high-grade cerebral gliomas. *AJNR Am J Neuroradiol* 2002; 23:520–527.

- [91] Tropine A, Vucurevic G, Delani P, et al. Contribution of diffusion tensor imaging to delineation of gliomas and glioblastomas. *J Magn Reson Imaging* 2004; 20:905–912.
- [92] Tummala RP, Chu RM, Liu H, Truwit CL, Hall WA. Application of diffusion tensor imaging to magnetic-resonance-guided brain tumor resection. *Pediatr Neurosurg* 2003;39:39–43.
- [93] Lee HY, Na DC, Song IC, Lee DH, Seo HS, Kim J, Chang KH. Diffusion-Tensor Imaging for Glioma Grading at 3-T Magnetic Resonance Imaging: Analysis of Fractional Anisotropy and Mean Diffusivity. *J Comput Assist Tomography*. 32(2), 298-303. March/April 2008.
- [94] Tropine A, Vucurevic G, Delani P, et al. Contribution of diffusion tensor imaging to delineation of gliomas and glioblastomas. *J Magn Reson Imaging*, 20:905–912, 2004.
- [95] Moffat BA, Chenevert TL, Lawrence TS, Meyer CR, Johnson TD, Dong Q, Tsien C, Mukherji S, Quint DJ, Gebarski SS, Robertson PL, Junck LR, Rehemtulla A, Ross BD. Functional diffusion map: A noninvasive MRI biomarker for early stratification of clinical brain tumor response. *PNAS* 102(15), 5524-5529. April 2005.
- [96] WangS, Kim S, Chawla S, et al. Differentiation between glioblastomas, solitary brain metastases, and primary cerebral lymphomas using diffusion tensor and dynamic susceptibility contrast-enhanced MR imaging. *AJNR Am J Neuroradiol*, 2011; 32: 507–14.
- [97] Byrnes TJ, Barrick TR, Bell BA, et al. Diffusion tensor imaging discriminates between glioblastoma and cerebral metastases in vivo. *NMR Biomed* 2011, 24: 54–60.

- [98] Toh CH, Wei KC, Ng SH, et al. Differentiation of brain abscesses from necrotic glioblastomas and cystic metastatic brain tumors with diffusion tensor imaging. *AJNR Am J Neuroradiol* 2011; 32:1646–51.
- [99] Wang S, Kim S, Chawla S, et al. Differentiation between glioblastomas, solitary brain metastases, and primary cerebral lymphomas using diffusion tensor and dynamic susceptibility contrast-enhanced MR imaging. *AJNR Am J Neuroradiol* 2011; 32: 507–14.
- [100] Tsuchiya K, Fujikawa A, Nakajima M, et al. Differentiation between solitary brain metastasis and high-grade glioma by diffusion tensor imaging. *Br J Radiol*. 2005; 78:533–37.
- [101] Connors RW, Harlow CA. A theoretical comparison of texture algorithm. *IEEE Transactions in Pattern Analysis and Machine Learning* 1980; 2(3), 204–22.
- [102] Kjer L, Ring P, Thomsen, Henriksen O. Texture analysis in quantitative MR imaging: tissue characterisation of normal brain and intracranial tumours at 1.5 T. *Acta Radiologica* 1995; 36(2):127-35.
- [103] Haralick RM, Shanmugam K, Dinstein I. Textural features for image classification *IEEE Transactions on Systems, man and cybernetics* 1973; 3(6): 610–621.
- [104] Haralick RM. Statistical and structural approaches to textures. *Proceedings of the IEEE*. 67(5). May 1979 pg 786-803.
- [105] <http://www.mathworks.com/help/stats>
- [106] Zacharaki EI, Wang S, Chawla S, Yoo DS, Wolf R, Melhem ER, Davatzikos C. Classification of brain tumor type and grade using MRI texture and shape in a machine learning scheme. *Magnetic Resonance in Medicine* (December 2009), 62 (6), pg. 1609-1618.

- [107] Herlidou-Meme S, Constans JM, Carsin B, Olivie D, Eliat PA, Nadal-Desbarats L, Gondry C, Le Rumeur E, Idy-Peretti I, De Certaines JD. MRI texture analysis on texture test objects, normal brain and intracranial tumors. *Magnetic Resonance Imaging*. 21: 989–993, 2003.
- [108] Holli KK, Harrison L, Dastidar P, Waljas M, Liimatainen S, Luukkaala T, Ohman J, Soimakallio S, Eskola H. Texture analysis of MR images of patients with mild traumatic brain injury. *Biomedical central medical imaging*. 10(8). 1-10. 2010.
- [109] Brown R, Zlatescu M, Sijben A, Roldan G, Easaw J, Forsyth P, Parney I, Sevic R, Yan E, Demetrick D, Schiff D, Cairncross G, Mitchell R. The use of magnetic resonance imaging to noninvasively detect genetic signatures in oligodendroglioma. *Clin Cancer Res*, 14(8):2357–2362, April 2008.
- [110] Saeed N, Puri BK. Cerebellum segmentation employing texture properties and knowledge based image processing: applied to normal adult controls and patients. *Magn Reson Imaging* 2002; 20:425–9.
- [111] Alejo RP, Ruiz-Cabello J, Cortijo M, et al. Computer-assisted enhanced volumetric segmentation magnetic resonance imaging data using a mixture of artificial neural networks. *Magn Reson Imaging* 2003; 21:901–12.
- [112] Yu O, Mauss Y, Namer IJ, Chambron J. Existence of contralateral abnormalities revealed by texture analysis in unilateral intractable hippocampal epilepsy. *Magn Reson Imaging* 2001;19:1305–10.
- [113] Kulkarni DA, Bhagyashree SM, Udupi GR. Texture Analysis of mammographic images. *International journal of computer applications* 2010; 5(6):12-17.
- [114] James D, Clymer BD, Schmalbrock P. Texture detection of simulated microcalcification susceptibility effects in magnetic resonance imaging of breasts. *J Magn Reson Imaging* 2001; 13:876–81.

- [115] Sinha S, Lucas-Quesada FA, DeBruhl ND, et al. Multifeature analysis of Gd-enhanced MR images of breast lesions. *J Magn Reson Imaging* 1997; 7:1016–26.
- [116] Mathias JM, Tofts PS, Losseff NA. Texture analysis of spinal cord pathology in multiple sclerosis. *Magn Reson Med* 1999; 42:929–35.
- [117] Chabat F, Yang G-Z, Hansell DM. Obstructive lung diseases: texture classification for differentiation at CT. *Radiology* 2003; 228:871–7.
- [118] Herlidou S, Rolland Y, Bansard JY, Le Rumeur E, DeCertaïnes JD. Comparison of automated and visual texture analysis in MRI: characterization of normal and diseased skeletal muscle. *Magn Reson Imaging* 1999; 17:1393–7.

2 Analysis of morphological MRI parameters and diffusion tensor parameters for perfusion CT derived high permeability areas in glioblastoma: identifying tumor recurrence from radiation induced necrosis

2.1 Introduction

Glioblastoma multiforme (GBM) is the most lethal and aggressive form of primary brain tumor. Median survival for patients with glioblastoma is 12-15 months¹. Treatment options are determined by tumor size, location, and associated symptoms. Advances in brain tumor treatment have led to aggressive management strategies utilizing combinations of surgery, chemotherapy, and radiation therapy. The current standard of care for patients with GBM is surgical resection of the tumor followed by radiation therapy and concomitant and adjuvant temozolomide chemotherapy. This approach has been shown to standardize the treatment protocol and prolong the overall survival for patients². Radiation Injury (RI) is an undesirable but unavoidable side effect of treatment that appears as enhancing lesions following contrast agent injection on magnetic resonance imaging (MRI). Since GBM is a high grade tumor, recurrences are common after treatment, and these recurrences also manifest as hyperintense regions on MRI after contrast agent injection. Therefore the presence of enhancing lesions after radiation therapy may represent either tumor recurrence or radiation induced injury^{3, 4}. Similarly, both recurrent tumor and radiation are also known to produce hyperintense regions on T2-weighted (T2w) and fluid attenuated inversion recovery (FLAIR) MRI. Although

important for treatment planning and prognosis, differentiating between tumor recurrence and RI can be difficult with conventional MRI⁵.

Currently tumor biopsy or histology is the gold standard for differentiating tumor from RI. There have been various attempts to differentiate tumor recurrences from RI in the past using in-vivo morphologic imaging as well as various functional imaging techniques such as CT perfusion, MR perfusion, diffusion weighted imaging, magnetic resonance spectroscopy (MRS), single-photon emission computed tomography, and positron emission tomography^{5, 6-18}. However, each modality has its limitations and therefore the search for an accurate and easy to implement technique continues¹⁹.

Numerous studies have successfully correlated CT perfusion properties of the tumor with histology and shown that progressive or recurrent tumors have high permeability (PS) compared to RI regions²⁰⁻²². CT has been widely used to obtain perfusion information in brain tumor, but it has several disadvantages that include additional cost, examination time, and increased exposure to radiation. Since MRI is part of routine brain tumor imaging, an MRI technique that provides similar information would be advantageous.

The purpose of the current study was to determine whether a multiparametric characterization of tissue based on T2w signal intensity, FLAIR signal intensity, and diffusion tensor imaging parameters could differentiate RI from tumor recurrence. Tumor recurrence was defined as tissue with high permeability and high blood volume measured by CT perfusion. RI was defined as tissue with low permeability measured by CT perfusion that was hyperintense on FLAIR MRI²³⁻²⁴. We hypothesized that

correlations between MRI parameters could identify regions of high vascular permeability and therefore could differentiate RI from tumor recurrence.

2.2 Methods

This study was approved by the University of Western Ontario Health Sciences Research Ethics Board. All patients provided written informed consent prior to imaging. Twelve patients with glioblastoma multiforme were recruited for the study. Patients were eligible for this study if they met the following criteria: histologically proven cancer before radiation and chemotherapy, magnetic resonance imaging findings on follow-up clinical MRI and clinical presentation consistent with glioblastoma. Patients underwent a perfusion CT scan and a 3 Tesla MRI. Of the twelve patients, two did not complete the perfusion CT scan and two patients showed no increase in permeability values and therefore could not be used in the analysis. Higher permeability values were approximately ten times the normal values. Table 2.1 shows the patient demographics and tumor location.

Table 2.1 Patient demographics and clinical information.

Patient	Gender, Age	Brain tumor location
1	M, 44	Lt. Parietal
2	M, 46	Lt. Parietal, Corpus Callosum
3	M, 57	Lt. Parieto-Occipital
4	M, 50	Lt. Temporal
5	F, 64	Rt. Parietal
6	M, 56	Lt. Temporal
7	F, 63	Rt. Temporal-Occipital
8	M, 43	Rt. Frontal

MR imaging was performed on a 3T Tim Trio MRI system (Siemens Medical Systems, Erlangen, Germany) with a 32-channel head coil. The MR imaging protocol included the following sequences: transverse T2-weighted (T2w) fast spin-echo (repetition time= 6000 ms, echo time = 93 ms, field of view = 220 mm, slice thickness = 2 mm; matrix = 320 × 320), transverse FLAIR (repetition time = 9000 ms, inversion time = 2500 ms, echo time = 91 ms, field of view = 256 mm, slice thickness = 5 mm; matrix = 256 x 256), and

diffusion-weighted spin-echo imaging (repetition time = 7500 ms, echo time = 90 ms, number of directions = 64, field of view = 256 mm, b-value = 1000, slice thickness = 2 mm; matrix = 128x128).

2.2.1 CT Perfusion Imaging

The patients were scanned on a GE CT scanner (GE LightSpeed VCT; GE Healthcare, Waukesha, WI) with a nonionic contrast bolus (Iomeron, 350 mg iodine/mL, 40 mL; Bracco Imaging Scandinavia, Goteborg, Sweden). A two-phase CT perfusion scan, guided by a prior non-contrast CT scan that identified eight 5 mm sections to cover the tumor, was performed for each patient. The bolus of contrast was injected into the vein at a rate of 2 to 4 mL/s at 3 to 5 seconds after the first phase started. The preselected brain sections were scanned for 45 seconds at 1-second intervals during the first phase and for a period of 105 seconds at 15-second intervals during the second phase. All patients were scanned at 80 kVp with a 250 mm field of view.

2.2.2 Data Analysis

The CT perfusion studies were analyzed using the prototype version of CT Perfusion 4D software (GE Healthcare, Waukesha, WI), which is based on the Johnson-Wilson model²⁵ and is insensitive to the delay between arterial and tissue time-attenuation curve (TAC) to generate a map of permeability. For each patient, the arterial and venous regions of interest (ROIs) were automatically chosen by the software in one of the anterior cerebral arteries and the posterior superior sagittal sinus, respectively. The venous TAC was used as a reference to correct for the partial volume averaging of the arterial TAC²⁵. Tissue TACs were measured from 2 x 2 pixel blocks of the CT images. Parametric perfusion

maps of permeability (PS) were calculated by deconvolving the arterial TAC with each tissue TAC using the Johnson-Wilson model²⁵.

The diffusion tensor imaging (DTI) data were analyzed using Brainvoyager QX software (Brain Innovation, Maastricht, The Netherlands). From the DTI dataset six independent elements of the diffusion tensor were determined for each voxel, and the eigen values ($\lambda_1, \lambda_2, \lambda_3$) of the diffusion tensor were calculated. The eigen value information was used to calculate the following diffusion tensor parameters²⁶: mean diffusivity (MD), fractional anisotropy (FA), axial diffusivity (AxD) and radial diffusivity (RD) as shown in the following equations (1-4):

$$MD = \lambda_1 + \lambda_2 + \lambda_3 \quad [2.1]$$

$$FA = \sqrt{\frac{3}{2}} \sqrt{\frac{(\lambda_1 - \bar{\lambda})^2 + (\lambda_2 - \bar{\lambda})^2 + (\lambda_3 - \bar{\lambda})^2}{\lambda_1^2 + \lambda_2^2 + \lambda_3^2}} \quad [2.2]$$

$$AxD = \lambda_1 \quad [2.3]$$

$$RD = \frac{(\lambda_2 + \lambda_3)}{2} \quad [2.4]$$

The diffusion tensor maps of MD, FA, AxD, RD, the T2w images, the FLAIR images, and the permeability maps were all coregistered in 3D slicer²⁷.

Three regions of interest (ROIs) were selected for each patient. The ROIs were selected using the PS map and the coregistered FLAIR images simultaneously. ROI1 was defined within a high permeability region on the PS map and a high signal intensity region on FLAIR. ROI1 was labeled as a high permeability region attributed to tumor. ROI2 was

defined as a high signal intensity region on FLAIR with normal permeability on the PS map and attributed to radiation induced necrosis (RI). A region on the white matter on the contralateral side with normal signal intensity on FLAIR and normal permeability on the PS map was selected as ROI3, and labeled as normal tissue. For each patient, the three ROIs were used to extract the mean MD, FA, AxD, and RD values from the diffusion tensor maps and the mean T2-weighted and FLAIR signal intensities. The values in ROI1 (high permeability) and ROI2 (RI) were normalized by the values in the normal tissue on the contralateral side. These normalized values were used for statistical comparisons.

All statistical comparisons were performed with SPSS software version 21 (SPSS, IBM, Chicago, IL). Independent sample t-tests were conducted to determine if there were differences in the normalized DTI parameters, the T2w signal intensity (SI) and FLAIR signal intensity between the high permeability region and RI region. A Pearson product-moment correlation was computed to determine whether there was an association between the measured MRI parameters in both the high permeability (tumor) and low permeability (RI) regions.

2.3 Results

A typical FLAIR image (Figure 2.1A), T2W image (Figure 2.1B), CT perfusion map (Figure 2.1C), and blood flow map (Figure 2.1D) from a single subject were used to visualize the tumor and tissue with RI. The FLAIR image with the corresponding permeability map overlaid is shown in Figure 2.1E. Based on these images, regions of

interest in the high permeability area (green), the high intensity area (brown), and the normal area (yellow) on the contralateral side were defined (Figure 2.1F).

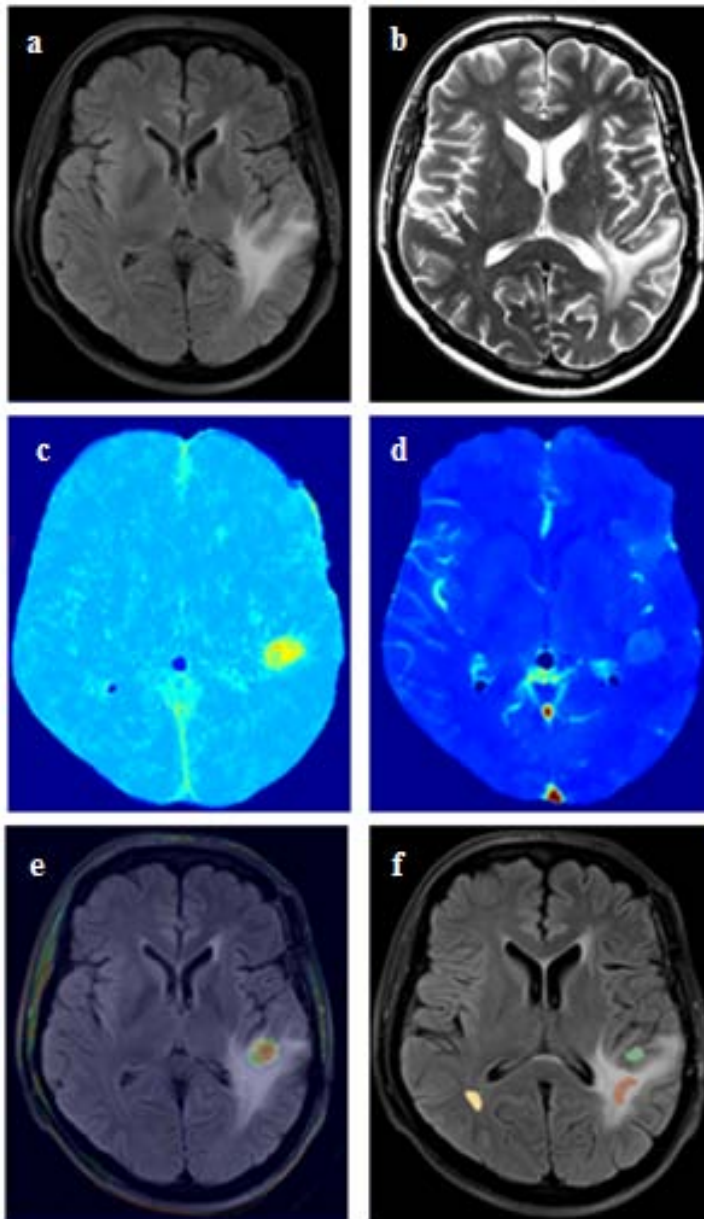


Figure 2.1a-f FLAIR, T2w images, PS and CBV maps, and the ROIs used for analysis.

Table 2.2 provides the mean and standard deviation (SD) of each measured parameter in the high permeability (tumor) and low permeability (RI) regions and the p-values. There were no significant differences in the T2w ($p = .94$) and FLAIR ($p = .99$) signal intensities between the high permeability region and the RI region. Also there were no significant differences in the diffusion tensor parameters FA ($p = .82$), MD ($p = .44$), AxD ($p = .33$) and RD ($p = .56$) comparing the high permeability region to the RI region.

Table 2.2 Parameters measured in the high permeability and RI regions.

Normalized Parameters	High Permeability Region (mean \pm SD)	RI Region (mean \pm SD)	p-value
FA	.73 \pm .29	.77 \pm .35	.82
MD	1.14 \pm .47	.97 \pm .36	.44
AxD	1.04 \pm .42	.87 \pm .24	.33
RD	1.23 \pm .54	1.07 \pm .50	.56
T2w SI	.96 \pm .33	.94 \pm .42	.94
FLAIR SI	.94 \pm .43	.94 \pm .36	.99

As expected, there was a strong positive correlation between MD and RD ($r = .98$, $p < .01$) in both the high permeability (tumor) region and in the low permeability (RI) region ($r = .98$, $p < .01$). The low permeability (RI) region also produced a strong negative correlation between FA and RD ($r = -.76$, $p < .05$) and a strong positive correlation between T2w signal intensity and FLAIR signal intensity ($r = .89$, $p < .01$). These associations are summarized in Figure 2.2.

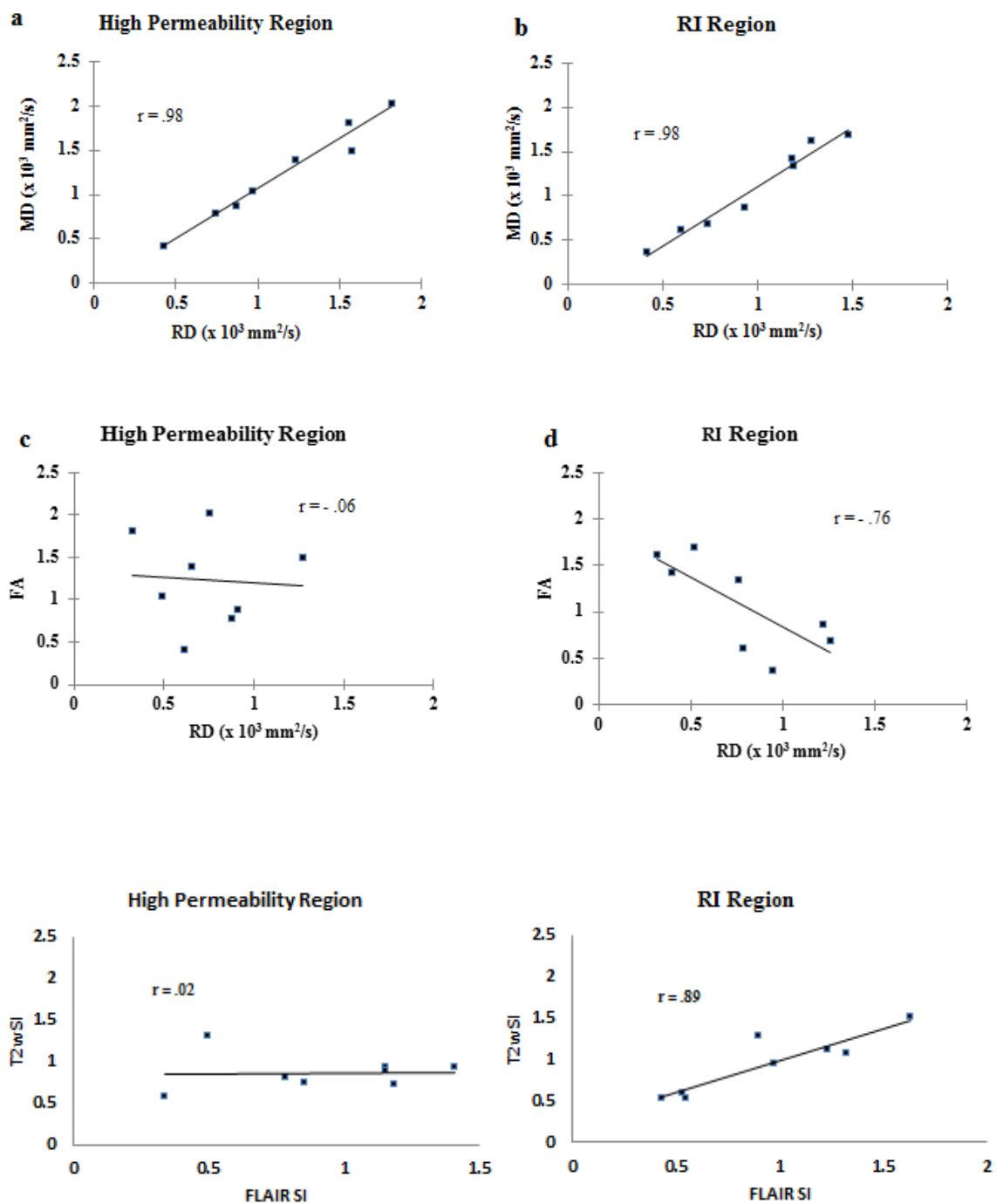


Figure 2.2a-f Scatterplots summarizing the correlation analysis.

2.4 Discussion

Differentiating radiation injury (RI) from recurrent or progressive tumor in patients with glioblastoma is essential since the prognoses and treatment for the two entities is different. Conventional morphologic imaging alone has failed to differentiate tumor regions from RI regions. With the advent of newer aggressive treatment options, RI is on the rise and the follow-up imaging of patients over time is becoming more complex. Diffusion MRI has shown promise in differentiating these two entities to a limited extent^{5, 13}. Various other imaging techniques also offer moderate success due to the complexity of the tissue microenvironment and the inherent limitations of these modalities and techniques.

The goal of this study was to determine whether morphological MRI and diffusion tensor imaging (DTI) could differentiate tumor recurrence from RI. The morphological parameters we explored were T2w SI and FLAIR SI, while the diffusion tensor parameters we explored were FA, MD, AxD, and RD. We did not find any statistically significant differences in the means of the measured parameters in the high permeability (tumor) region and the low permeability (RI) region.

There was a significant correlation between MD and RD in both the high permeability region and RI region. Such a correlation is expected because infiltrating tumor cells can cause an increase in MD and RD while edema from radiation damage can also cause a similar increase³¹. Therefore the correlation between MD and RD may not be a good marker to distinguish the two regions. Interestingly, a significant negative correlation was observed between FA and RD and a significant positive correlation was observed

between T2w SI and FLAIR SI in the low permeability (RI) region. A decrease in FA can be caused by vasogenic edema due to radiation injury^{13, 29}, which can in turn cause an increase in RD (the radial component of diffusion)³⁰. Therefore the presence of vasogenic edema could explain why FA has a significant negative correlation with RD in the RI region. These correlations were not observed in the high permeability (tumor) region. Therefore, the correlations between FA and RD, and between T2w SI and FLAIR SI may differentiate these two regions.

Further work is needed to determine whether these correlations could help differentiate high permeability regions from radiation injury. One possible approach would involve identifying suspicious regions and then correlating DTI parameter values and morphological MRI values on a pixel-by-pixel basis from within the ROI. If a significant correlation was found, it may indicate radiation injury. This success of this approach depends on the heterogeneity of the tissue within the ROI.

To date, no objective study on correlation analyses of diffusion tensor parameters has shown any diagnostic potential in patients with glioblastoma multiforme. Our study had several limitations. First, the patient population was small, and further investigation with a larger patient population is necessary to confirm these preliminary findings. Further large-scale studies would provide estimates of the accuracy and diagnostic utility of this new method. The second limitation of this study is the use of permeability maps to select possible tumor regions. There have been numerous studies that have successfully correlated perfusion properties of tumors with histology, and shown that progressive or recurrent tumors have high permeability compared to RI regions²⁰⁻²². Ideally in a future

study the tumor regions would be confirmed histologically, which is the current gold standard.

Perfusion CT is widely used for differentiating RI from tumor tissue but has several disadvantages that include additional cost, examination time, increased exposure to radiation, and increased post-processing and reading time. Obtaining similar information directly from MRI would circumvent these disadvantages. T2, FLAIR and DTI are part of routine clinical MRI protocols for brain tumor patients. The results of the present study suggest that correlations observed among routine MRI parameters may help differentiate RI from tumor.

In conclusion, our results indicate that the significant correlations of diffusion tensor imaging parameters FA and RD, along with the significant correlations of morphological MRI parameters of T2w SI and FLAIR SI, could be used to differentiate recurred tumor from RI regions in patients with GBM.

2.5 References

- [1] Yang I, Aghi MK. New advances that enable identification of glioblastoma recurrence. *Nature reviews in clinical oncology* 2009; 6:648-657.
- [2] Hygino da cruz jr. LC, Rodriguez I, Domingues RC, Gasparetto EL, Sorensen AG. Pseudoprogression and Pseudoresponse: Imaging Challenges in the Assessment of Posttreatment Glioma. *American Journal of neuroradiology* 2011; 32:1978-1985.
- [3] Chamberlain MC, Glantz MJ, Chalmers L, Van Horn A, Sloan AE. Early necrosis following concurrent Temodar and radiotherapy in patients with glioblastoma. *J Neurooncology* 2007; 82(1):81–83.
- [4] Gasparetto EL, Pawlak MA, Patel SH,. Posttreatment recurrence of malignant brain neoplasm: accuracy of relative cerebral blood volume fraction in discriminating low from high malignant histologic volume fraction. *Radiology* 2009;250(3):887–896.
- [5] Kashimura H, Inoue T, Beppu T, et al. Diffusion tensor imaging for differentiation of recurrent brain tumor and radiation necrosis after radiotherapy—three case reports. *Clinical neurology and neurosurgery* 2007; 109: 106-110.
- [6] Kumar AJ, Leeds NE, Fuller GN, et al. Malignant gliomas: MR imaging spectrum of radiation therapy- and chemotherapy-induced necrosis of the brain after treatment. *Radiology*. 2000; 217:377–384.
- [7] Mullins ME, Barest GD, Schaefer PW, et al. Radiation necrosis versus. glioma recurrence: Conventional MR imaging clues to diagnosis. *Am J Neuroradiol*. 2005; 26:1967–72.
- [8] Rogers LR, Scarpace L, Gutierrez J, et al. Magnetic resonance imaging characteristics and histological correlates of cerebral radiation necrosis. *Neurology*. 2006; 66(2):335.

- [9] Jain R, Scarpace L, Ellika S, et al. First-pass perfusion computed tomography: initial experience in differentiating recurrent brain tumors from radiation effects and radiation necrosis. *Neurosurgery* 2007; 61:778–786.
- [10] Jain R, Narang J, Schultz L, et al. Permeability estimates in histopathology proven treatment induced necrosis using perfusion CT: Can these add to other perfusion parameters in differentiating from recurrent/progressive tumors? *AJNR Am J Neuroradiol.* 2011; 32:658–663.
- [11] Sugahara T, Korogi Y, Tomiguchi S, et al. Post therapeutic intra axial brain tumor: the value of perfusion-sensitive contrast enhanced MR imaging for differentiating tumor recurrence from non-neoplastic contrast-enhancing tissue. *AJNR Am J Neuroradiol.* 2000;21:901–909.
- [12] Barajas RF, Chang JS, Sneed PK, et al. Distinguishing recurrent intra-axial metastatic tumor from radiation necrosis following gamma knife radiosurgery using dynamic susceptibility-weighted contrast-enhanced perfusion MR imaging. *AJNR Am J Neuroradiol.* 2009; 30:367–372.
- [13] Hein PA, Eskey CJ, Dunn JF, et al. Diffusion weighted imaging in the follow-up of treated high-grade gliomas: Tumor recurrence versus radiation injury. *Am J Neuroradiol.* 2004; 25:201–209.
- [14] Rock JP, Scarpace L, Hearshen D, et al. Associations among magnetic resonance spectroscopy, apparent diffusion coefficients, and image guided histopathology with special attention to radiation necrosis. *Neurosurgery.* 2004; 54:1111–17.
- [15] Graves EE, Nelson SJ, Vigneron DB, et al. Serial proton MR spectroscopic imaging of recurrent malignant gliomas after gamma knife radiosurgery. *Am J Neuroradiol.* 2001; 22:613–624.

- [16] Rabinov JD, Lee PL, Barker FG, et al. In vivo 3-T MR spectroscopy in the distinction of recurrent glioma versus radiation effects: Initial experience. *Radiology*. 2002; 225: 871–879.
- [17] Chao ST, Suh JH, Raja S, et al. The sensitivity and specificity of FDG PET in distinguishing recurrent brain tumor from radionecrosis in patients treated with stereotactic radiosurgery. *Int J Cancer*. 2001; 96:191–197.
- [18] Tsuyuguchi N, Sunada I, Iwai Y, et al. Methionine positron emission tomography of recurrent metastatic brain tumor and radiation necrosis after stereotactic radiosurgery: is a differential diagnosis possible? *J Neurosurg*. 2003; 98:1056–1064.
- [19] Narang J, Jain R, Arbab AS, Mikkelsen T, Scarpace L, Rosenblum ML, Hearshen D, Babajani-Feremi A. Differentiating treatment-induced necrosis from recurrent/progressive brain tumor using nonmodel-based semiquantitative indices derived from dynamic contrast-enhanced T1-weighted MR perfusion. *Neuro-oncology* 2011; 13(9):1037-1046.
- [20] Jain R, Narang J, Schultz L, Scarpace L, Saksena S, Brown S, Rock JP, Rosenblum M, Gutierrez J, Mikkelsen T. Permeability Estimates in Histopathology-Proved Treatment-Induced Necrosis Using Perfusion CT: Can These Add to Other Perfusion Parameters in Differentiating from Recurrent/Progressive Tumors? *American Journal of neuroradiology* 2011; 32:658-663.
- [21] Jain R, Ellika SK, Scarpace L, et al. Quantitative estimation of permeability surface-area product in astroglial brain tumors using perfusion CT and correlation with histopathologic grade. *AJNR Am J Neuroradiol* 2008;29:694–700
- [22] Jain R, Gutierrez J, Narang J, et al. In vivo correlation of tumor blood volume and permeability with histological and molecular angiogenic markers in gliomas. *AJNR Am J Neuroradiol* 2011;32:388–94

- [23] Tsuruda JS, Kortman K, Bradley WG, Wheeler DC, Dalsem. WV, Bradley TP. Radiation Radiation effects on cerebral white matter: MR Evaluation. AJNR. 1987; 165-171.
- [24] Pruzincova L, Steno J, Srbecky, Kalina P, Rychly B, Boljesikova E, Chorvath, Novotny M, Procka, Makaiova I, Belan V. MR imaging of late radiation therapy- and chemotherapy-induced injury: a pictorial essay. European Society of Radiology. 19:2716-2727. 2009
- [25] Lee TY, Purdie TG, Stewart E. CT imaging of angiogenesis. Q J Nucl Med 2003; 47:171–187.
- [26] Serena J. Counsell, Yuji Shen, James P. Boardman, David J. Larkman, Olga Kapellou, Philip Ward, Joanna M. Allsop, Frances M. Cowan, Joseph V. Hajnal, A. David, Edwards and Mary A. Rutherford. Axial and Radial Diffusivity in Preterm Infants Who Have Diffuse White Matter Changes on Magnetic Resonance Imaging at Term-Equivalent Age, 2006; 117(2):376-386.
- [27] Fedorov A., Beichel R., Kalpathy-Cramer J., Finet J., Fillion-Robin J-C., Pujol S., Bauer C., Jennings D., Fennessy F., Sonka M., Buatti J., Aylward S.R., Miller J.V., Pieper S., Kikinis R. 3D Slicer as an Image Computing Platform for the Quantitative Imaging Network. Magnetic Resonance Imaging 2012; 30(9): 1323-41
- [28] Wang W, Steward CE, Desmond PM. Diffusion Tensor Imaging in Glioblastoma Multiforme and Brain Metastases: The Role of p , q , L , and Fractional Anisotropy. American Journal of Neuroradiology 2009; 30:203-08.
- [29] Chiaki Asao, Yukunori Korogi, Mika Kitajima, Toshinori Hirai, Yuji Baba, Keishi Makino, Masato Kochi, Shoji Morishita, and Yasuyuki Yamashita. Diffusion-Weighted Imaging of Radiation- Induced Brain Injury for Differentiation from Tumor Recurrence. AJNR 2005; 26:1455-1460.

- [30] Y. Wang¹, S-K. Song. The Effect of Inflammation on DTI Derived Axial and Radial Diffusivity: A Monte Carlo Simulation Study. *Proc. Intl. Soc. Mag. Reson. Med.* 19 (2011)

3 Differentiating between glioblastoma and metastasis using first- and second-order MR image texture

3.1 Introduction

Glioblastoma multiforme (GBM) and metastasis (MET) are the two most common types of brain tumors in adults¹. These tumors can have similar appearance on magnetic resonance imaging (MRI) specifically a necrotic mass surrounded by ring-like enhancement and extensive edema²⁻⁴. Discriminating between these two types of tumor remains challenging when the patient presents with a solitary enhancing mass, since both types of tumors exhibit similar radiologic appearance⁴. Differentiating between GBM and MET is very important because they have different biological mechanisms and require different treatment strategies^{5, 6}. Histopathologic analysis of a biopsy sample from the tumor region is the only currently accepted method to make a definitive diagnosis^{7, 8}. The use of noninvasive methods is preferable and sometimes mandatory when a biopsy is not possible because of the general condition of the patient or if the mass is located near a critical area. Therefore, it would be clinically beneficial to have a noninvasive method of differentiating between these tumor types without the need for biopsy⁹. Since routine MRI is not very useful for non-invasively differentiating between these two types of tumor, many studies have focused on advanced imaging modalities, such as diffusion tensor imaging¹⁰⁻¹³, perfusion MRI^{14,15}, MR spectroscopy¹⁶⁻¹⁹ and perfusion CT²⁰⁻²³. The advanced imaging modalities that have been used require longer scan times, expertise in advanced imaging, and additional imaging modality like CT which increases cost,

examination time, and patient exposure to radiation. Since MRI is part of the routine brain tumor imaging, a technique based on routine MRI that would provide quantitative information without the additional cost would be highly advantageous.

Image texture analysis has been used in a range of studies for classifying tissues²⁴⁻²⁶ in breast and brain tumors. Image texture is a function of the spatial variation of pixel intensities in an image²⁷. Texture analysis can provide quantitative information that is not visible to human vision²⁸. The most common technique to compute image texture is to use statistical based methods, namely first- and second-order textures, which analyze properties of individual pixel intensities and their spatial distribution within the image.

The purpose of the current study was to determine whether first- and second- order image texture properties of GBM and MET could be used to differentiate between these two types of tumor. We hypothesized that the texture properties of GBM and MET tumor tissue on post-contrast T1-weighted (T1w) MRI are different, and therefore these texture properties could be used to differentiate GBM from MET. This study compares four first-order texture features: the mean signal intensity, standard deviation of the signal intensity, skewness, and kurtosis; and five second-order texture features: entropy, homogeneity, inertia, correlation, and energy of GBM and MET tumors.

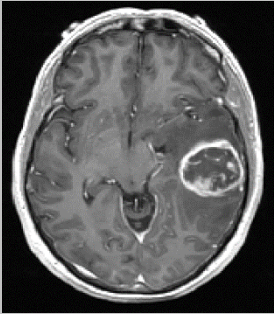
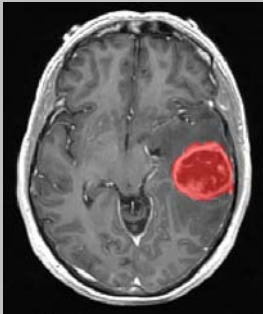
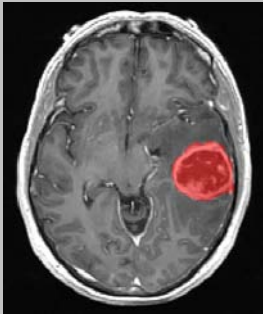

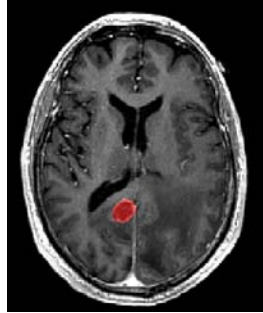
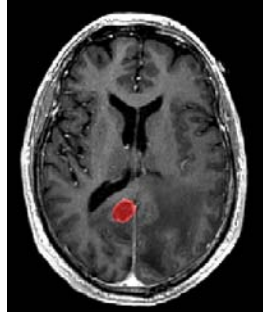
3.2 Methods

Thirty-Nine (39) patients with a diagnosis of brain metastasis and 31 patients with a diagnosis of glioblastoma multiforme were evaluated retrospectively for this study. All patients had undergone routine brain MR examination before radiation treatment and/or surgical resection at London Health Sciences Center, Canada. The tumors that were resected fulfilled the 2007 WHO histopathologic criteria for diagnosis¹.

MR imaging was performed on a 1.5T GE Signa MRI system (GE Healthcare, Milwaukee, Wisconsin). The MR imaging protocol included pre- and post-contrast T1w sequences. Post-contrast images were acquired immediately after contrast injection. A 3D spoiled gradient echo sequence was used to acquire the T1w images with the following parameters: repetition time: 8.84 msec, echo time: 3.47 msec, slice thickness: 2 mm, matrix size: 512×512 , flip angle: 13° .

3D lesion contouring on the post-contrast T1w MR images was performed under the supervision of a radiation oncologist with expertise in the treatment of brain tumors using ITK-SNAP (Version 2.4.0)²⁹. The contours were saved as 3D label maps. Figure 3.1 shows the post-contrast T1w images of GBM and MET lesions, with the contours overlaid on the images.

Figure 3.1 Post-contrast T1w image of GBM and MET lesion, with the contour overlaid.

Type of tumor	Post-contrast image	T1w	Contour overlaid
GBM			
MET			

3.2.1 Data Analysis

All calculations were performed using Matlab 7.1. (The Mathworks Inc., Natick, MA, USA). For each lesion, we calculated the following first- and second-order texture features: (1) mean T1w signal intensity, (2) standard deviation of the T1w signal intensity, (3) skewness, (4) kurtosis, (5) information entropy of the T1w signal intensity histogram, (6) homogeneity, (7) inertia, (8) energy, and (9) correlation. Features (1) through (4) are first-order texture measures that are estimated from individual pixel

values in the tumor region. Features (5) through (9) are second-order texture features that were calculated based on a gray-level co-occurrence matrix (GLCM)^{30, 31, 32}.

The GLCM approach is based on the use of second-order statistics of the grayscale image histograms and is an estimate of the second-order joint probability $G(i, j)$ of the intensity values of two pixels (i and j), at a certain pixel distance apart along a given direction (i.e., the probability that i and j have the same intensity). This joint probability takes the form of a square matrix with row and column dimensions equal to the number of discrete gray levels (intensities) in the image. If an intensity image contained no texture the resulting GLCM would be completely diagonal. As the image texture increases (i.e. as the local pixel intensity variations increase), the off-diagonal values in the GLCM become larger.

The images were quantized to thirty-two gray levels, and four 32×32 GLCMs were computed with neighboring pixels defined in angular directions of 0, 45, 90 and 135. The resulting texture features were averaged over the four directions. Each GLCM-based second-order texture feature was calculated as follows:

Table 3.1 GLCM-based second-order texture features

Feature	Equation	Description
Entropy	$-\sum_{i,j} G(i,j) \log_2 G(i,j)$	Measures the randomness of the GLCM.
Homogeneity	$\sum_{i,j} \frac{1}{1 + i - j } G(i,j)$	Measures the closeness of the distribution of elements in the GLCM to the GLCM diagonal.
Inertia	$\sum_{i,j} (i - j)^2 G(i,j)$	Measures the intensity contrast between a pixel and its neighbor over the whole image. Describes the local variations in the GLCM.
Correlation	$\sum_{i,j} \frac{(i - \mu)(j - \mu)G(i,j)}{\sigma^2}$	Measures how correlated a pixel is to its neighbor over the whole image. Describes the joint probability occurrence of the specified pixel pairs.
Energy	$\sum_{i,j} G(i,j)^2$	Measures sum of the squared elements of the GLCM. It describes the uniformity of the image.

3.2.2 Statistical Analysis

All statistical analysis was performed using SPSS software (IBM SPSS, Version 21, Chicago, IL). Kolmogorov-Smirnov test was used to assess the normality of the data. Mann-Whitney U test was conducted to test the differences between the two groups (GBM and MET). $P < .05$ was considered to indicate a statistically significant difference.

The efficacy of the texture features for classification was evaluated using logistic regression analysis. The first- and second-order texture features were combined into a

multivariate logistic regression analysis to determine the most significant parameters and to build an optimal logistic regression model (LRM) to classify GBM and MET. Model fit was evaluated by means of the Hosmer–Lemeshow goodness-of fit test³³.

Areas under the receiver operating characteristic (ROC) curves were computed for each of the first- and second-order texture features. ROC curves were also computed for the predictive features that were calculated from the LRM. ROC curve analyses were performed to determine optimum threshold and the diagnostic accuracy of each histogram parameter for discriminating the two types of tumors. These analyses allowed us to determine the sensitivity, specificity, 95 % confidence interval (CI), standard error (SE), and area under the curve (AUC) associated with each individual texture parameter and combined texture parameter as a function of the threshold value used to discriminate the two types of tumors.

3.3 Results

The independent samples Mann-Whitney U test for the first-order texture features showed significant differences in the standard deviation of the T1w signal intensity for the GBM and MET groups. No differences were found in T1w signal intensity, skewness and kurtosis between the GBM and MET groups. Table 3.2 shows the mean and standard deviation (SD) of each first-order texture feature for the GBM and MET, as well as the result of the Mann-Whitney U test for each feature. Figure 3.2 summarizes the results in form of bar graphs for each of the first-order texture feature.

Table 3.2 Mean and SD of each of the first-order texture feature.

First-Order Texture	GBM	MET	p-value
Feature	(mean \pm SD)	(mean \pm SD)	
T1w Signal Intensity	1382 \pm 660.62	1194 \pm 808.27	.08
SD T1w Signal Intensity	438 \pm 258.21	312 \pm 235.29	.02
Skewness	.159 \pm .39	.079 \pm .50	.52
Kurtosis	2.85 \pm .74	2.97 \pm .63	.22

The independent samples Mann-Whitney U test for the second-order texture features showed significant differences in the entropy, homogeneity, inertia and energy feature for the GBM and MET groups. No differences were found in the correlation feature for the GBM and MET groups. Table 3.3 shows the mean and standard deviation of each second-order texture feature for the GBM and MET, as well as the result of the Mann-Whitney U test for each feature. Figure 3.3 summarizes the results in form of bar graphs for each of the second-order texture feature.

Table 3.3 Mean and SD of each of the second-order texture feature.

Second-Order Texture Feature	GBM (mean \pm SD)	MET (mean \pm SD)	p-value
Entropy	10.18 \pm 1.11	9.32 \pm 1.46	.007
Homogeneity	.995 \pm .003	.998 \pm .001	.000
Inertia	.320 \pm .183	.155 \pm .092	.000
Correlation	.915 \pm .047	.914 \pm .065	.615
Energy	.981 \pm .013	.992 \pm .005	.000

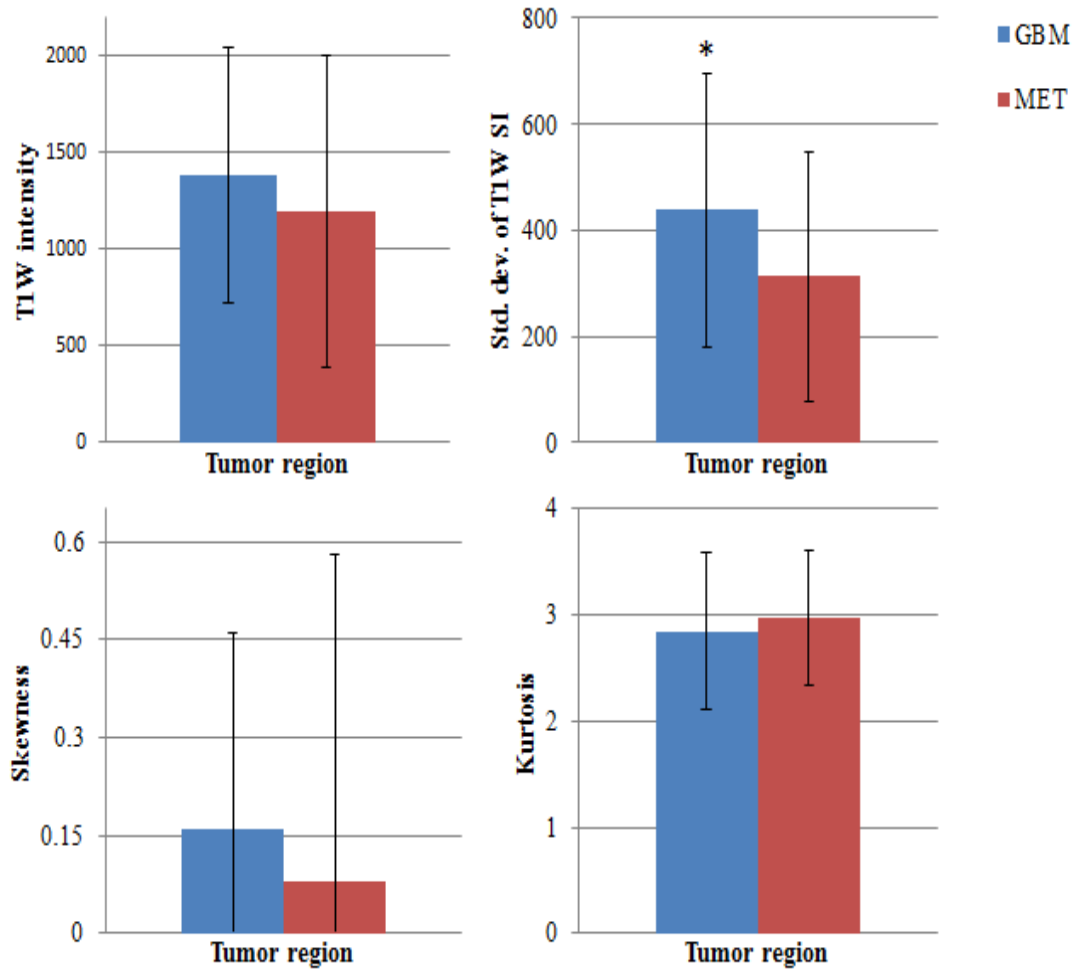


Figure 3.2 Plots of the first-order texture features for GBM and MET. Standard deviation of the T1w signal intensity was the only significantly different feature between the two tumor types.

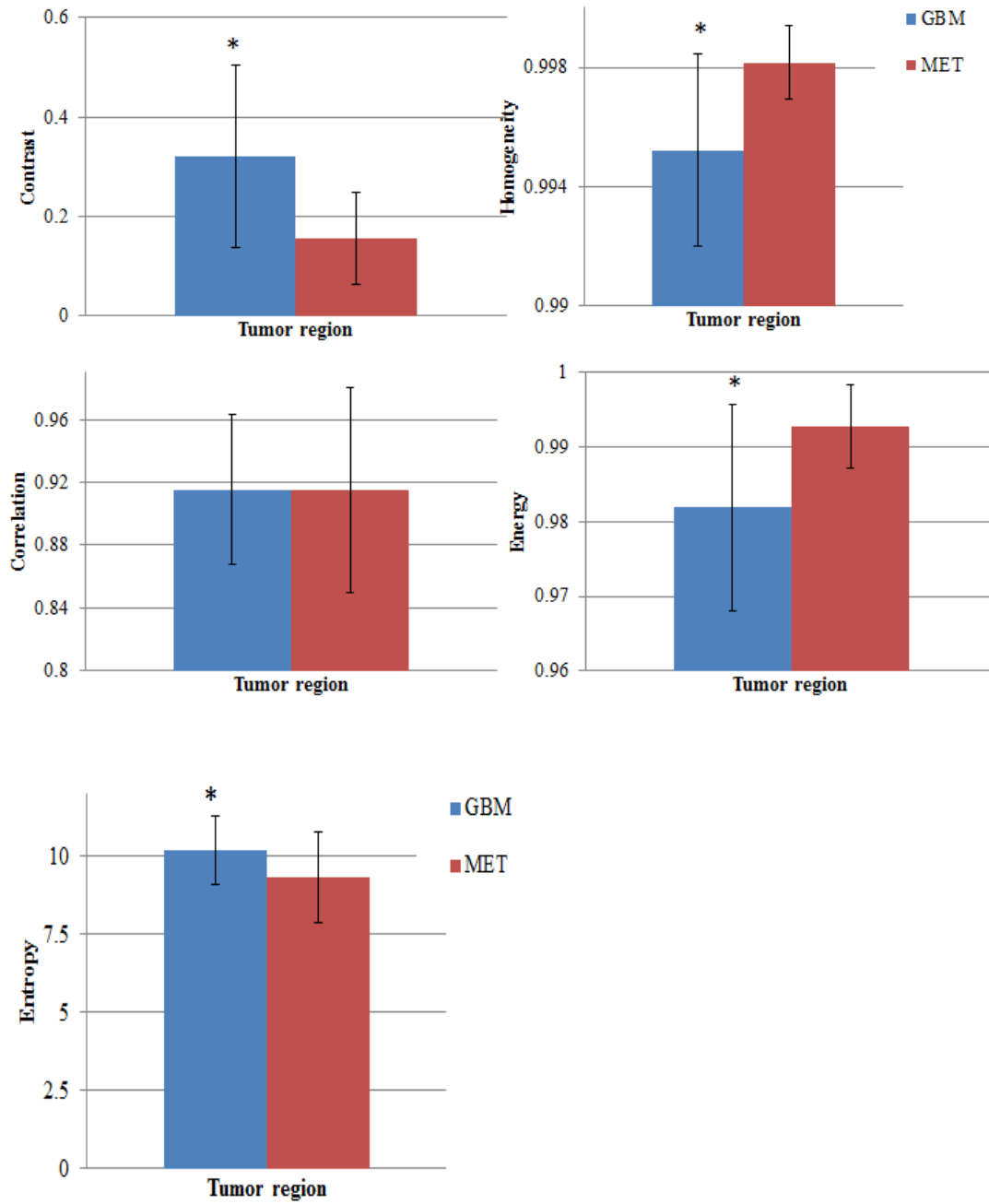


Figure 3.3 Plots of the second-order texture features for GBM and MET. Contrast, homogeneity, energy and entropy features were significantly different between the tumor types.

3.3.1 ROC curve analysis:

Each texture feature was evaluated for its discriminative ability using ROC analysis as shown in Table 3.4 and Figure 3.4, 3.5 and 3.6. When used alone, second-order texture feature of inertia (AUC= .790) was the best feature for discrimination, followed by homogeneity (AUC= .776), energy (AUC= .752) and entropy (AUC= .688). The first-order texture features of mean of the T1w signal intensity (AUC= .621), standard deviation of the T1w signal intensity (AUC= .659), skewness (AUC= .544) and kurtosis (AUC= .585) were not very useful in discriminating the tumor types.

The LRM of the combined first- and second-order texture features was the most accurate in differentiating the tumor types with AUC= 0.885, sensitivity = 90.3%, specificity = 82.1 % and cutoff value = 0.673. The LRM of the second-order texture features also showed good accuracy differentiating the tumor types with AUC= 0.840, sensitivity = 83.9 %, specificity = 66.7 % and cutoff value = 0.708 compared to the individual second-order textures. The LRM of the first-order texture features was a poor discriminator of the tumor types with AUC= 0.658, sensitivity = 61.3%, specificity = 64.1 % and cutoff value = 0.562. The optimum threshold, sensitivity, and specificity of each texture parameter and combined texture parameters to distinguish the two tumor types are summarized in Table 3.4

Table 3.4 ROC curve analysis for each of the first- and second-order texture features and combination of the first- and second-order texture features for differentiation between GBM and MET. (the cut-off value was chosen as a point on the ROC curve that maximizes sensitivity + specificity)

Texture Feature	Cut-off Value	Sensitivity	Specificity	AUC	SE	CI
Mean T1w	1073	61.3	56.4	.621	.067	(.49, .75)
Std T1w	305	67.7	64.1	.659	.065	(.53, .78)
Skewness	.054	58.1	48.7	.544	.069	(.40, .68)
Kurtosis	2.91	64.5	56.4	.585	.070	(.44, .72)
Entropy	9.74	71.0	64.1	.688	.064	(.56, .81)
Homogeneity	.998	74.2	71.8	.776	.062	(.65, .89)
Inertia	.180	71.0	71.8	.790	.054	(.68,.89)
Correlation	.929	64.5	53.8	.535	.072	(.39, .67)
Energy	.992	74.2	66.7	.752	.063	(.62, .87)
First order	.562	61.3	64.1	.658	.067	(.52, .79)
Second order	.708	83.9	66.7	.840	.047	(.74, .93)
First + Second order	.673	90.3	82.1	.885	.043	(.80, .97)

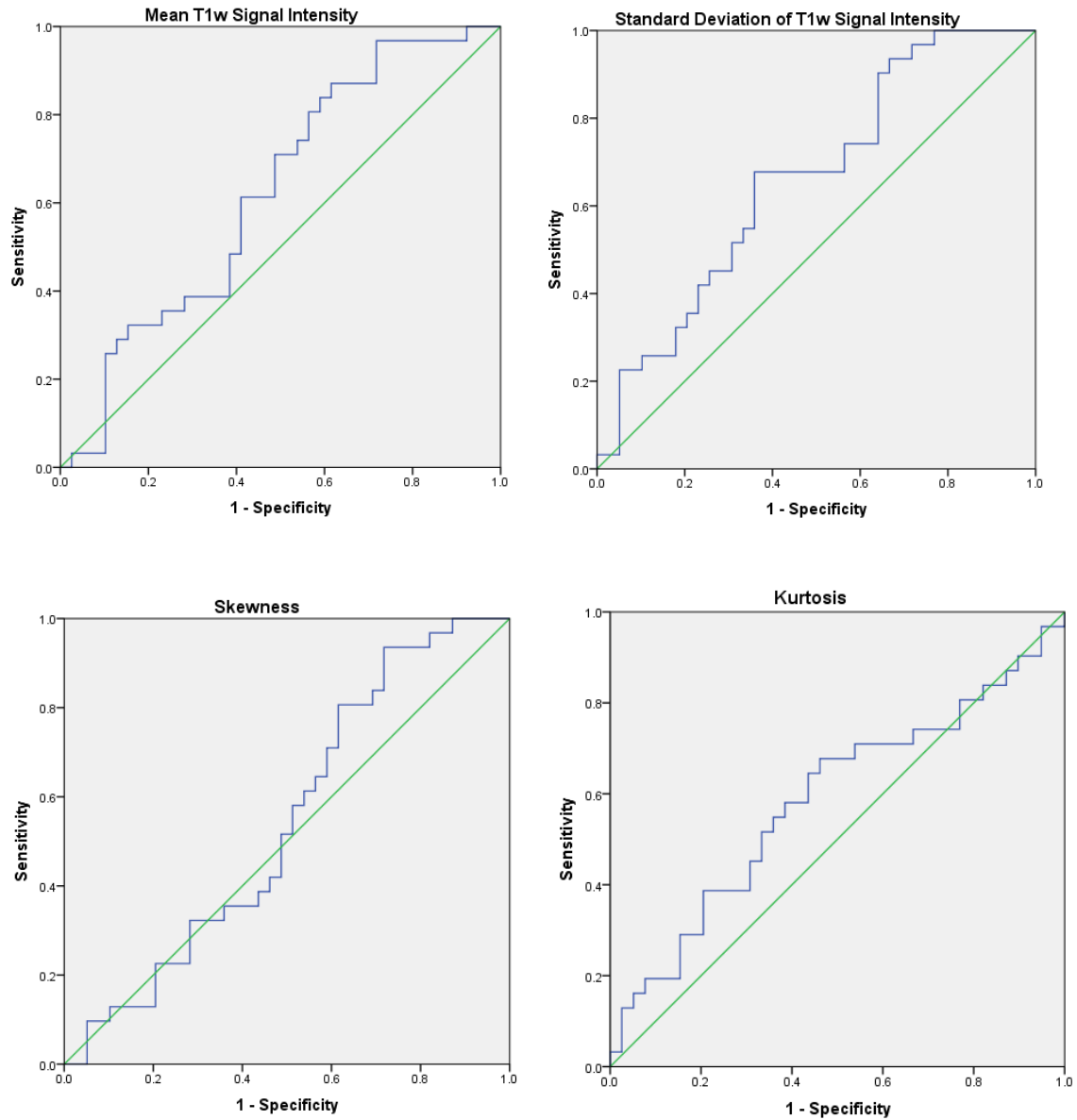


Figure 3.4 ROC curves for each of the first-order texture measures: mean T1w signal intensity (AUC= .621), standard deviation (std) of the T1w signal intensity (AUC= .659), skewness (AUC= .544) and kurtosis (AUC= .585). All four features have poor predictive value.

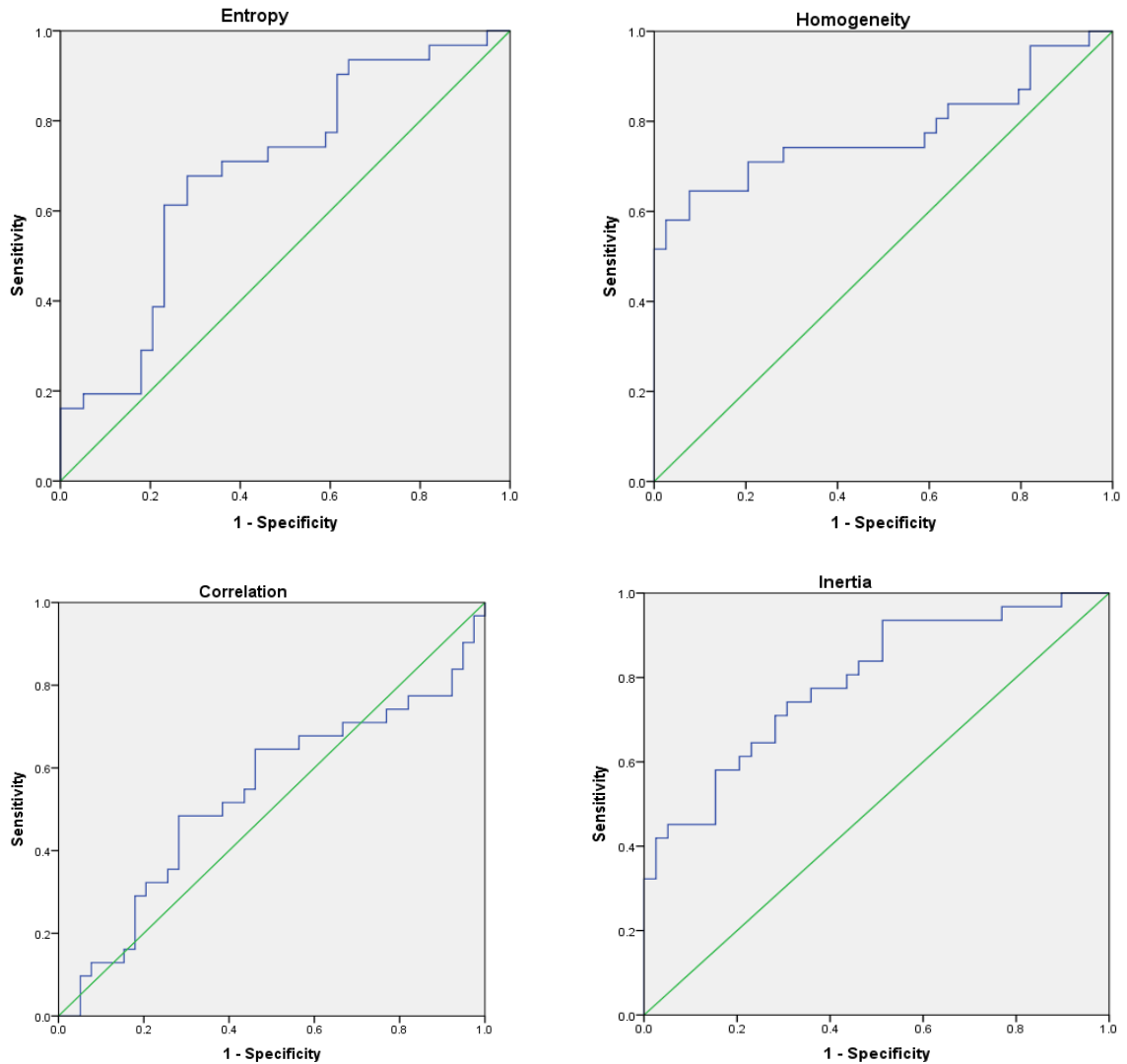


Figure 3.5 ROC curves for the second-order texture measures: entropy (AUC = .688), inertia (AUC= .790), homogeneity (AUC= .776), correlation (AUC= .535), and energy (AUC= .752). Inertia, homogeneity and energy (next page) are the best predictors for differentiating between GBM and MET when used alone.

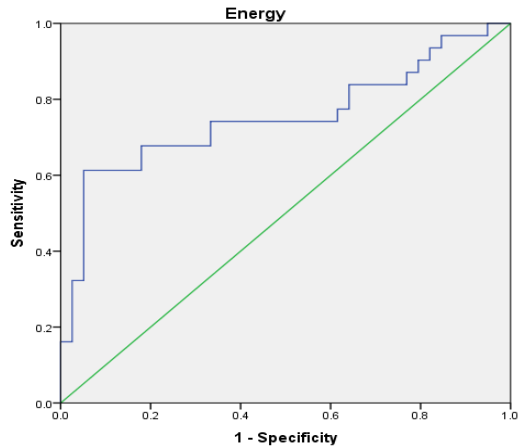


Figure 3.5 (contd): ROC curve for the second-order texture measure of energy.

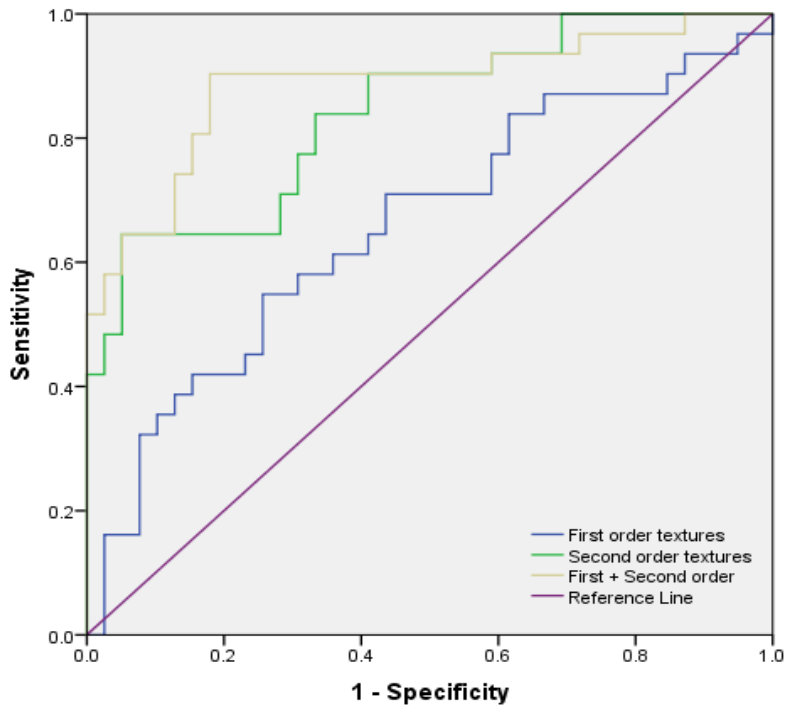
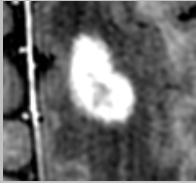
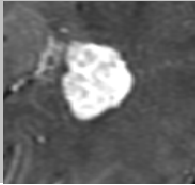


Figure 3.6 ROC curves for the first order textures (AUC = .658), second-order textures (AUC = .840) and combined first + second-order texture measures (AUC = .885). Combining the first and second order textures may provide the best predictive accuracy for differentiating between GBM and MET.

3.4 Discussion

GBM and MET typically demonstrate similar appearances on routine MR imaging. Since they have same clinical symptoms but different treatment strategies, a technique is needed to differentiate between these two types of tumors. In this study we investigated the feasibility of using texture-based analysis of routine MR images to differentiate GBM from MET. Texture analysis provides quantitative information about the spatial variation of pixel intensities in an image.

We investigated four first-order texture features (mean T1w signal intensity, standard deviation of the T1w signal intensity, skewness, and kurtosis) and five second-order texture features (entropy, homogeneity, inertia, correlation, and energy). First-order texture features are computed from gray level histogram while second order texture features are computed from the gray level co-occurrence matrix (GLCM) which analyzes gray level distribution of pairs of pixels. Figure 3.8a and 3.8b show sample GBM and MET images having similar radiologic appearance, where the second-order texture features of inertia, energy, and homogeneity are able to successfully differentiate between GBM and MET.

a	GBM	MET
Image		
Inertia	7.475	5.594
Energy	0.0050	0.0133
Homogeneity	0.4468	0.5336

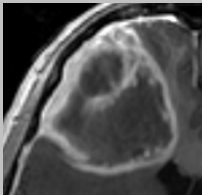
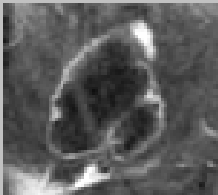
b	GBM	MET
Image		
Inertia	9.248	3.114
Energy	0.0136	0.0186
Homogeneity	0.4987	0.6063

Figure 3.4a,b GBM and MET tumors showing similar appearance on routine MR image but differences in the second-order texture measures.

A statistically significant difference was observed in the standard deviation of the mean T1w signal intensity. The first-order texture features of mean, skewness, and kurtosis did not show any significant differences between the two types of tumors. A statistically significant difference was observed in the second-order texture features of entropy,

inertia, homogeneity, and energy. No statistically significant difference was seen in the second-order texture feature of correlation.

ROC analysis showed that the combination of first- and second-order texture features had the largest AUC (0.88) and would have the best predictive accuracy for differential diagnosis between GBM and MET, followed by the combined second-order texture features (AUC= 0.84). The individual second-order texture features of inertia (AUC= .79), homogeneity (AUC= .77), and energy (AUC= .75) also showed good predictive accuracy. The combined first-order texture features (AUC= .65) was not very useful in differentiating the tumor types.

Other investigators have used advanced imaging techniques including diffusion and perfusion to differentiate between the two types of tumor¹⁰⁻¹⁵. Previous studies have also used a region of interest (ROI) approach within the whole tumor to derive imaging parameters for differentiation. However, this may not be the suitable approach since a small ROI in a large tumor may not provide information about the changes occurring within the tumor and may not be a good indicator of the global change within the entire tumor. Our technique is unique in several ways: (1) This is the first study to apply first- and second-order texture analysis for differentiating between GBM and MET tumors, (2) we use the routine clinical MR images instead of advanced imaging modalities to discriminate between the two tumor types, which saves time and cost; (3) we use a whole-tumor approach rather than small ROIs drawn inside the tumors. Our approach yields information about the textural properties of the whole tumor rather than a small ROI within the tumor: and (4) the simplicity of implementation makes it desirable than

other techniques. Simple mathematical calculations are used to compute the texture parameters.

A limitation of this study is the small sample size. Features that may have less effect on the differentiation may have been missed. Features which were approaching significance, such as the mean of the T1w signal intensity ($p = .08$), may become statistically significant with a larger sample size. Even within our sample size we had significant effects that were useful, suggesting that the texture features we found to be significant are important in differentiating GBM from MET. Another limitation is that the performance of the LRM is unclear without the use of a separate validation set, and further evaluation of the models need to be explored in future work on a larger data set.

3.5 Conclusions

We have demonstrated the ability of texture-based analysis of routine MR images to differentiate between GBM and MET. Our results indicate that the combination of first- and second-order texture features provides us with the highest predictive accuracy followed by the combined second-order features. When used individually, the second order texture feature of inertia had the best predictive accuracy followed by homogeneity and energy. Given the simplicity of our technique and availability of the post-contrast T1w MR images which are part of the routine brain tumor imaging, we believe this method may have practical significance and may become a useful tool for differentiating between GBM and MET.

3.6 References

- [1] Louis, D.N., Ohgaki, H., Wiestler, O.D., Cavenee, W.K., Burger, P.C., Jouvet, A., Scheithauer, B.W., Kleihues, P. The 2007 WHO classification of tumours of the central nervous system. *Acta Neuropathol.* 2007; 114:97–109.
- [2] Schwartz KM, Erickson BJ, Lucchinetti C. Pattern of T2 hypointensity associated with ring-enhancing brain lesions can help to differentiate pathology. *Neuroradiology* 2006;48:143–49
- [3] Byrnes TJ, Barrick TR, Bell BA, et al. Diffusion tensor imaging discriminates between glioblastoma and cerebral metastases in vivo. *NMR Biomed* 2011;24: 54–60
- [4] Schiff, D. Single Brain Metastasis. *Curr. Treat. Options Neurol.* 2001; 3(1):89–99.
- [5] Giese A, Bjerkvig R, Berens ME, et al. Cost of migration: invasion of malignant gliomas and implications for treatment. *J Clin Oncol* 2003;21:1624–36
- [6] Campos S, Davey P, Hird A, et al. Brain metastasis from an unknown primary, or primary brain tumour? A diagnostic dilemma. *Curr Oncol* 2009;16:62–66
- [7] Davis FG, McCarthy BJ, Berger MS. Centralized databases available for describing primary brain tumor incidence, survival, and treatment: Central Brain Tumor Registry of the United States; Surveillance, Epidemiology, and End Results; and National Cancer Data Base. *Neuro-oncol* 1999;1:205–11
- [8] Surawicz TS, McCarthy BJ, Kupelian V, et al. Descriptive epidemiology of primary brain and CNS tumors: results from the Central Brain Tumor Registry of the United States, 1990–1994. *Neuro-oncol* 1999;1:14–25
- [9] Blanchet L, Krooshof PW, Postma GJ, Idema AJ, Gorai B, Heerschap A, Buydens LM. Discrimination between metastasis and glioblastoma based on morphometric analysis of MR images. *AJNR* 2011; 32(1):67-73.

- [10] Byrnes TJ, Barrick TR, Bell BA, et al. Diffusion tensor imaging discriminates between glioblastoma and cerebral metastases in vivo. *NMR Biomed* 2011;24: 54–60
- [11] Tsuchiya K, Fujikawa A, Nakajima M, et al. Differentiation between solitary brain metastasis and high-grade glioma by diffusion tensor imaging. *Br J Radiol* 2005;78:533–37
- [12] Toh CH, Wei KC, Ng SH, et al. Differentiation of brain abscesses from necrotic glioblastomas and cystic metastatic brain tumors with diffusion tensor imaging. *AJNR Am J Neuroradiol* 2011;32:1646–51
- [13] Wang S, Kim S, Chawla S, et al. Differentiation between glioblastomas, solitary brain metastases, and primary cerebral lymphomas using diffusion tensor and dynamic susceptibility contrast-enhanced MR imaging. *AJNR Am J Neuroradiol* 2011;32: 507–14
- [14] Lehmann P, Saliou G, de Marco G, et al. Cerebral peritumoral oedema study: does a single dynamic MR sequence assessing perfusion and permeability can help to differentiate glioblastoma from metastasis? *Eur J Radiol* 2012;81: 522–27
- [15] Young GS, Setayesh K. Spin-echo echo-planar perfusion MR imaging in the differential diagnosis of solitary enhancing brain lesions: distinguishing solitary metastases from primary glioma. *AJNR Am J Neuroradiol* 2009;30:575–77
- [16] Opstad KS, Murphy MM, Wilkins PR, et al. Differentiation of metastases from high-grade gliomas using short echo time ¹H spectroscopy. *J Magn Reson Imaging* 2004;20:187–92
- [17] Fan G, Sun B, Wu Z, Guo Q, Guo Y. In vivo single-voxel proton MR spectroscopy in the differentiation of high-grade gliomas and solitary metastases. *Clinical Radiology* 2004; 59(1):77-85.

- [18] Law M, Cha S, Knopp EA, Johnson G, Arnett J, Litt AW High-grade gliomas and solitary metastases: differentiation by using perfusion and proton spectroscopic MR imaging 2002; 222(3):715-21.
- [19] Ishimaru H, Morikawa M, Iwanaga S, Kaminogo M, Ochi M, Hayashi K. Differentiation between high-grade glioma and metastatic brain tumor using single-voxel proton MR spectroscopy. *Eur Radiol* 2001;11:1784–91.
- [20] Cha S, Lupo JM, Chen MH, et al. Differentiation of glioblastoma multiforme and single brain metastasis by peak height and percentage of signal intensity recovery derived from dynamic susceptibility-weighted contrast-enhanced perfusion MR imaging. *AJNR Am J Neuroradiol* 2007; 28:1078–84
- [21] Blasel S, Jurcoane A, Franz K, et al. Elevated peritumoural rCBV values as a mean to differentiate metastases from high-grade gliomas. *Acta Neurochir* 2010;152:1893–99
- [22] Server A, Orheim TE, Graff BA, et al. Diagnostic examination performance by using microvascular leakage, cerebral blood volume, and blood flow derived from 3-T dynamic susceptibility-weighted contrast-enhanced perfusion MR imaging in the differentiation of glioblastoma multiforme and brain metastasis. *Neuroradiology* 2011;53:319–30
- [23] Ma JH, Kim HS, Rim NJ, et al. Differentiation among glioblastoma multiforme, solitary metastatic tumor, and lymphoma using whole-tumor histogram analysis of the normalized cerebral blood volume in enhancing and perienhancing lesions. *AJNR Am J Neuroradiol* 2010;31:1699–706
- [24] Evangelia I. Zacharaki; Sumei Wang; Sanjeev Chawla; Dong Soo Yoo; Ronald Wolf; Elias R. Melhem; Christos Davatzikos Classification of brain tumor type and grade using MRI texture and shape in a machine learning scheme. *Magnetic Resonance in Medicine* 2009; 62 (6):1609-1618.

- [25] Kulkarni DA, Bhagyashree SM, Udupi GR. Texture Analysis of mammographic images. *International journal of computer applications* 2010; 5(6).
- [26] S. Herlidou-Meme, J.M. Constans, B. Carsin, D. Olivie, P.A. Eliat, L. Nadal Desbarats, C. Gondry, E. Le Rumeur, I. Idy-Peretti, J.D. de Certaines. MRI texture analysis on texture test objects, normal brain and intracranial tumors. *Magnetic Resonance Imaging* 2003; 21:989–993
- [27] C.H Chen, L.F. Pau, P.S.P. Wang. *The handbook of pattern recognition and computer vision* (2nd edition), world scientific publishing. Pg-207-248, 1998.
- [28] Herlidou S, Rolland Y, Bansard JV, Rumeur EL, and Certaines JD. Comparison of automated and visual texture analysis in mri: characterization of normal and diseased skeletal muscle *Magnetic Resonance Imaging* 1999; 17(9):1393–1397.
- [29] Yushkevich PA, Piven J, Hazlett HC, Smith RG, Ho S, Gee JC, Gerig G. User guided 3D active contour segmentation of anatomical structures: Significantly improved efficiency and reliability. *Neuroimage* 2006; 31:1116-28.
- [30] Connors RW, Harlow CA. A theoretical comparison of texture algorithm. *IEEE Transactions in Pattern Analysis and Machine Learning* 1980; 2(3):204–22.
- [31] R.M. Haralick, K. Shanmugam, I. Dinstein, Textural features for image classification *IEEE Transactions on Systems, man and cybernetics* 1973; 3(6): 610–621.
- [32] Haralick RM. Statistical and structural approaches to textures. *Proceedings of the IEEE* 1979; 67(5):786-803.
- [33] Lemeshow, S., Hosmer Jr., D.W. A review of goodness of fit statistics for use in the development of logistic regression models. *Am. J. Epidemiol.* 1982; 115, 92–106.

4 MRI-based prediction of response to whole-brain helical tomotherapy with simultaneous intralesional boost for metastatic brain cancer using quantitative size and appearance features

4.1 Introduction

Metastatic brain tumors are an important public health issue, with 20%–40% of patients having solid tumors subsequently developing symptomatic brain metastases¹, and approximately 150,000 annual brain metastasis diagnoses annually in the United States. With recent improvements in diagnostic imaging and increasing patient survival due to improved systemic cancer control, the incidence of intracranial metastatic disease is projected to rise². Whole brain radiotherapy (WBRT) is widely used in the treatment of patients with metastatic disease and involves the delivery of a uniform dose of radiation to the entire brain³. It improves symptoms, but longer-term survivors may develop neurocognitive deficits^{4, 5}. Stereotactic radiosurgery (SRS) is a more targeted form of radiation therapy in which a higher dose of radiation is delivered to the tumor in a single treatment session. SRS combined with WBRT has been shown to yield superior local control, as compared with WBRT alone⁶. However, SRS has a higher frequency of side effects related to brain tissue necrosis and edema, which can put pressure on surrounding healthy brain tissue. SRS also requires separate localization and treatment procedures that add cost and patient inconvenience. Depending on the SRS system used, invasive immobilization devices may be needed, increasing patient discomfort. In addition, the

sequential delivery of WBRT and SRS does not allow integration of radiation delivery across both components, limiting the ability to fully optimize the radiation dose.

Helical tomotherapy (HT) and volumetric modulated arc therapy (VMAT) are two radiotherapy delivery technologies that allow for radiosurgery-type simultaneous infield boost (SIB) treatments to be given synchronously with the standard WBRT dose, and in this way be used to efficiently boost multiple brain metastases without the need for separate stereotactic procedures^{7,8}. The ability to incorporate this boost contribution with larger field volumes as part of the treatment planning optimization process provides an advantage of this WBRT+SIB strategy over sequential WBRT and SRS. During fractionated radiotherapy, reassortment and reoxygenation may occur between treatments, resulting in increased efficacy of subsequent doses in the treatment course; single-fraction treatments cannot exploit these radiobiologic properties⁹. Although WBRT+SIB has potential advantages compared to surgery and SRS, it is not necessarily appropriate for every patient. Some patients' tumors may not respond to WBRT+SIB, and would be more appropriately treated with radiosurgery or conventional surgery despite the additional risks and side effects. A means for predicting response to WBRT+SIB based on pre-treatment imaging could support the selection of the best treatment for each individual lesion as early as possible while the metastatic lesion has the greatest chance of control.

As a first step toward a broader objective of developing a means for response prediction to WBRT+SIB, the goal of this study was to determine whether quantitative measurements of tumor size and appearance on a magnetic resonance imaging (MRI)

scan acquired prior to treatment could be used to differentiate responder and non-responder lesion groups after WBRT+SIB using HT (henceforth WBHT+SIB) treatment of metastatic disease of the brain. In this study, we used the longest axial diameter (as used in Response Assessment Criteria in Solid Tumors [RECIST] measurements¹⁰ and the 3D volume as the measure of tumor size. To measure imaging appearance, we used three first-order features (the mean signal intensity, standard deviation of the signal intensity, and skewness of the intensity histogram) and five second order texture features (entropy, homogeneity, inertia, correlation and energy).

4.2 Materials and methods

4.2.1 Materials

This study was approved by the Human Subjects Research Ethics Board of our institution and informed consent was obtained from all patients. We recruited 21 patients for the study. These 21 patients had a total of 31 lesions. Inclusion criteria were: histologic diagnosis of primary cancer; contrast-enhanced MRI demonstrating 1–3 metastases within 6 weeks of study enrollment; age ≥ 18 years; Karnofsky performance status ≥ 70 ; anticipated survival ≥ 3 months; extracranial disease controlled; to be treated, or absent. Exclusion criteria were: metastases not suitable for SIB (> 3 lesions or any lesion maximum diameter > 3 cm, metastases within 5 mm of brainstem or optic apparatus, evidence of leptomeningeal spread, intracranial extension of an osseous metastasis, evidence of intraventricular or subependymal growth), prior cranial radiotherapy, concurrent cytotoxic chemotherapy, contraindications to MRI or gadolinium contrast. The patients underwent HT with 30 Gy WBRT and 60 Gy SIB in 10 fractions at the

London Regional Cancer Program, London Health Science Centres, Canada. Figure 4.1 illustrates the isodose curves for a 60 Gy/10-fraction WBHT+SIB case.

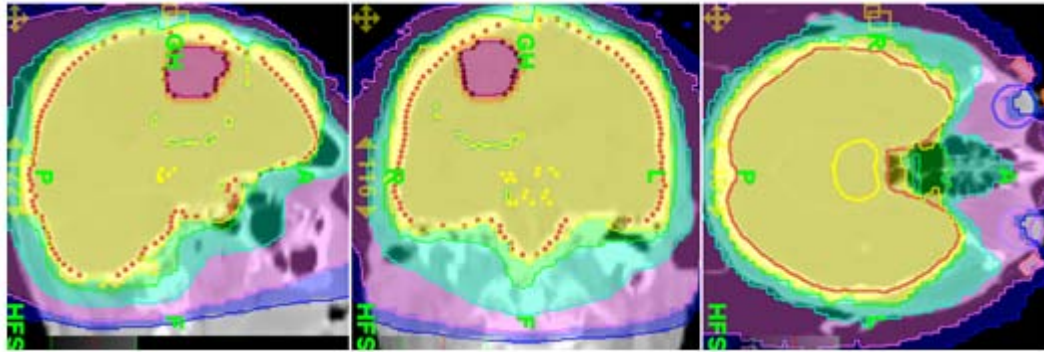


Figure 4.1 Isodose curves for an HT plan, illustrating a whole brain radiation plan (yellow = 30Gy) with integrated high-dose boost (purple = 60Gy) to a metastatic lesion.

For each patient, we acquired pre-treatment and post-treatment T1-weighted (T1W) gadolinium contrast-enhanced MRI scans (for an overall total of $21 \times 2 = 42$ scans) using 3D spoiled gradient echo sequence (repetition time: 8.84 msec, echo time: 3.47 msec, slice thickness: 2 mm, matrix size: 512×512 , flip angle: 13°). The mean time between the baseline and follow-up scans was 3.4 months (range 1–6 months). Imaging was performed on a 1.5 Tesla General Electric Signa HDxt MRI scanner (GE Healthcare, Waukesha, WI, USA).

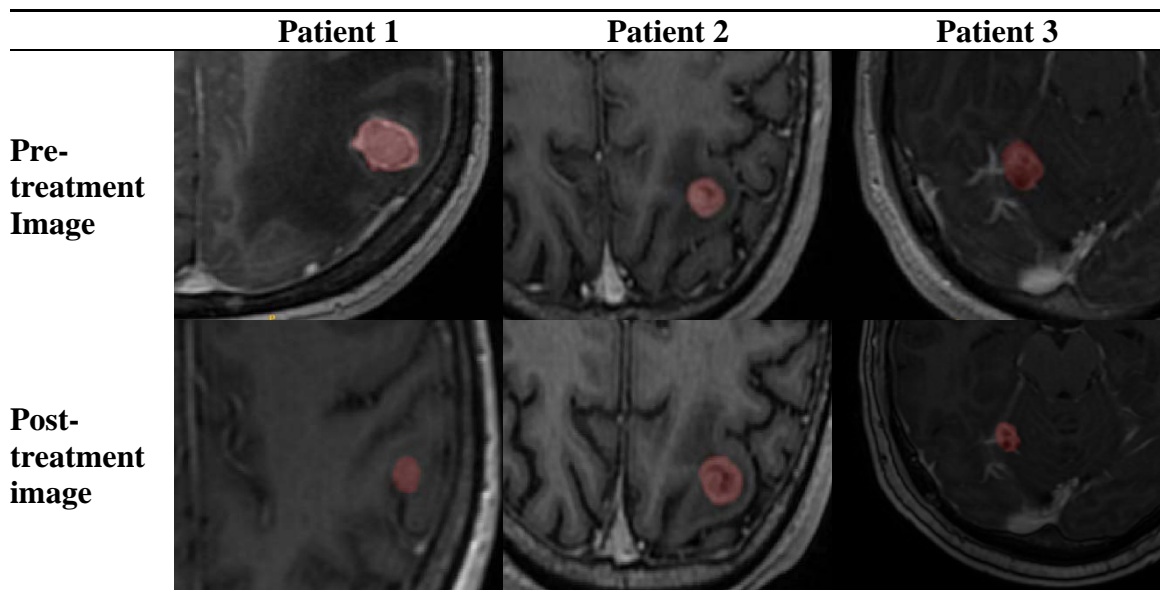


Figure 4.2 Sample images of brain metastases at the pre-treatment and follow-up imaging time points, with manual contours overlaid in red. Note the variability of MRI appearance of the different lesions.

Table 4.1 Primary site of metastasis for non-responders and responders

Primary Site	Number of Non-responding lesions	Number of Responding lesions
Breast	4	1
Melanoma	3	3
Lung	1	8
Colon	1	0
Kidney	4	0
Parotid	1	0
Thyroid	1	0
Prostate	0	3
Unknown	1	0

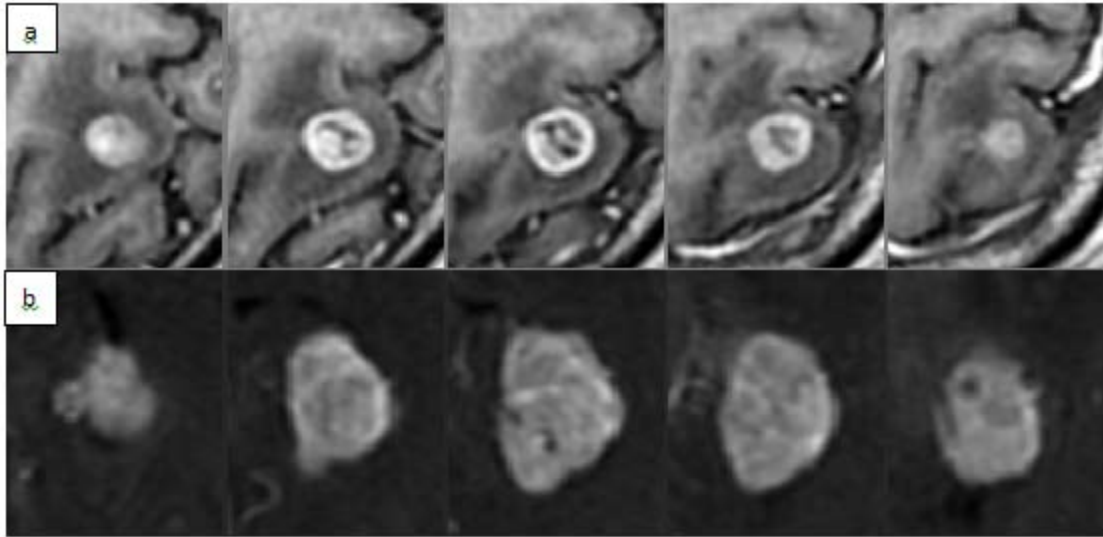


Figure 4.3 Representative axial cross sections from inferior (left) to superior (right) of two tumors, one in each row. The tumor in the first row (a) had a standard deviation of 375.79 within its core region. The tumor in the second row (b) had a standard deviation of 238.97 within its core region. The higher standard deviation value in the upper tumor is reflective of the more variegated texture within the tumor; bright pixels are sometimes neighbouring bright pixels, but are also sometimes neighbouring dark pixels; the correlation between intensities of neighbouring pixels is not as high as in the tumor in the second row.

4.2.2 Methods

3D lesion contouring on the post-contrast T1W MR images was performed by a radiation oncologist with expertise in treatment of brain metastases using ITK-SNAP (Version 2.4.0) for all the baseline and follow-up lesions¹¹. The regions enclosed by the contours were recorded as 3D binary label maps. All subsequent image processing and data analysis was performed using Matlab 7.1 (The Mathworks Inc., Natick, MA, USA).

The longest diameter lying entirely within tumor tissue on any axial slice for each lesion was calculated based on the 3D binary label maps according to the Response Evaluation Criteria in Solid Tumors (RECIST) 1.1 guidelines¹⁰. For each lesion, the percentage change in RECIST was calculated as $100\% \times (\text{follow-up RECIST} - \text{baseline RECIST}) / \text{baseline RECIST}$. Lesions with a percentage change in RECIST of $\leq -30\%$ were grouped as *responders* (15 lesions), with the remainder of the patients grouped as *non-responders* (16 lesions), according to the RECIST guidelines for clinical assessment¹⁰.

Measures of size and appearance were computed on each 3D contoured tumor, as well as on two tumor subregions, defined as follows. The 3D binary label maps were automatically separated by software into two regions: a peripheral region intended to correspond to the tumor rim, and the remaining region intended to correspond to the tumor core. The rim was defined as the set of image voxels within 3 mm of the tumor boundary on each slice within each 3D tumor. The core was defined as the set of image voxels on the inside of the tumor and not within the rim.

Inspired by qualitative categorizations of metastases as “homogeneous”, “heterogeneous”, and “rim-enhancing” in related work in the SRS context^{12,13}, we calculated the following features for each tumor and its subregions: (1) 3D tumor volume (number of voxels within the contoured tumor \times voxel size), (2) tumor diameter, (3) mean T1W signal intensity, (4) standard deviation of the T1W signal intensity, (5) skewness, (6) information entropy of the T1W signal intensity histogram, (7) homogeneity, (8) inertia, (9) energy, (10) correlation, and (11) the ratio of mean intensity within the rim to mean intensity within the core (henceforth rim:core ratio). Features (1) and (2) are size measures. Features (3)–(5) are first-order appearance and texture measures. Features (6)–(10) are a subset of the Connors and Harlow second-order texture features¹⁴ and were calculated based on a gray-level co-occurrence matrix (GLCM) g , where $g(i, j)$ contains the number of neighbouring pixels having intensities i and j . Each GLCM-based feature was calculated as follows:

$$\text{homogeneity} = \sum_{i,j} \frac{1}{1+|i-j|} g(i, j),$$

$$\text{inertia} = \sum_{i,j} (i - j)^2 g(i, j),$$

$$\text{energy} = \sum_{i,j} g(i, j)^2, \text{ and}$$

$$\text{correlation} = \sum_{i,j} \frac{(i-\mu)(j-\mu)g(i,j)}{\sigma^2}.$$

Images were quantized to 60 gray levels and we computed four GLCMs with neighboring pixels defined in angular directions of 0, 45, 90 and 135. For each axial slice containing tumor, a single GLCM was constructed from the sum of the four GLCMs taken in each

direction. These slice-wise GLCMs were then summed to produce a final GLCM, from which the texture features were calculated.

Kolmogorov-Smirnov tests were used to assess the normality of the distributions of the data. Mann-Whitney U tests were conducted to test for significant differences between the medians of the two groups (responders and non-responders), with $\alpha = 0.05$. Receiver operating characteristic (ROC) curve analyses were performed for each feature independently and areas under the curves (AUC) were computed. ROC curve analysis was conducted using the SPSS software package (IBM SPSS, Version 21, Chicago, IL).

4.3 Results

Table 4.2 shows the median and interquartile range (IQR) of each feature within each group for the whole tumor, as well as the result of the Mann-Whitney U test for each feature. Tables 4.3 and 4.4 show the same information for the core and rim regions, respectively, although for these regions only the appearance measures, not the size measures, were calculated as the sizes of the rim and core are directly correlated with the size of the whole tumor. For the whole tumor and for the core region, significant differences in median tumor diameter, 3D volume, and second-order homogeneity, inertia, correlation, and energy were found. For the rim region, significant differences in homogeneity, inertia and energy were found. For the whole tumor, the 3D volume measure had a smaller p-value, compared to the tumor diameter measure. For all significant differences, non-responders had larger 3D volume, diameter, inertia, and correlation values, and smaller homogeneity and energy values. Figures 4.4, 4.5 and 4.6

shows box and whisker plots for features found to be significant, to graphically illustrate the differences between the groups.

Table 4.5 shows the AUC values for the three top-performing individual features, as well as the optimal thresholds (chosen as the upper left-most points on the ROC curves). In addition, logistic regression was done to examine combined performance of the variables, and we calculated the AUC yielded by the combination of the best-performing size measure (tumor 3D volume) and the best-performing appearance measure (core correlation) to investigate whether the combination of size and appearance characteristics would yield improved per-patient prediction of response. This combination did not outperform the measure of core correlation. The threshold shown in Table 4.5 for this feature combination is on the response variable from the logistic regression model.

Table 4.2 Feature values measured for each group in the whole tumor. For rows with $p < 0.05$, the larger median is underlined.

Feature	Responders (median \pm IQR)	Non-responders (median \pm IQR)	p-value
3D volume (mm³)	1326 \pm 2529	<u>3879</u> \pm 7120	0.01
Tumor diameter	17.8 \pm 12.1	<u>24.1</u> \pm 15.0	0.03
T1W signal intensity	1369 \pm 1723.7	1199 \pm 885.1	0.24
SD T1W signal intensity	466.1 \pm 441.6	339.7 \pm 271.6	0.39
Skewness	0.04 \pm 0.56	0.11 \pm 0.72	0.67
Entropy	9.7 \pm 2.0	10.1 \pm 1.3	0.67
Homogeneity	<u>0.998</u> \pm 0.001	0.997 \pm 0.002	0.02
Inertia	0.25 \pm 0.20	<u>0.35</u> \pm 0.22	0.02
Correlation	0.93 \pm 0.05	<u>0.95</u> \pm 0.02	0.03
Energy	<u>0.995</u> \pm 0.004	0.993 \pm 0.007	0.01
Rim:core ratio	0.73 \pm 0.16	0.66 \pm 0.14	0.73

Table 4.3 Feature values measured for each group in the tumor core. For rows with $p < 0.05$, the larger median is underlined.

Feature	Responders (median \pm IQR)	Non-responders (median \pm IQR)	p-value
T1W signal intensity	1382.9 \pm 2005.2	1240.6 \pm 900.7	0.22
SD T1W signal intensity	390.7 \pm 366.8	334.6 \pm 290.9	0.48
Skewness	0.09 \pm 0.41	0.15 \pm 0.86	0.95
Entropy	9.62 \pm 2.1	9.90 \pm 1.6	0.46
Homogeneity	0.9987 \pm 0.001	0.9981 \pm 0.001	0.02
Inertia	0.34 \pm 0.28	<u>0.44</u> \pm 0.20	0.04
Correlation	0.90 \pm 0.07	<u>0.93</u> \pm 0.02	<0.01
Energy	<u>0.996</u> \pm 0.004	0.994 \pm 0.007	0.01

Table 4.4 Feature values measured for each group in the tumor rim. For rows with $p < 0.05$, the larger median is underlined.

Feature	Responders	Non-responders	p-value
	(median \pm IQR)	(median \pm IQR)	
T1W signal intensity	1082.3 \pm 1100.9	830.3 \pm 510.8	0.19
SD T1W signal intensity	359.2 \pm 304.4	230.9 \pm 235.9	0.41
Skewness	0.69 \pm 0.47	0.83 \pm 0.65	0.29
Entropy	9.44 \pm 1.41	9.73 \pm 1.5	0.82
Homogeneity	0.9986 \pm 0.0008	0.9984 \pm 0.0008	0.03
Inertia	0.56 \pm 0.27	0.74 \pm 0.29	0.03
Correlation	0.79 \pm 0.02	0.79 \pm 0.02	0.70
Energy	0.996 \pm 0.002	0.995 \pm 0.002	0.03

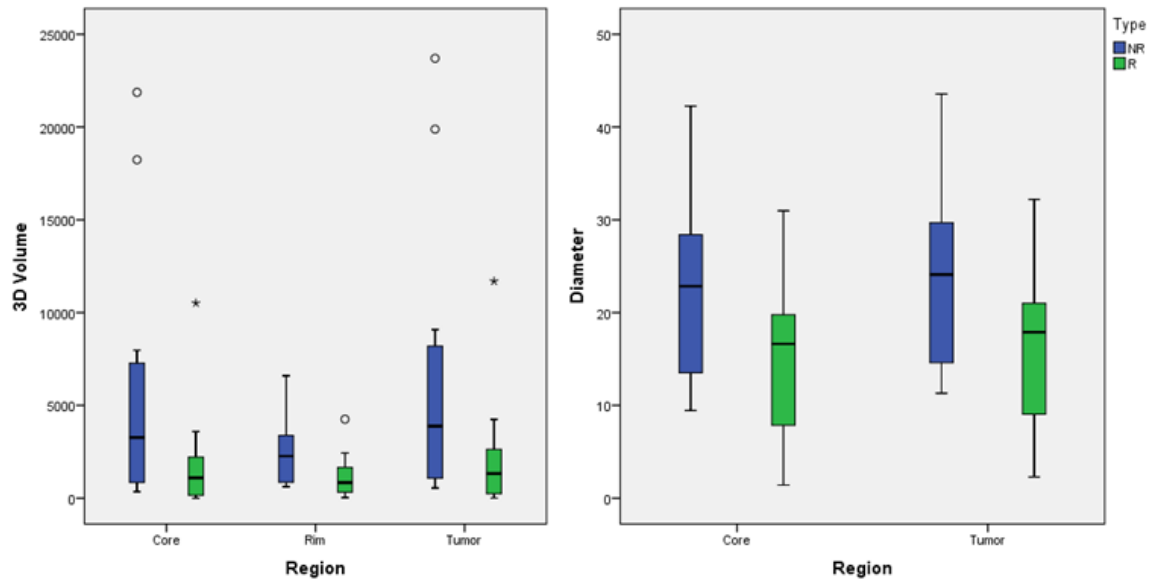


Figure 4.4 Boxplots for 3D volume and Diameter for the whole tumor, the core, and rim regions, comparing responders (R) and non-responders (NR).

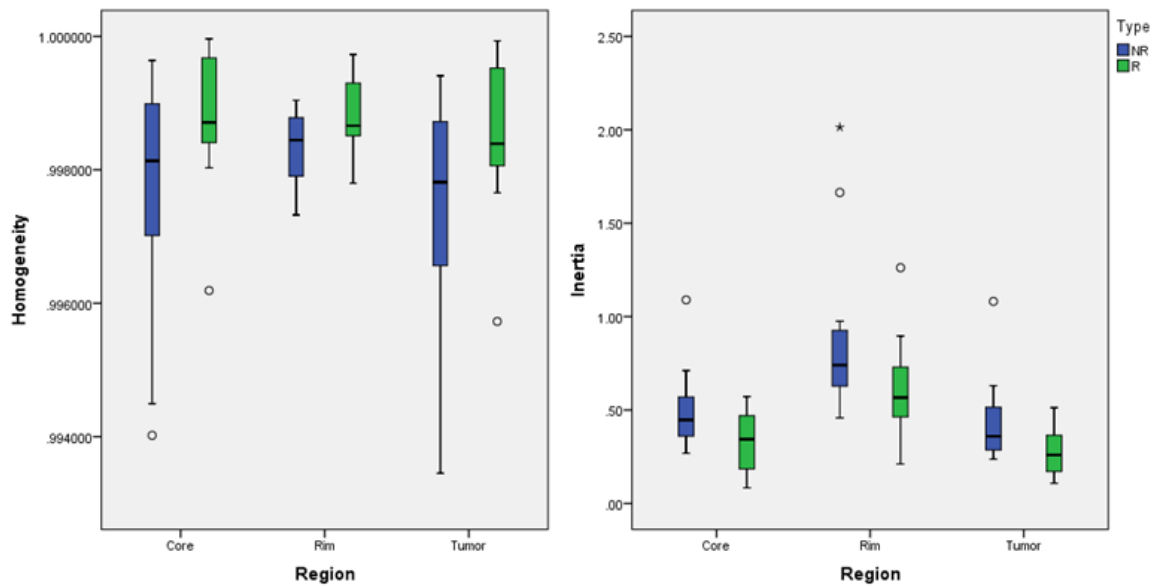


Figure 4.5 Boxplots for Homogeneity and Inertia for the whole tumor, the core, and rim regions, comparing responders (R) and non-responders (NR).

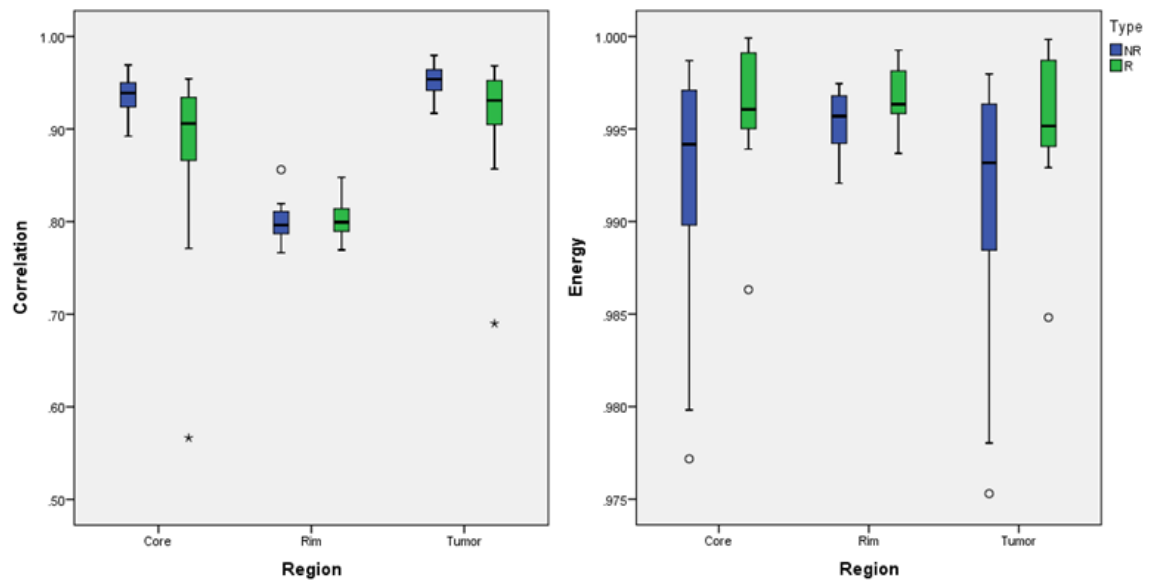


Figure 4.6 Boxplots for Correlation and energy for the whole tumor, the core, and rim regions, comparing responders (R) and non-responders (NR).

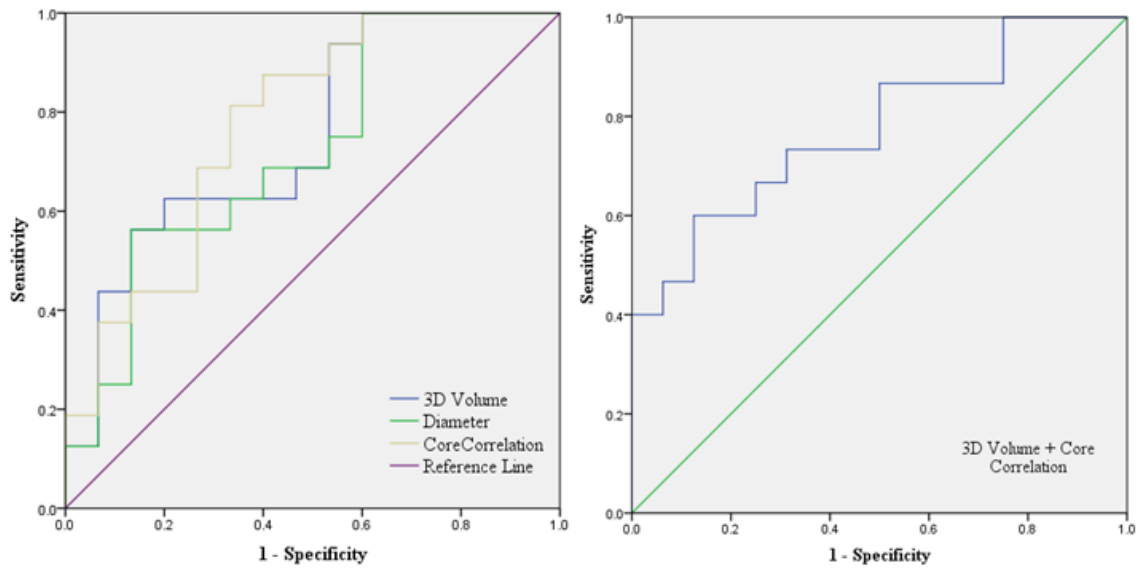


Figure 4.7 ROC curves for the four features that had the largest AUCs (Table 4.4).

Table 4.5 Optimal thresholds of features having the four largest AUCs.

Features	AUC	Threshold
Tumor 3D Volume	.75	2154
Tumor Diameter	.72	16.84
Core Correlation	.77	0.92
Combined (core correlation +3D volume)	.77	0.32

4.4 Discussion

The role of brain radiotherapy has been a source of controversy since some patient populations show limited clinical benefit¹⁵. WBRT is widely used in the treatment of patients with metastatic disease¹⁶ since it is technically easy to deliver and it improves symptoms in 75% of symptomatic patients with brain metastases^{17,18}, but long-term survivors may develop neurocognitive deficits^{4,5} and local control may be inadequate, especially in patients who live longer than a few months.

The feasibility and safety of HT+SIB using 30 Gy WBRT with intralesional boost of 60 Gy has been shown by Rodrigues et al. in a phase I clinical trial⁷. For selected patients with brain metastasis, aggressive treatment of the individual lesions with high dose radiation combined with a lower dose of radiation to the remainder of the brain has produced the best results in terms of controlling cancer in the brain and preventing new lesions from developing²². HT allows for radiosurgery-type SIB treatments to be given synchronously with the standard WBRT dose, and can be used efficiently to boost multiple brain metastases without the need for separate stereotactic procedures^{7,8}. Bauman et al. have shown that the WBHT+SIB strategy is also relatively independent of the number of lesions being boosted and may be a feasible strategy for treating multiple intracranial lesions efficiently¹⁹.

In this study, we investigated size and imaging appearance features of the whole tumor, tumor rim and tumor core for differentiation of patient groups that would benefit from the WBHT+SIB therapy for brain metastases. This is the first study to apply quantitative size and imaging texture measures of tumors to measure the differences on pre-treatment

contrast-enhanced T1-weighted MRI between responders and non-responders to helical tomotherapy with simultaneous infield boost for intracranial metastases. Our approach adapts and extends previous work in the stereotactic radiosurgery context by using quantitative measures that are related to previously used categorical subjective tumor assessments. To measure imaging appearance, we used three first-order features (the mean signal intensity, standard deviation of the signal intensity, and skewness) derived from the gray-level histogram, where mean and standard deviation are the mean of the gray-levels and the measure of deviation of these gray-levels in the image, while skewness is the asymmetry of the distribution of the gray-levels. We also tested five second order texture features (entropy, homogeneity, inertia, correlation and energy) which are calculated from the GLCM, where GLCM provides an estimate of the joint probability of the intensity values of neighboring pixels. The use of these predictive markers could help to identify the lesions which would benefit from WBHT+SIB (responders) while sparing the non- responders which would not benefit so that the latter may be treated with other combinations of therapies. For the former group of lesions, WBHT+SIB may represent an effective and less invasive option compared to traditional combinations of surgery or radiosurgery combined with WBRT.

For the whole tumor, size measures of 3D volume and diameter were significantly different between the responders and non-responders with responders having smaller size tumors than the non-responders. One possible explanation for the limited response of large tumors is related to the presence of hypoxic regions. Hypoxic regions are resistant to radiation damage²³. During the course of fractionated WBHT + SIB treatment, smaller hypoxic regions may become reoxygenated and therefore may be more sensitive to

radiation damage. Conversely, larger tumors have bigger hypoxic regions that may need more fractionated radiation delivery (>15 fractions) than is currently used in clinical settings.

Appearance measure of first-order features did not show any significant differences between the groups. Second-order features of homogeneity, inertia, correlation and energy showed significant differences between the two groups. Figure 4.3a-b shows an example of the differences in the standard deviation (SD) and correlation values for the two patients. The tumor in the first row (4.3a) had a SD value of 375.79 and correlation value of 0.89 within its core region. The tumor in the second row (4.3b) had a SD value 238.97 and correlation value of 0.97 within its core region. The lower correlation value in the upper tumor is reflective of the more variegated texture within the tumor and the correlation between intensities of neighbouring pixels is not as high as in the tumor in the second row.

Since the tumor appears to have a hypodense core and a hyperintense rim, we also looked at the first and second order texture features separately for each of the two regions (the tumor core and tumor rim) to assess whether separating the two regions would give us better predictive capability. For the core region, we saw similar results to that of the tumor as a whole. Core size measures of 3D volume, tumor diameter and second-order appearance measures of homogeneity, inertia, correlation and energy were significantly different between the responders and non-responders groups. For the rim region, the size measure of 3D volume and second-order features of homogeneity inertia and energy were significantly different between the two groups. To investigate the predictive value of an

enhancing rim and/or a necrotic core, we calculated the rim-core ratio. No significant difference was seen for the rim-core ratio between the responder and non-responder groups. The AUC for the ROC curve (0.46) of rim-core ratio feature was very low, suggesting that the appearance (or lack thereof) of an enhancing rim or necrotic core on the pre-treatment image may not predict response at first follow-up.

For all three regions (tumor, core, rim), no significant differences were seen in the first-order features of T1w signal intensity and SD between the responders and non-responders suggesting that the T1w signal intensity and SD may not be useful as a predictive marker for response to WBHT+SIB therapy. The failure to detect statistical significance for the first-order texture features for the three regions may imply that the global appearance of the tumor may be less important than the local pixel intensity relationships to prediction of WBHT+SIB treatment response. Further testing of this observation will require greater statistical power with a larger sample size.

There are several limitations to this study. First, all the contours were drawn by a single observer; further study is required to measure the impact of observer contouring variability on the size and appearance measures used in this study. Second, our sample size necessitates that the results of this study be considered hypothesis-generating, with more extensive validation required on a separate data set. Third, although our study tested a subset of the Conners and Harlow second-order texture features¹⁴, this does not constitute an exhaustive evaluation of the texture measures that have been proposed, so firm conclusions regarding the predictive power of appearance measures in general

cannot be drawn from the results of this study and further investigation of alternative texture measures is required. Fourth, the texture measure of T1w signal intensity was not normalized. Although this parameter was not significantly different between the two groups, factors such as coil loading may have increased the variance of the measured signal intensity. In the future a quantitative approach should be taken²⁴ to measure the absolute T1 of the tissue for texture analysis. Finally, the logistic regression model's performance on a separate validation set should be explored in future work on a larger data set.

Metastatic brain lesion size and second order appearance as measured on pre-treatment MRI can distinguish responders from non-responders to WBHT+SIB. . The results of this study suggest that the 3D tumor volume and the second-order correlation texture measure within the tumor core are the best predictors, with smaller lesions ($< 2.1 \text{ cm}^3$) and those with a relatively smaller second order core correlation value (< 0.92) having a greater rate of response to WBHT+SIB. The results also suggest that the longest axial diameter (as measured in RECIST) could be a useful surrogate for 3D volume, with tumors having diameters $< 1.7 \text{ cm}$ responding more favorably to treatment. Appearance measures in general can quantify visual changes but they did not substantially outperform measures of size; there is high variability of appearance in both responders and non-responders to WBHT+SIB. The amount of rim enhancement and/or core necrosis, as reflected in our signal intensity measures did not provide useful prediction of response. Ongoing work on a larger sample size will include further validation of our results and the development of an approach to per-lesion prediction of response to WBHT+SIB therapy based on pre-treatment MRI, supporting optimal treatment selection.

4.5 References

- [1] Kondziolka D, Martin JJ, Flickinger JC, Brufsky AM, Baar J, Kirkwood JM, Lunsford LD. Long term survivors after gamma knife radiosurgery for brain metastases. *Cancer* 2005; 104(12):2784–91.
- [2] Patel TR, McHugh BJ, Bi WL, Minja FJ, Knisely JP, Chiang VL. A comprehensive review of MR imaging changes following radiosurgery to 500 brain metastases. *AJNR Am J Neuroradiology* 2011; 32(10):1885-92.
- [3] Sneed PK et al., *Neurosurgery Clinics of North America* 1996; 7:505–515.
- [4] Eichler AF, Loeffler JS. Multidisciplinary management of brain metastases. *Oncologist* 2007; 12(7):884-98.
- [5] Asai A, Matsutani M, Kohno T, Nakamura O, Tanaka H, Fujimaki T, Funada N, Matsuda T, Nagata K, Takakura K.. Subacute brain atrophy after radiation therapy for malignant brain tumor. *Cancer* 1989; 63(10):1962-74.
- [6] Sneed PK, Lamborn KR, Forstner JM, McDermott MW, Chang S, Park E, Gutin PH, Phillips TL, Wara WM, Larson DA. Radiosurgery for brain metastases: is whole brain radiotherapy necessary? *Int J Radiat Oncol Biol Phys.* 1999; 43(3):549-58.
- [7] Rodrigues G, Yartsev S, Yaremko B, Perera F, Dar AR, Hammond A, Lock M, Yu E, Ash R, Caudrelier JM, Khuntia D, Bailey L, Bauman G. Phase I trial of simultaneous in-field boost with helical tomotherapy for patients with one to three brain metastases 201; 80(4):1128-33.
- [8] Lagerwaard F, Van der hoorn EA, Verbakel WF, Haasbeek CJ, Slotman BJ, Senan S. Whole brain radiotherapy with simultaneous integrated boost to multiple brain metastases using volumetric modulated arc therapy. *Int J Radiat Oncol Biol Phys* 2009; 75(1):253–9.

- [9] Hall EJ, Brenner DJ. The radiobiology of radiosurgery: rationale for different treatment regimes for AVMs and malignancies. *Int J Radiat Oncol Biol Phys* 1993; 25(2):381–5.
- [10] Eisenhauer EA, Therasse P, Bogaerts J, Schwartz LH, Sargent D, Ford R, Dancey J, Arbuck S, Gwyther S, Mooney M, Rubinstein L, Shanker L, Dodd L, Kaplan R, Lacombe D, Verweij J. New response evaluation criteria in solid tumors: revised RECIST guideline (version 1.1). *European Journal of Cancer* 2009; 45(2):228–47.
- [11] Yushkevich PA , Piven J , Hazlett HC, Smith RG, Ho S, Gee JC , Gerig G. User-guided 3D active contour segmentation of anatomical structures: Significantly improved efficiency and reliability. *Neuroimage* 2006; 31:1116-28.
- [12] Goodman KA, Sneed PK, McDermott MW, Shiau CY, Lamborn KR, Chang S, Park E, Wara WM, Larson DA. Relationship between pattern of enhancement and local control of brain metastases after radiosurgery. *Int J Radiat Oncol Biol Phys* 2001; 50(1), 139–46.
- [13] Rodrigues G, Zindler J, Warner A, Lagerwaard F. Recursive partitioning analysis for the prediction of stereotactic radiosurgery brain metastases lesion control. *The Oncologist* 2013; 18(3):330–5.
- [14] Connors RW, Harlow CA. A theoretical comparison of texture algorithm. *IEEE Transactions in Pattern Analysis and Machine Learning* 1980; 2(3):204–22.
- [15] Nieder C, Mehta MP. Prognostic indices for brain metastases--usefulness and challenges. *Radiation Oncology* 2009; 4:10.
- [16] Sneed PK, Larson DA, Wara WM. Radiotherapy for cerebral metastases. *Neurosurgical Clinics of North America* 1996; 7:505-515.
- [17] Borgelt B, Gelber R, Kramer S, Brady LW, Chang CH, Davis LW, Perez CA, Hendrickson FR.. The palliation of brain metastases: Final results of the first two

- studies by the Radiation Therapy Oncology Group. *International Journal of Radiation Oncology Biology Physics* 1980; 6(1): 1-9.
- [18] Markesbery WR, Brooks WH, Gupta GD, Young AB. Treatment for patients with cerebral metastases. *Archives of Neurology* 1978; 35(11):754-756.
 - [19] Bauman G, Yartsev S, Fisher B, Kron T, Laperriere N, Heydarian M, VanDyk J. Simultaneous infield boost with helical tomotherapy for patients with 1 to 3 brain metastases. *American Journal of Clinical Oncology* 2007; 30(1):38-44.
 - [20] Brown JM, Diehn M, Loo B. Stereotactic ablative radiotherapy should be combined with a hypoxic cell radiosensitizer. *International Journal of Radiation Oncology Biology Physics* 2010; 78(2):323–7.
 - [21] Levegrün S, Pottgen C, Wittig A, Lubcke W, Jawad JA, Stuschke M. *International Journal of Radiation Oncology Biology Physics* 2013; 86(4):734–42.
 - [22] Kondziolka D, Patel A, Lunsford D, Kassam A, Flickinger J. Stereotactic radiosurgery plus Whole brain radiotherapy versus radiotherapy alone for patients with multiple brain metastasis, *Int. J. Radiation Oncology Biol. Phys* 1999; 45(2):427–434.
 - [23] Wachsberger P, Burd R, Dicker A. Tumor Response to Ionizing Radiation Combined with Antiangiogenesis or Vascular Targeting Agents: Exploring Mechanisms of Interaction. *Clinical Cancer Research* 2003;9:1957-1971.
 - [24] Deoni SC, Peters TM, and Rutt BK. High-resolution T1 and T2 Mapping of the Brain in a Clinically acceptable time with DESPOT1 and DESPOT2, *Magnetic Resonance in Medicine* 2005; 53: 237-241

5 Conclusion and Future Work

This thesis addresses important questions about improving the detection of brain tumor recurrence following treatment, differentiating glioblastoma from metastasis using quantitative texture parameters, and improving patient selection for helical tomotherapy type whole brain radiation therapy with simultaneous infield boost. The main scientific contributions are summarized below.

5.1 Multiparametric Imaging in Patients with Glioblastoma

GBMs are the most malignant form of primary brain tumor where recurrences are common even after surgery and chemo-radiation therapy¹. Discrimination of tumor from radiation injured tissue is essential for guiding proper surgical and radiotherapy treatments since tumor recurrences and radiation injury (RI) have similar appearance on follow-up conventional magnetic resonance imaging^{2, 3} (MRI). There have been numerous attempts to differentiate tumor recurrences from RI using various functional imaging modalities such as CT, MRI, single-photon emission computed tomography and positron emission tomography, however biopsy is still the gold standard. DTI derived parameters have been used in an attempt to differentiate tumor¹⁶ from radiation injury. The AxD parameter showed significant differences between the tumor region and RI region. Other DTI parameters like FA, MD and RD showed no significant differences between the two regions¹⁶. The majority of the studies that were performed to differentiate tumor recurrence from RI had no histopathological verification^{4,5} of the final

diagnosis and most of these studies were retrospective^{4,6}. A search for an accurate technique to differentiate tumor from RI continues. As described in Chapter 2 we did not see significant differences in the diffusion tensor parameters between the two groups. Instead, we have shown that correlations between diffusion tensor parameters and routine MRI signal intensities were significant and may be able to differentiate the tumor regions from radiation injured regions. In this study we used perfusion CT information along with FLAIR images to separate the tumor regions from radiation injured regions. This was based on the numerous studies that have successfully correlated perfusion properties of tumors with histology, and have shown that progressive or recurrent tumors have high permeability compared to RI regions^{7,8,9}. The correlation of MRI signal intensity values from FLAIR and diffusion tensor parameters is a novel approach that was tested on a small group of patients. The preliminary results from this study require further investigation with a larger patient population to confirm our initial findings and provide estimates as to the accuracy and diagnostic utility of this new method. In future studies the tumor regions would need to be confirmed histologically, which is the current gold standard.

5.2 Texture Analysis in Differentiating between Glioblastoma and Metastasis

Glioblastoma and metastasis (MET) are the two most common types of brain tumor and both these of tumor types exhibit similar radiologic appearance on routine MR imaging¹⁰.

¹¹. Differentiating between GBM and MET is very important because they have different biological mechanisms and require different treatment strategies. Many studies have focused on advanced imaging modalities¹²⁻¹⁴ such as diffusion tensor imaging, perfusion MRI, spectroscopy, and perfusion CT for non-invasively differentiating between these two types of tumor. These advanced imaging modalities require long scan times, expertise in advanced imaging, and additional imaging modalities in the case of CT, which increases cost, examination time, and patient exposure to radiation. Since T1w imaging is part of routine brain tumor MRI examination, our technique utilizes easily accessible MR images and provides quantitative information without additional cost. In our current study (Chapter 3) we have shown that first-order texture feature of standard deviation and second-order texture features of entropy, inertia, homogeneity, and energy may be able to differentiate between the two groups. ROC curve analysis showed combining first- and second-order features increases the predictive accuracy in differentiating between GBM and MET. When used individually, the second order texture feature of inertia had the best predictive accuracy followed by homogeneity and energy. This study was the first attempt to quantify the texture appearance of the tumor and use it as an indicator in order to differentiate between GBM and MET. The simplicity of implementing our technique makes it more desirable than other advanced techniques. In future studies, various models can be created with combinations of these texture parameters. With further evaluation and validation of the models on a larger sample size, these models can be used in clinical settings to predict tumor types with routine MR

images. This would prevent needless tumor biopsies and cut down the imaging and ultimately examination time.

5.3 Texture Analysis in Patient Selection for Radiation Therapy

Helical tomotherapy (HT) is a radiation delivery technique that allows for a radiosurgery-type simultaneous infield boost (SIB) of multiple brain metastases^{15, 16} synchronously with whole brain radiation therapy (WBRT) without separate stereotactic procedures. Patient selection is crucial since some patients' tumors may not respond to HT type WBRT+SIB. In our current study (Chapter 4), as a first step toward the broader objective of developing a means for response prediction, we have demonstrated that smaller size lesions may respond better to this type of radiation therapy. We have also shown that measures of appearance provide limited added value for response prediction. Size measures have also been shown to be a good prognostic factor for the SRS type of radiation therapy¹⁷. Qualitative assessment of the lesions may also predict the success of the SRS type of radiosurgery¹⁸. None of these predictors have previously been studied for the WBHT + SIB type of radiation therapy. Our study was the first attempt to quantify the texture appearance of the lesions and use it as an indicator for the prediction of tumor response to the WBHT + SIB type of radiation therapy. The use of these predictive markers can help identify the groups of patients who would benefit from WBHT+SIB (responders) while sparing the non-responders who would not benefit so that the latter

may be treated with other therapies. For the responders, this type of radiation therapy may represent an effective and less invasive option compared to the traditional combinations of surgery, or radiosurgery combined with WBRT. Future work with a larger sample size will support further validation of our results. This will lead to the development of a per-lesion prediction of response approach based on pre-treatment MRI, which will support optimal treatment selection for patients with multiple brain metastases.

5.4 References

- [1] Yang I, Aghi MK. New advances that enable identification of glioblastoma recurrence. *Nature reviews in clinical oncology*, Vol 6, 648-657. 2009
- [2] Chamberlain MC, Glantz MJ, Chalmers L, Van Horn A, Sloan AE. Early necrosis following concurrent Temodar and radiotherapy in patients with glioblastoma. *J Neurooncol*;82(1):81–83.2007
- [3] Gasparetto EL, Pawlak MA, Patel SH,. Posttreatment recurrence of malignant brain neoplasm: accuracy of relative cerebral blood volume fraction in discriminating low from high malignant histologic volume fraction. *Radiology*;250(3):887–896. 2009
- [4] Sundgren PC, Fan X, Weybright P, Welsh RC, Carlos RC, Petrou M, McKeever PE, Chenevert TL. Differentiation of recurrent brain tumor versus radiation injury

using diffusion tensor imaging in patients with new contrast-enhancing lesions.

Magnetic Resonance Imaging 2006; 24: 1131-1142.

- [5] Bobek-Billewicz B, Stasik-Pres G, Majchrzak H, Zarudzki L. Differentiation between brain tumor recurrence and radiation injury using perfusion, diffusion-weighted imaging and MR spectroscopy. *Folia Neuropathologica* 2010; 48 (2): 81-92.
- [6] Henze M, Mohammed A, Schlemmer H, Herfarth KK, Mier W, Eisenhut M, Debus J, Haberkorn U. Detection of tumour progression in the follow-up of irradiated astrocytomas: comparison of 3-[123I]iodo- α -methyl-L-tyrosine and 99mTc-MIBI SPECT. *European Journal of Nuclear Medicine* 2002; 29(11):1455-1461.
- [7] Jain R, Narang J, Schultz L, Scarpance L, Saksena S, Brown S, Rock JP, Rosenblum M, Gutierrez J, Mikkelsen T. Permeability Estimates in Histopathology-Proved Treatment-Induced Necrosis Using Perfusion CT: Can These Add to Other Perfusion Parameters in Differentiating from Recurrent/Progressive Tumors? *American Journal of neuroradiology*. 32:658-663. 2011
- [8] Jain R, Ellika SK, Scarpance L, et al. Quantitative estimation of permeability surface-area product in astroglial brain tumors using perfusion CT and correlation with histopathologic grade. *AJNR Am J Neuroradiol* 2008;29:694–700
- [9] Jain R, Gutierrez J, Narang J, et al. In vivo correlation of tumor blood volume and permeability with histological and molecular angiogenic markers in gliomas. *AJNR Am J Neuroradiol* 2011;32:388–94

- [10] Schwartz KM, Erickson BJ, Lucchinetti C. Pattern of T2 hypointensity associated with ring-enhancing brain lesions can help to differentiate pathology. *Neuroradiology* 2006;48:143–49
- [11] Schiff, D., 2001. Single Brain Metastasis. *Curr. Treat. Options Neurol.* 3, 89–99.
- [12] Byrnes TJ, Barrick TR, Bell BA, et al. Diffusion tensor imaging discriminates between glioblastoma and cerebral metastases in vivo. *NMR Biomed* 2011;24: 54–60
- [13] Lehmann P, Saliou G, de Marco G, et al. Cerebral peritumoral oedema study: does a single dynamicMRsequence assessing perfusion and permeability can help to differentiate glioblastoma from metastasis? *Eur J Radiol* 2012;81: 522–27
- [14] Opstad KS, Murphy MM, Wilkins PR, et al. Differentiation of metastases from high-grade gliomas using short echo time ¹H spectroscopy. *J Magn Reson Imaging* 2004;20:187–92
- [15] Rodrigues G, Yartsev S, Yaremko B, Perera F, Dar AR, Hammond A, Lock M, Yu E, Ash R, Caudrelier JM, Khuntia D, Bailey L, Bauman G. Phase I trial of simultaneous in-field boost with helical tomotherapy for patients with one to three brain metastases. 2011. 15;80(4):1128-33.
- [16] Lagerwaard F, Van der hoorn EA, Verbakel WF, Haasbeek CJ, Slotman BJ, Senan S. Whole brain radiotherapy with simultaneous integrated boost to multiple brain metastases using volumetric modulated arc therapy. *International Journal of Radiation Oncology Biology Physics* 2009 75(1), 253–9.

- [17] Chang EL, Hassenbusch SJ, Shiu AS, Lang FF, Allen PK, Sawaya R, Maor MH. The role of tumor size in the radiosurgical management of patients with ambiguous brain metastases. *Neurosurgery* 2003; 53(2): 272-80.
- [18] Goodman KA, Sneed PK, McDermott MW, Shiau CY, Lamborn KR, Chang S, Park E, Wara WM, Larson DA. Relationship between pattern of enhancement and local control of brain metastases after radiosurgery. *International Journal of Radiation Oncology Biology Physics* 2001; 50(1), 139–46.

Appendix: Ethics Approval Notices



Use of Human Participants - Ethics Approval Notice

Principal Investigator: Dr. Barbara Fisher
Review Number: 15958
Review Level: Delegated
Approved Local Adult Participants: 15
Approved Local Minor Participants: 0
Protocol Title: Feasibility Study of Magnetic Resonance Spectroscopy and Dynamic Enhanced Cat Scan Imaging in Gliomas: Predictive Value for Postradiation Relapse
Department & Institution: Oncology, London Health Sciences Centre
Sponsor:
Ethics Approval Date: March 17, 2011 **Expiry Date:** January 31, 2015
Documents Reviewed & Approved & Documents Received for Information:

Document Name	Comments	Version Date
Revised UWO Protocol	Revised co-investigators (add H. Sharma), revised study methodology, revised data transfer	
Revised Letter of Information & Consent		2011/03/11

This is to notify you that The University of Western Ontario Research Ethics Board for Health Sciences Research Involving Human Subjects (HSREB) which is organized and operates according to the Tri-Council Policy Statement: Ethical Conduct of Research Involving Humans and the Health Canada/ICH Good Clinical Practice Practices: Consolidated Guidelines; and the applicable laws and regulations of Ontario has reviewed and granted approval to the above referenced revision(s) or amendment(s) on the approval date noted above. The membership of this REB also complies with the membership requirements for REB's as defined in Division 5 of the Food and Drug Regulations.

The ethics approval for this study shall remain valid until the expiry date noted above assuming timely and acceptable responses to the HSREB's periodic requests for surveillance and monitoring information. If you require an updated approval notice prior to that time you must request it using the UWO Updated Approval Request Form.

Members of the HSREB who are named as investigators in research studies, or declare a conflict of interest, do not participate in discussion related to, nor vote on, such studies when they are presented to the HSREB.

The Chair of the HSREB is Dr. Joseph Gilbert. The UWO HSREB is registered with the U.S. Department of Health & Human Services under the IRB registration number IRB 00000940.

Signature

Ethics Officer to Contact for Further Information

Janice Sutherland (jsutherland@uwo.ca)	Elizabeth Wambolt (ewambolt@uwo.ca)	Grace Kelly (grace.kelly@uwo.ca)
---	--	-------------------------------------

The University of Western Ontario

Office of Research Ethics

Room 5150, Support Services Building • London, Ontario • CANADA - N6A 3K7
PH: 519-661-3036 • F: 519-850-2466 • ethics@uwo.ca • www.uwo.ca/research/ethics



Principal Investigator: Dr. Barbara Fisher
File Number:103424
Review Level:Delegated
Approved Local Adult Participants:100
Approved Local Minor Participants:0
Protocol Title:Retrospective Imaging Review of Malignant Gliomas
Department & Institution:Schulich School of Medicine and Dentistry/Oncology,London Health Sciences Centre
Sponsor:
Ethics Approval Date:February 28, 2013 Expiry Date:February 28, 2014
Documents Reviewed & Approved & Documents Received for Information:

Document Name	Comments	Version Date
Western University Protocol		2013/01/15

This is to notify you that The University of Western Ontario Research Ethics Board for Health Sciences Research Involving Human Subjects (HSREB) which is organized and operates according to the Tri-Council Policy Statement: Ethical Conduct of Research Involving Humans and the Health Canada/ICH Good Clinical Practice Practices: Consolidated Guidelines; and the applicable laws and regulations of Ontario has reviewed and granted approval to the above referenced revision(s) or amendment(s) on the approval date noted above. The membership of this REB also complies with the membership requirements for REB's as defined in Division 5 of the Food and Drug Regulations.

The ethics approval for this study shall remain valid until the expiry date noted above assuming timely and acceptable responses to the HSREB's periodic requests for surveillance and monitoring information. If you require an updated approval notice prior to that time you must request it using the University of Western Ontario Updated Approval Request Form.

Members of the HSREB who are named as investigators in research studies, or declare a conflict of interest, do not participate in discussion related to, nor vote on, such studies when they are presented to the HSREB.

The Chair of the HSREB is Dr. Joseph Gilbert. The HSREB is registered with the U.S. Department of Health & Human Services under the IRB registration number IRB 00000940.



Ethics Officer to Contact for Further Information

Janice Sutherland (jsutherland@uwo.ca)	Grace Kelly (grace.kelly@uwo.ca)	Shantel Walcott (swalcott@uwo.ca)
---	-------------------------------------	--------------------------------------

This is an official document. Please retain the original in your files.



Office of Research Ethics

The University of Western Ontario

Room 00045 Dental Sciences Building, London, ON, Canada N6A 5C1

Telephone: (519) 661-3036 Fax: (519) 850-2466 Email: ethics@uwo.ca

Website: www.uwo.ca/research/ethics

Use of Human Subjects - Ethics Approval Notice

Principal Investigator: Dr. G.S. Bauman

Review Number: 09531

Revision Number:

Protocol Title: A feasibility study of helical tomotherapy in the palliation of locally symptomatic incurable cancer.

Department and Institution: Oncology, London Regional Cancer Centre

Sponsor: CLINICAL RESEARCH UNIT, LRCC

Approval Date: 19-Mar-03

End Date: 30-Sep-03

Documents Reviewed and Approved: UWO Protocol, Letter of information & consent form dated March 10/03

Documents Received for Information: Protocol dated July 10/02

This is to notify you that the University of Western Ontario Research Ethics Board for Health Sciences Research Involving Human Subjects (HSREB) which is organized and operates according to the Tri-Council Policy Statement and the Health Canada/ICH Good Clinical Practice Practices: Consolidated Guidelines; and the applicable laws and regulations of Ontario has received and granted full board approval to the above named research study on the date noted above. The membership of this REB also complies with the membership requirements for REB's as defined in Division 5 of the Food and Drug Regulations.

This approval shall remain valid until end date noted above assuming timely and acceptable responses to the HSREB's periodic requests for surveillance and monitoring information. If you require an updated approval notice prior to that time you must request it using the UWO Updated Approval Request Form.

During the course of the research, no deviations from, or changes to, the protocol or consent form may be initiated without prior written approval from the HSREB except when necessary to eliminate immediate hazards to the subject or when the change(s) involve only logistical or administrative aspects of the study (e.g. change of monitor, telephone number). Expedited review of minor change(s) in ongoing studies will be considered. Subjects must receive a copy of the signed information/consent documentation.

Investigators must promptly also report to the HSREB:

- a) changes increasing the risk to the participant(s) and/or affecting significantly the conduct of the study;
- b) all adverse and unexpected experiences or events that are both serious and unexpected;
- c) new information that may adversely affect the safety of the subjects or the conduct of the study.

If these changes/adverse events require a change to the information/consent documentation, and/or recruitment advertisement, the newly revised information/consent documentation, and/or advertisement, must be submitted to this office for approval.

Members of the HSREB who are named as investigators in research studies do not participate in discussion related to, nor vote on, such studies when they are presented to the HSREB.

Chair of HSREB: Dr. Paul Harding

Faxed: *UN*

Date: *Mar. 21/03*
agb

This is an official document. Please retain the original in your files.

UWO HSREB Ethics Approval

09531

Page 1 of 1



Office of Research Ethics

The University of Western Ontario
Room 4180 Support Services Building, London, ON, Canada N6A 5C1
Telephone: (519) 661-3036 Fax: (519) 850-2466 Email: ethics@uwo.ca
Website: www.uwo.ca/research/ethics

Use of Human Subjects - Ethics Approval Notice

Principal Investigator: Dr. G. Rodrigues

Review Number: 16776

Review Date: January 26, 2010

Review Level: Full Board

Approved Local # of Participants: 50

Protocol Title: A Phase II Multi-Institutional Study Assessing Simultaneous In-field Boost Helical Tomotherapy for 1-3 Brain Metastases

Department and Institution: Oncology, London Regional Cancer Program

Sponsor: ONTARIO INSTITUTE FOR CANCER RESEARCH

Ethics Approval Date: March 4, 2010

Expiry Date: December 31, 2020

Documents Reviewed and Approved: UWO Protocol (including instruments noted in Section 8.1) and Letter of Information and Consent Form dated 20Jan2010

Documents Received for Information: Clinical Trial Protocol, October 29 2009

This is to notify you that The University of Western Ontario Research Ethics Board for Health Sciences Research Involving Human Subjects (HSREB) which is organized and operates according to the Tri-Council Policy Statement: Ethical Conduct of Research Involving Humans and the Health Canada/ICH Good Clinical Practice Practices: Consolidated Guidelines; and the applicable laws and regulations of Ontario has reviewed and granted approval to the above referenced study on the approval date noted above. The membership of this REB also complies with the membership requirements for REB's as defined in Division 5 of the Food and Drug Regulations.

The ethics approval for this study shall remain valid until the expiry date noted above assuming timely and acceptable responses to the HSREB's periodic requests for surveillance and monitoring information. If you require an updated approval notice prior to that time you must request it using the UWO Updated Approval Request Form.

During the course of the research, no deviations from, or changes to, the protocol or consent form may be initiated without prior written approval from the HSREB except when necessary to eliminate immediate hazards to the subject or when the change(s) involve only logistical or administrative aspects of the study (e.g. change of monitor, telephone number). Expedited review of minor change(s) in ongoing studies will be considered. Subjects must receive a copy of the signed information/consent documentation.

Investigators must promptly also report to the HSREB:

- changes increasing the risk to the participant(s) and/or affecting significantly the conduct of the study;
- all adverse and unexpected experiences or events that are both serious and unexpected;
- new information that may adversely affect the safety of the subjects or the conduct of the study.

If these changes/adverse events require a change to the information/consent documentation, and/or recruitment advertisement, the newly revised information/consent documentation, and/or advertisement, must be submitted to this office for approval.

Members of the HSREB who are named as investigators in research studies, or declare a conflict of interest, do not participate in discussion related to, nor vote on, such studies when they are presented to the HSREB.

Chair of HSREB: Dr. Joseph Gilbert
FDA Ref. #: IRB 00000940

Ethics Officer to Contact for Further Information

<input type="checkbox"/> Janice Sutherland (jsutherland@uwo.ca)	<input checked="" type="checkbox"/> Elizabeth Wambolt (ewambolt@uwo.ca)	<input type="checkbox"/> Grace Kelly (grace.kelly@uwo.ca)	<input type="checkbox"/> Denise Grafton (dgrafton@uwo.ca)
--	---	--	---

This is an official document. Please retain the original in your files.

cc: ORE File
LHR

UWO HSREB Ethics Approval - Initial
V.2008-07-01 (rpApprovalNoticeHSREB_Initial)

16776

Page 1 of 1

Curriculum Vitae

Harish Sharma

EDUCATION:

PhD in Medical Biophysics (Current)

University of Western Ontario, London, ON, Canada

Thesis: Multiparametric imaging and MRI image texture analysis in brain tumors

Funding: Ontario Graduate Scholarship, Western Graduate Research Scholarship

PUBLICATIONS:

Sharma H, Lee TY, Bureau Y, Fisher B, Bartha R. Analysis of morphological MRI parameters and diffusion tensor parameters for perfusion CT derived high permeability areas in glioblastoma: identifying tumor recurrence from radiation induced necrosis (*Submitted to The Neuroradiology Journal*)

Sharma H, Rodrigues G, Bauman G, Bartha R, Ward A. MRI-based prediction of response to whole-brain helical tomotherapy with simultaneous intralesional boost for metastatic brain cancer using quantitative size and appearance features (*in preparation*)

Sharma H, Ward A, Bureau Y, Rodrigues G, Bauman G, Fisher B. Differentiating between Glioblastoma and Metastasis using first- and second-order MRI Image Texture (*Submitted to American Journal of Neuroradiology*)

Sharma H, Rodrigues G, Bauman G, Ward A. "Metastatic brain cancer: prediction of response to whole-brain helical tomotherapy with simultaneous intralesional boost for metastatic disease using quantitative MR imaging features", SPIE Medical Imaging (*Accepted*)